FACULTY OF ENGINEERING AND ARCHITECTURE

Advanced Imaging and Biomechanical Modeling for Cardiovascular Phenotyping in Adult Zebrafish

Matthias Van Impe

Doctoral dissertation submitted to obtain the academic degree of
Doctor of Biomedical Engineering

Supervisors

Prof. Patrick Segers, PhD* - Prof. Julie De Backer, PhD** - Prof. Patrick Sips, PhD***

* Department of Electronics and Information Systems
Faculty of Engineering and Architecture, Ghent University

** Department of Internal Medicine and Pediatrics
Faculty of Medicine and Health Sciences, Ghent University

*** Department of Biomolecular Medicine
Faculty of Medicine and Health Sciences, Ghent University

November 2025

GHENT UNIVERSITY

ISBN 978-94-93464-55-1
NUR 954
Wettelijk depot: D/2025/10.500/115

Members of the Examination Board

Chair

Prof. Hennie De Schepper, PhD, Ghent University

Other members entitled to vote

Anabela Bensimon-Brito, PhD, Centre for Integrative Biology, France
Prof. Bert Callewaert, PhD, Ghent University
Prof. Charlotte Debbaut, PhD, Ghent University
Soroush Safaei, PhD, Ghent University
Prof. Choon Hwai Yap, PhD, Imperial College London, United Kingdom

Supervisors

Prof. Patrick Segers, PhD, Ghent University
Prof. Julie De Backer, PhD, Ghent University
Prof. Patrick Sips, PhD, Ghent University

Preface

Looking back on this PhD journey, I want to start by expressing my gratitude to all of my supervisors: Patrick, Julie and Patrick. First of all thank you for the opportunity to pursue this PhD. Patrick, after my time at BioMMedA as a master thesis student, I was (and am) really grateful that I could continue at BioMMedA as a PhD student. You gave me the confidence needed to start the PhD, encouraged and guided along the way (also during this special period called COVID) and again gave me the confidence to - finally ;-) - wrap up the PhD. Julie and Patrick, thank you for also providing essential guidance and feedback throughout the journey and to introduce me to both heritable thoracic aortic disease and zebrafish research. I am grateful that next to being true examples of scientific rigor, all three of you were, from the start, very approachable and available when needed.

Thank you to the members of the examination board for taking the time to assess, improve and discuss my research. Also thank you to all (co-)authors of the publications that are the backbone of this PhD, your contributions were of course essential.

I am grateful for all moments where I could share (scientific) thoughts with colleagues from BioMMedA, the HTAD Lab, the GOA consortium, MEDISIP, UGCT and many more. Also the interactions at, a.o., (inter)national conferences, the field trips to Switzerland (PSI) or the stay at NUS (Singapore) have each in their own way shaped this research. And definitely also thank you, Jurgen en Saskia, for your (practical) help along the way.

Next to the scientific growth one experiences during a PhD, I believe that many colleagues also contributed a lot to my personal growth and to the small and big fun moments that are indispensable during a PhD. At this point (or maybe already on the previous page), one might expect I start the namedropping you certainly deserve. But, being *slightly* exhausted at the end of this journey, I will take a much shorter (*for once*) but no less sincere route.

I hope that even without listing all of your names, you all now how grateful I am for the many fun but also interesting moments. Both to the colleagues that were only present during the beginning of my PhD, the ones that traveled with me along the majority of my journey and to the ones that only arrived at the end, I had a great time, really. Both to my office roomies and the ones seated slightly further away, going to the UZ campus guaranteed pleasant interactions.

Just to give some examples: a small and non exhaustive list of fun moments can be mentioned. The starter's parties with or without hallway racing, birthday pictures @Graslei, the oven in the office accross the hallway, the World Company Sport Games @Catania and accompanying hyping of Isola Bella: grazie mille!, plant cuttings, CAMPUS football @GUSB, sweets (sometimes extremely sweet) in the kitchen, top 3's and many more. I am very grateful for this ride and also for the fact that this PhD created (or extended!) friendships.

Bedankt ook aan mijn nieuwe collega's in de Plateaustraat om mij evenzeer thuis te laten voelen op mijn nieuwe werkplek. Ik kijk zeker en vast uit naar de komende jaren.

Daarnaast en zeer gemeende merci aan mijn vrienden voor jullie interesse in dit onderzoek. Nog meer dan voor deze nieuwsgierigheid (of achterdocht naar wat er nu eigenlijk met dat belastinggeld gebeurt) wil ik jullie vooral bedanken voor de ontspannende momenten in de voorbije jaren.

Bedankt aan mijn voetbalvrienden, voor de soms tot meestal succesvolle voetbalavonden op het plein maar evenzeer de momenten naast het plein. Bedankt aan mijn studievrienden, voor dat Ardennenweekend, die citytrip, die vrijgezellen, maar evengoed elke andere gelegenheid of gewoon een avond op café. Jullie allen hebben er mee voor gezorgd ik het zwoegen op dit doctoraat even opzij kon leggen, en zorgden er zo mee voor dat de voorbije jaren op een fijne manier voorbij gevlogen zijn.

Ook heel oprecht bedankt aan mijn (schoon)familie voor de steun en aanmoedigingen! Net zoals mijn vrienden zorgden jullie voor positieve energie om de uitdagingen die gepaard gaan met een doctoraat uiteindelijk tot een goed einde te brengen. Mama en papa, bedankt aan jullie in het bijzonder om (letterlijk en figuurlijk) van bij 'mijn' start, veel vroeger dan de start van dit doctoraat dus, voor mij te zorgen. Jullie hebben mij mee gevormd tot een persoon die vandaag tevreden en trots terug- en vooruitblikt, en dat vind ik heel wat. Jullie hebben mij steeds aangemoedigd en in mij geloofd. Danku!

Broeder, jij mag jezelf uiteraard ook onder de voetbalvrienden rekenen. Omdat ik je zo hoog heb zitten op (en zeker ook naast) het voetbalveld durf(de) ik de lat af en toe hoog te leggen voor jou tijdens het minivoetballen. Ik kan dat een beetje compenseren door hier zeer terecht te vermelden dat we op het moment van schrijven grotendeels dankzij jou met MVC The Green Lions aan kop staan van reeks 2B van de befaamde Kern Gent-De Pinte. Maar meer dan dat wil ik je hier vooral bedanken om de kleine broer te zijn die iedere grotere broer zich zou wensen!

Eline, rond het begin van dit doctoraat startte ook ons pad samen. Veel meer dan je denk ik zelf beseft, kwam dit schrijfsel er heel zeker ook dankzij jou. Door nooit te oordelen toen ik (te) laat doorwerkte. En ook toen dit doctoraat in extra tijd ging en ik ondertussen al een andere job startte ben je mij zonder druk altijd blijven aanmoedigen en steunen. Ik kan niet genoeg benadrukken hoe cruciaal dat was, zowel voor de afronding zelf als voor het positieve gevoel dat ik er uiteindelijk aan over hou. Ik bewonder je daar echt voor. Jij

zag naast het feit dat ik dit doctoraat vooral graag deed meer dan wie ook de momenten van stress en zeker richting het einde ook de moeilijke momenten die met het afronden van het doctoraat gepaard gingen. Bedankt om daar op jouw goede manier mee om te gaan, echt waar, als ik daar achteraf op terugkijk beschouw ik dit zeker niet als vanzelfsprekend. Op dit moment ben ik vooral dankbaar en trots. Dankbaar voor en trots op het doctoraat. Maar nog meer dankbaar voor en trots op wat wij samen al bereikt hebben. En waar een einddatum en afronding van dit doctoraat broodnodig was, prijs ik mij gelukkig dat er voor ons geen einddatum is. Heel veel liefde!

Matthias

Table of contents

Summary

Context

The zebrafish is an increasingly popular model organism in cardiovascular research. Compared to mammalian animal models, the zebrafish model offers the advantage of the ease of genetic manipulation, the high replication rate, the lower cost and the transparency of zebrafish embryos allowing effective imaging at young age. In order to fully exploit the potential of the zebrafish model organism and understand the mechanobiology of disease development in this organism, advanced image-based phenotyping options as well as (image-based) biomechanical phenotyping is (also) required for adult zebrafish, complementing the battery of phenotyping options available during embryonic stages. The phenotyping options presented in this dissertation can, for example, be applied in (zebrafish) research related to drug induced cardiovascular toxicities, atherosclerosis, cardiomyopathies, cardiac valves and heart regeneration but heritable thoracic aortic diseases are the primary target disease. In zebrafish models of heritable thoracic aortic disease, the bulbus arteriosus and the ventral aorta are key structures of interest, showing similarities to the human aortic root, ascending aorta and aortic arch.

The main objective of this dissertation is to explore whether information on the zebrafish aortic biomechanics can be obtained via computer models of the zebrafish ventral aorta and bulbus arteriosus. A second, broader, objective is expanding the adult zebrafish cardiovascular phenotyping options in general.

Part I - Background

Zebrafish as a model organism in cardiovascular research

The physiology of the adult zebrafish cardiovascular system is addressed and compared to the human cardiovascular system. Next,

the scientific literature on zebrafish models of cardiovascular development, function and disease is summarized and heritable thoracic aortic disease is discussed both from a human and zebrafish perspective.

Model-derived aortic biomechanics

Three different type of problems are considered: computational fluid dynamics problems, computational solid mechanics problems and fluid-structure interaction problems. Numerical simulation of aortic biomechanics and derived biomechanical variables and mechanobiological stimuli, including wall shear stress, are introduced and discussed from a practical perspective.

Cardiovascular imaging in adult zebrafish

State-of-the-art zebrafish cardiovascular imaging research on histological imaging, micro computed tomography imaging, high-frequency echocardiography and magnetic resonance imaging is summarized. All four of these techniques have been applied for adult zebrafish imaging but in general, adult zebrafish cardiovascular imaging most often relies on high-frequency echocardiography and histological analysis.

Part II - Cardiovascular imaging and biomechanical modeling in adult zebrafish

Automated pulsed wave Doppler annotation and analysis in adult zebrafish

A fully automated framework to process pulsed wave doppler (PWD) adult zebrafish echocardiography measurements of ventricular in- and outflow, allowing the evaluation of all cardiac cycles in a large number of recordings without operator-dependent inputs, is presented. We applied this algorithm to a large number of ultrasound measurements in both male and female wild-type adult zebrafish of varying ages to validate the framework and we both confirm existing findings and discuss previously unreported correlations, in particular related to the early wave of ventricular inflow and the regurgitation of both ventricular in- and outflow. This framework can be used for advanced, fast and unbiased phenotyping of zebrafish models of cardiovascular disease and the reference measurement set provided in this study can serve as a benchmark for future projects.

Cardiovascular CT-imaging and 3D reconstruction in adult zebrafish

Synchrotron phase contrast computed tomography imaging was selected as the most promising technique to obtain accurate anatomical and structural three-dimensional cardiovascular information of the adult zebrafish, both for direct morphological phenotyping and as starting point for numerical simulations. We found synchrotron phase contrast micro computed tomography imaging at 21.8 keV beam energy, 250 mm object-detector distance and isotropic voxel size of 1.625 μm^3 to provide accurate two-dimensional (2D) information and three-dimensional (3D) reconstructions of key cardiovascular structures such as the atrium, ventricle, bulbus arteriosus, ventral aorta and dorsal aorta. Decalcification of the sample prior to imaging and the use of Paganin phase retrieval during the image reconstruction further improve image quality and facilitate segmentation of the resulting image stacks. Based on these modalities, major cardiovascular structures such as the ventricle and bulbus arteriosus can be segmented largely automatically and also structures such as the ventral aorta and afferent branchial arteries can be 3D reconstructed after combining several manual and automated operations. Automated segmentation of (small) luminal structures is possible if corrosion casting or contrast-enhanced casting is performed prior to the computed tomography scanning.

Fluid dynamics and biomechanics of the ventral aorta in adult zebrafish

Phenotyping of cardiovascular structure and function extends beyond (anatomical and functional) imaging, and should also address biomechanical factors as indicators of aortic disease and as intrinsic components of the mechanobiological environment within which pathophysiological processes take place. Wall shear stress, i.e., the shear stress exerted by the blood flow on the endothelial cells that line the vessel wall, as well as the stress inside the vessel wall are key metrics.

We show that modeling of the cardiovascular fluid dynamics and biomechanics in adult zebrafish is feasible. Synchrotron imaging provides accurate three-dimensional reconstructions of the main cardiovascular structures, which is complemented by high-frequency ultrasound measurements to provide additional information on in vivo blood flow characteristics. This study provides the first reference values for multiple key biomechanical stimuli in wild-type adult zebrafish, including wall shear stress and first principal stress.

This way, biomechanical phenotyping in zebrafish is no longer limited to the developing stages, as earlier reported, and also progressive or late onset conditions and phenotypes can be investigated.

Biomechanics and fluid dynamics of the bulbus arteriosus in adult zebrafish: an FSI proof-of-concept

Next to investigations of the aorta, the (patho)physiology of the bulbus arteriosus in zebrafish is interesting from a translational viewpoint, particularly for heritable thoracic aortic disease research. The position of the bulbus, directly downstream of the ventricle, is similar to the location of the aortic root in mammals, the latter providing the largest contribution to the buffering capacity of the arterial tree. In this chapter, two proof-of-concept (preliminary) fluid-structure interaction studies are reported. Both idealized 2D axi-symmetric geometries and synchrotron imaging-based 3D geometries as well as different constitutive relations to mimic the structural behavior of the bulbar wall are considered. Rather than providing accurate simulation results at this preliminary stage, the two presented proof-of-constant studies demonstrate the feasibility of biomechanical modeling of the bulbus arteriosus but also identify (important) current limitations.

Part III - Overall discussion

Overall discussion

The contribution to the state-of-the-art of this dissertation is summarized and discussed from a general perspective. Applications, clinical relevance limitations and future perspectives of the presented work are addressed explicitly and a short take home message is provided.

Samenvatting

Context

Zebravissen worden steeds populairder als modelorganisme in cardiovasculair onderzoek. In vergelijking met zoogdieren is de genetische manipulatie van zebravissen gemakkelijker, plant de zebravis zich sneller en in groter getale voort en zijn de algehele kosten beperkter. Een bijzonder groot voordeel is bovendien dat zebravissen tijdens de ontwikkeling optisch transparant zijn, wat het gebruik van krachtige beeldvormingstechnieken toelaat tijdens de eerste dagen van de ontwikkeling. Geavanceerde cardiovasculaire fenotyperingsopties gebaseerd op adequate beeldvormingstechnieken en biomechanische modellering zijn noodzakelijk om het potentieel van de zebravis als modelorganisme optimaal te benutten. Volwassen zebravissen zijn echter niet langer (optisch) transparant en de huidige opties voor cardiovasculaire fenotypering van volwassen zebravissen zijn beperkt. De fenotyperingsopties die in dit proefschrift aan bod komen kunnen, bijvoorbeeld, toegepast worden in (zebravis)onderzoek gerelateerd aan atherosclerose, cardiomyopathie, hartkleppen en cardiovasculaire regeneratie maar zijn in het bijzonder relevant in het onderzoek naar erfelijke thoracale aorta aandoeningen. De beeldvorming en fenotypering van de bulbus arteriosus en ventrale aorta van de zebravis zullen de meeste aandacht krijgen doorheen dit proefschrift, aangezien deze structuren gelijkenissen vertonen met de aortawortel en aortaboog in de mens en belangrijke cardiovasculaire manifestaties bij erfelijke thoracale aorta aandoeningen net optreden ter hoogte van de (humane) aortawortel en aortaboog.

Het voornaamste doel van dit proefschrift is onderzoeken of en welke biomechanische informatie van de ventrale aorta en bulbus arteriosus in de zebravis kan worden bekomen via computersimulaties. Het uitbreiden van de opties voor de cardiovasculaire fenotypering van volwassen zebravissen in het algemeen is een bijkomend, breder doel.

Deel I - Achtergrond

Het zebravis modelorganisme in cardiovasculair onderzoek

De fysiologie van het cardiovasculair system in volwassen zebravissen wordt besproken en vergeleken met het cardiovasculair system van de mens. Vervolgens wordt de wetenschappelijke literatuur over zebravismodellen van de cardiovasculaire ontwikkeling, cardiovasculaire functie en cardiovasculaire aandoeningen samengevat. Erfelijke thoracale aorta aandoeningen worden afzonderlijk besproken, waarbij de vergelijking met de mens nadrukkelijker wordt gemaakt.

Model-gebaseerde biomechanica van de aorta

Drie verschillende soorten computationale problemen komen aan bod in dit hoofdstuk: vloeistofdynamica problemen, vaste stof mechanica problemen en vloeistof-structuur interactie problemen. Numerieke simulaties van de biomechanica in de aorta en afgeleide biomechanische variabelen en mechano-biologische stimuli, waaronder wandschuifspanning, worden geintroduceerd en besproken vanuit een praktisch oogpunt.

Cardiovasculaire beeldvorming in volwassen zebravissen

Het meest recente onderzoek over cardiovasculaire beeldvorming in volwassen zebravissen op basis van histologie, *micro computed tomography*, (hoogfrequentie) echocardiografie en *magnetic resonance imaging*, wordt samengevat. Elk van deze vier beeldvormingstechnieken wordt toegepast in zebravissen maar echocardiografie en histologie worden algemeen beschouwd veruit het meest toegepast voor cardiovasculaire beeldvorming in volwassen zebravissen.

Deel II - Cardiovasculaire beeldvorming en biomechanische modellering in volwassen zebravissen

Automatische pulsed wave Doppler ultrageluid karakterisatie en analyse in volwassen zebravissen

Een algoritme om *pulsed wave Doppler* ultrageluid metingen van de ventriculaire bloed in- en uitstroom in volwassen zebravissen volledig automatisch te verwerken werd ontwikkeld. De verwerking en analyse van een groot aantal metingen, telkens gebaseerd op een groot aantal cardiale cycli, is mogelijk zonder operator-afhankelijke invoer. Het ontwikkelde algoritme werd ter validatie toegepast op een groot aantal *pulsed wave Doppler* ultrageluid metingen van zowel mannelijke als vrouwelijke wild-type zebravissen van

verschillende leeftijden die ook manueel geanalyseerd werden. Eerder gerapporteerde verbanden tussen parameters die de ventriculaire in- en uitstroom karakteriseren werden bevestigd maar ook nieuwe verbanden werden gevonden en besproken, in het bijzonder gerelateerd aan de regurgitatie van de ventriculaire in- en uitstroom. Het algoritme kan gebruikt worden voor geavanceerde, snelle en operator-onafhankelijke fenotypering van zebravis modellen van verschillende cardiovasculaire aandoeningen. Een uitgebreid aantal *pulsed wave Doppler* ultrageluid metingen wordt, samen met de automatische verwerking ervan, ter beschikking gesteld en kan dienen als referentie dataset voor toekomstige studies.

Cardiovasculaire CT beeldvorming en 3D reconstructie in volwassen zebravissen

Synchrotron fase-contrast *computed tomography* beeldvorming werd geselecteerd als de meeste geschikte beeldvormingstechniek voor het onderzoeken van nauwkeurige anatomische en structurele driedimensionale cardiovasculaire aspecten in volwassen zebravissen. We gebruiken synchrotron beeldvorming in dit proefschrift zowel voor rechtstreekse morfologische fenotypering als voor numerieke simulaties op basis van nauwkeurige, zebravis-specifieke, driedimensionale anatomische data. Synchrotron fase-contrast micro *computed tomography* beeldvorming gebruik makende van stralingsenergie van 21.8 keV, een afstand van 250 mm tussen het object en de detector en een isotropische voxelgrootte van 1.625 μm^3 resulteert in nauwkeurige tweedimensionale informatie en driedimensionale reconstructions van belangrijke cardiovasculaire structuren zoals het atrium, het vetrikel, de bulbus arteriosus, de ventrale aorta en de dorsale aorta. Decalcificatie van het monster voorafgaand aan de synchrotron beeldvorming en het gebruik van (Paganin) faseherstel tijdens de beeldreconstructie resulteren in de beste beeldkwaliteit en verbeteren de (automatische) segmentatiemogelijkheden. Cardiovasculaire structuren zoals het ventrikel en de bulbus arteriosus kunnen grotendeels automatisch gesegmenteerd en driedimensionaal gereconstrueerd worden. Een driedimensionale reconstructie van de ventrale aorta is ook mogelijk maar vereist meer manuele operaties, in het bijzonder voor een accurate segmentatie van de vertakkingen. Snelle, geautomatiseerde segmentatie en driedimensionale reconstructie van (kleine) bloedholtes is mogelijk door scannen van vasculaire afgietsels of *in situ* vasculaire gietsels met een contrast-verhogend medium met *computed tomography* beeldvorming.

Vloeistofdynamica en biomechanica van de ventrale aorta in volwassen zebravissen

Fenotypering van de cardiovasculaire structuur en functie gaat verder dan de directe fenotypering op basis van verschillende beeldvormingstechnieken. Ook biomechanische factoren dienen onderzocht te worden om het ontstaan en het verlopen van cardiovasculaire aandoeningen goed te kunnen onderzoeken. De biomechanische stimuli zijn intrinsiek verweven met de mechanobiologische context waarbinnen de pathofysiologische processen plaatsvinden. De schuifspanning uitgeoefend door de bloedstroom op de endotheelcellen van de weefselwand wordt wandschuifspanning genoemd. Wandschuifspanning is samen met de spanning binnenin de weefselwand een zeer belangrijke biomechanische parameter.

We hebben aangetoond dat modellering van de cardiovasculaire vloeistofdynamica en biomechanica mogelijk is in volwassen zebravissen. Synchrotron beeldvorming kan gebruikte worden om nauwkeurige (zebravis-specifieke) driedimensionale reconstructies te bekomen en (hoogfrequentie) echocardiografie kan *in vivo* informatie over de karakteristieken van de bloedstroom leveren. Deze studie rapporteert de eerste referentiewaarden voor verschillende biomechanische stimuli in volwassen wild-type zebravissen waaronder wandschuifspanning en de spanning in de weefselwand. Dankzij dit onderzoek is de biomechanische fenotypering niet langer beperkt tot de vroege ontwikkelingsstadia van de zebravis maar is fenotypering van progressieve cardiovasculaire aandoeningen en aandoeningen die pas op latere leeftijd optreden nu ook mogelijk.

Biomechanica en vloeistofdynamica van de bulbus arteriosus in volwassen zebravissen: een *proof-of-concept* op basis van vloeistof-structuur interactie simulatie

Naast de studie van (ventrale) aorta is de (patho)physiologie van de bulbus arteriosus bijzonder interessant vanuit een translationeel oogpunt, in het bijzonder in onderzoek naar erfelijke thoracale aorta aandoeningen. De anatomische positie van de bulbus, meteen stroomafwaarts van het ventrikel, is gelijkaardig aan de positie van de aortawortel in zoogdieren. De aortawortel levert de belangrijkste bijdrage tot de buffercapaciteit (*Windkessel effect*) van het arterieel netwerk. In zebravissen levert de bulbus arteriosus een cruciale bijdrage tot deze bufferwerking. In dit hoofdstuk worden de voorlopige resultaten van twee *proof-of-concept* vloeistof-structuur interactie studies voorgesteld. Zowel tweedimensionale axi-symmetrische

modellen als driedimensionale modellen gebasseerd op synchrotron beeldvorming komen aan bod, net zoals verschillende constitutieve relaties om het (materiaal)gedrag van de bulbus te modelleren. Deze proof-of-concept studies leveren op dit moment nog geen bruikbare kwantitatieve data op maar demonstreren wel dat de biomechanische modellering van de bulbus arteriosus mogelijk is. De belangrijkste beperkingen van de huidige modellen worden besproken.

Deel III - Algemene discussie

Algemene discussie

De toegevoegde wetenschappelijke waarde van dit proefschrift wordt samengevat en besproken vanuit een overkoepelend oogpunt. Verschillende toepassingen, de klinische relevantie, limitaties en toekomstperspectieven van dit onderzoek worden expliciet aangekaart, en er wordt afgesloten met een korte conclusie

Abbreviations

2D two-dimensional

3D three-dimensional

4D four-dimensional

AET aortic ejection time

B-mode brightness mode

bpm beats per minute

CFD computational fluid dynamics

CSM computational solid mechanics

CT imaging computational tomography imaging

dpf days post fertilization

EtOH ethanol

FSI fluid structure interaction

HTAD heritable thoracic aortic disease

HTADs heritable thoracic aortic diseases

M-mode motion mode

MRI magnetic resonance imaging

OSI oscillatory shear index

PWD pulsed wave doppler

PWV pulse wave velocity

TAWSS time-averaged wall shear stress

US imaging ultrasound imaging

WSS wall shear stress

Chapter 1

Context

1.1 Introduction

The aim of this research is to contribute to a more comprehensive understanding and better treatment of several human cardiovascular pathologies through a deeper understanding of the cardiovascular system of the zebrafish. Before explaining the clinical rationale in more detail, two important terms, occurring in the title of the thesis, are discussed.

Phenotyping refers to determining, analyzing and describing an organism's characteristics. Such a characteristic or *phenotype* can be the result of an organism's *genotype*, i.e., its genetic constitution or material, or environmental, i.e., external, factors. Certain phenotypes are easy to observe, for example the eye-color of a person. Many cardiovascular disease associated phenotypes require advanced (imaging) techniques for studying and reporting.

Modeling refers to mimicking a real-life situation. In life sciences the phrase *model organism* or *animal model* indicates the use of an organism, e.g., the zebrafish, to study aspects of human physiology or pathophysiology. In engineering on the other hand the phrase *computational modeling*, as used in the title of this dissertation, refers to *numerical simulations* run on a computer to solve a mathematical representation of a real-life situation.

1.2 Clinical rationale

1.2.1 Target diseases: heritable thoracic aortic disease (HTAD)

The primary target diseases are a heterogeneous group of diseases referred to as heritable thoracic aortic disease (HTAD). The common denominator in HTAD are the clinical manifestations in the aortic wall, increasing the risk of aortic aneurysm, dissection and rupture.

Our understanding of several (human) disease mechanisms in HTAD has notably improved over the past decades but several aspects remain elusive. A number of causal genes are identified but our comprehension of, for example, the genotype-phenotype correlations is incomplete. Numerous (genetic) variants of uncertain significance also require further research. Several cardiovascular phenotypes in HTAD may be subtle initially but can worsen progressively, and lifelong follow up is needed. Treatment of HTAD mainly consists of preventing (often fatal) aortic dissection. Medical treatment aimed at slowing aortic growth and (preferably prophylactic) surgical intervention constitute the main treatment options. Exploratory studies involving, a.o., multiple genes, genetic pathways and drug treatments are needed. More background information on HTAD is provided in 2.5.

1.2.2 Cardiovascular biomechanics and computational modeling

Mechanobiology is the field of science investigating how mechanics trigger responses at molecular, cellular and/or tissue level, including the impact on (e.g.) development and (patho)physiology [1]. Knowledge of the cardiovascular mechanics, often referred to as cardiovascular biomechanics, is thus required to obtain a comprehensive understanding of the (patho)physiological processes inside our body [2]. In HTAD, biomechanics play an important role in the development and progression of aortic manifestations [3, 4].

Computational modeling (numerical simulation) is often used to quantify and substantiate cardiovascular biomechanics because experimental measurement of cardiovascular biomechanics, for example experimental measurement of the mechanical stresses experienced by the cardiovascular system, is often not feasible. More background information on cardiovascular numerical simulations is provided in Chapter 3.

1.2.3 Fully exploiting the zebrafish model organism

Animal models in general are useful to improve our understanding of human cardiovascular disease. Genetics diseases can be replicated in animals, external factors can be mimicked and experimental studies involving different treatment options, for example, certain drugs, are possible. The zebrafish has several important advantages compared to other animal models used in cardiovascular research, such as mice, being for example the ease of genetic manipulation, the high replication rate, the lower cost and the transparency of zebrafish embryos allowing effective imaging.

The zebrafish is ideally suited as a first-line animal model. Exploratory studies involving multiple genes, genetic pathways and drug treatments can be performed time- and cost-effectively using the zebrafish model organism, ultimately decreasing the time from bench to bedside.

A crucial challenge is to evaluate the clinical relevance of developed (genetically engineering) zebrafish disease models adequately. An extensive and advanced cardiovascular phenotyping toolbox for zebrafish is needed. The optical transparency of developing zebrafish enables powerful in vivo microscopy imaging, allowing advanced functional and structural cardiovascular phenotyping. Starting from the in vivo imaging data, a number of reports on (numerical simulations of) early stage zebrafish cardiovascular biomechanics are also available (e.g., [5–7]).

Adult zebrafish are no longer transparent and microscopy imaging generally has to be replaced by techniques such as magnetic resonance imaging (MRI), computational tomography imaging (CT imaging) or ultrasound imaging (US imaging) to obtain 3D and or in vivo imaging data. In a murine or human setting, MRI, CT imaging or US imaging can provide powerful 3D and sometimes also four-dimensional (4D) (space+time) cardiovascular data. In adult zebrafish, this kind of data is much more difficult to obtain due the small cardiovascular dimensions as well as the need for water perfusion to keep the zebrafish alive during in vivo imaging. Anatomical cardiovascular information in adult zebrafish is in most reports based on histochemistry only and functional cardiovascular information is often limited to PWD or 2D echocardiography.

Overall, options to investigate cardiovascular phenotypes in the adult zebrafish, especially 3D, subtle and/or progressive phenotypes, are

currently very limited. Reports on (numerical simulations of) cardiovascular biomechanics in adult zebrafish are completely lacking. This dissertation aims to fill these knowledge gaps which would allow to evaluate the clinical relevance of zebrafish (HTAD) models more adequately.

The bulbus arteriosus and ventral aorta of the adult zebrafish will receive most attention throughout this dissertation. The combination of the bulbus arteriosus, a fish-specific structure in between the ventricle and the ventral aorta, and the ventral aorta itself share similarities with the human aortic root, ascending aorta and aortic arch.

The phenotyping options developed and studied in this dissertation are also relevant beyond HTAD, for example in (zebrafish) research related to drug induced cardiovascular toxicities, atherosclerosis, cardiomyopathies, cardiac valves and heart regeneration. From a broader perspective, this research is also a starting point for future research involving other organs and model organisms of similar length scales.

1.3 Objectives

The key objective of this dissertation is to apply computational tools for a biomechanical characterization of the zebrafish ventral aorta and bulbus arteriosus. A second, broader, objective is expanding the adult zebrafish cardiovascular phenotyping options in general.

This dissertation does not describe the (genetic) development of zebrafish models of cardiovascular disease. Instead, this dissertation presents new techniques to (biomechanically) characterize zebrafish disease models at adult stages.

1.4 Outline

After this introductory chapter, this dissertation is structured into three parts. In Part I of this thesis, background information is provided through three chapters. Chapter 2 describes the zebrafish model organism, especially focusing on cardiovascular research. Important aspects such as the organization of the cardiovascular system and HTAD are both discussed from a human and zebrafish perspective. Next, Chapter 3 introduces biomechanical modeling and numerical simulations of arterial mechanics and fluid dynamics. Chapter

4 summarizes different cardiovascular imaging techniques in adult zebrafish. The general imaging principles are mentioned concisely and state-of-the-art zebrafish research is discussed.

The original research is presented in Part II of this thesis and comprises four chapters. In the first of these chapters, Chapter 5, a framework to automatically analyze (a large number of) cardiac cycles in adult zebrafish PWD ultrasound recordings is provided. Also an in-depth analysis of the (correlations between) different PWD parameters is performed.

In Chapter 6, (synchrotron) micro-CT imaging is used to visualize key cardiovascular structures in adult zebrafish. Several effects, ranging from the sample preparation over parameter settings of the actual scans to different reconstruction methods, are investigated. Cardiovascular structures of interest are segmented and 3D reconstructed.

In Chapter 7, these 3D reconstructed geometries are used as input for numerical simulations. Both computational fluid dynamics (CFD) and fluid structure interaction (FSI) simulations of the ventral aorta are included in this study. These simulations provide maps of for example wall shear stress and first principal stress inside the vessel wall. In Chapter 8, the bulbus arteriosus is studied, again using numerical simulations. Both idealized (2D axi-symmetric) geometries and 3D synchrotron based geometries are considered in proof-of-concept FSI simulations.

Finally, an overall discussion forms Part III. Next to the technical achievements, special attention is paid to the clinical relevance and future perspectives of the presented research.

1.5 Publications related to this dissertation

A1 Peer-reviewed publications

- *Fluid-structure interaction modeling of the aortic hemodynamics in adult zebrafish : a pilot study based on synchrotron x-ray tomography* (**Van Impe, M.**, Caboor, L., Deleeuw, V., Olbinado, M., De Backer, J., Sips, P. and Segers, P., IEEE TRANSACTIONS ON BIOMEDICAL ENGINEERING, 2023) [8].

- *Application of an automated analysis framework for pulsed-wave Doppler cardiac ultrasound measurements to generate reference data in adult zebrafish* (**Van Impe, M.**, Caboor, L., Deleeuw, V., De Rycke, K., Vanhooydonck, M., De Backer, J., Segers, P. and Sips, P., AMERICAN JOURNAL OF PHYSIOLOGY REGULATORY INTEGRATIVE AND COMPARATIVE PHYSIOLOGY, 2023) [9].

- *Corrosion Casting of the Cardiovascular Structure in Adult Zebrafish for Analysis by Scanning Electron Microscopy and X-ray Microtomography* (De Spiegelaere, W., Caboor, L., **Van Impe, M.**, Boone, M., De Backer, J., Segers, P. and Sips, P., ANATOMIA HISTOLOGIA EMBRYOLOGIA, 2020) [10].

- *From Corrosion Casting to Virtual Dissection: Contrast-enhanced Vascular Imaging Using Hafnium Oxide Nanocrystals.* (Goossens, E., Deblock, L., Caboor, L., Van den Eynden, D., Josipovic, I., Reyes Isaacura, P., Maksimova, E., **Van Impe, M.**, Bonnin, A., Segers, P., Cornillie, P., Boone, M., Van Driessche, I., De Spiegelaere, W., De Roo, J., Sips, P. and De Buysser, K., SMALL METHODS, 2024) [11].

Under review and available as preprint

- *Early mechanisms of aortic failure in a zebrafish model for thoracic aortic dissection and rupture.* (Vanhooydonck, M., Verlee, M., Silva, M. S., Pottie, P., Boel, A., **Van Impe, M.**, De Saffel, H., Caboor, L., Tapaneeyaphan, P., Bonnin, A., Segers, P., De Clercq, A., Willaert, A., Syx, S., Sips, P. and Callewaert, B., bioRxiv, 2024) [12].

- *Systematic disruption of zebrafish fibrillin genes identifies a translational zebrafish model for Marfan syndrome.* (De Rycke, K., Horvat, M., Caboor, L., Vermassen, P., De Smet, G., Santana Silva, M., Steyaert, W., **Van Impe, M.**, Segers, P., De Backer, J., Sips, P., bioRxiv, 2025) [13].

I

Background

Chapters

Chapter 2

Zebrafish as a model organism in cardiovascular research

2.1 Introduction

This chapter provides background information on the zebrafish model organism focusing on cardiovascular research in particular. Key aspects and distinctive traits of the zebrafish model compared to other animal models are listed in Section 2.2. The physiology of the adult zebrafish cardiovascular system is described and compared to the human cardiovascular system in Section 2.3. Next, the scientific literature on zebrafish models of cardiovascular development, function and disease is summarized in Section 2.4. As HTAD are the primary target diseases in this dissertation, a separate section, Section 2.5 is used to discuss HTAD in the zebrafish as well as in humans. A summary of HTAD zebrafish disease models is included.

2.2 The zebrafish model organism

Various animal models have undeniably played, and still play, an important role in our basic understanding of human physiology, pathophysiology and drug discovery [14–17]. The last decades, the zebrafish (Danio rerio) emerged as a versatile small animal model to study a wide range of (patho)physiological conditions [18–21].

Most human organs and anatomical structures are conserved in the zebrafish. Moreover, the genes and pathways to grow and regulate

these features are highly conserved between humans and zebrafish [22], making the zebrafish suited to study diseases related to these body parts. Mammary glands, prostate, uterus and placenta are the only exception that are specific to mammals and cannot be studied in zebrafish. In general, numerous successful reports of disease modeling in zebrafish are available, for example in neuroscience [23–25] and cancer research [26, 27]. Zebrafish models of cardiovascular disease are discussed separately in Section 2.4.

The zebrafish is very suited to study human genetic disorders [28–31]. Zebrafish eggs, which are laid and fertilized externally, are easily accessible for genetic manipulation and develop rapidly. Four major growth periods can be defined and are visualized in Figure 2.1: the embryonic (0-3 days post fertilization; dpf), larval (3-30 dpf), juvenile (30-90 dpf) and adult stage (90 dpf onwards).

Figure 2.1: Images (not scaled) of the zebrafish from the embryonic (left) to the adult stage (right). The adult zebrafish reaches approximately 3 cm in length and the total lifespan varies around 3 years. dpf: days post fertilization. Images adapted and combined from [32] and [33].

CRISPR/Cas9 technology, an efficient gene editing technique, is routinely used at this point and has boosted zebrafish research [34, 35]. In mammals such as mice, genetic manipulation, using for example CRISPR/Cas9 technology, is more challenging and more expensive. Gene editing in zebrafish is efficient and the effects of the manipulation are rapidly observable.

Another attractive characteristic of zebrafish is their transparency at embryonic and early larval stages, especially considering the accessibility of the externally laid and developing zebrafish eggs. Using transgenic zebrafish lines which express fluorescent reporter genes in specific cell types, targeted tissue structures can be visualized in vivo at high resolution throughout development using fluorescence microscopy [36, 37], something which is impossible to achieve in mammals at this point. Zebrafish are also very valuable in drug screening research as they represent a complete and complex biological system of different cell types and organ structures (aspects that cannot be

modeled in cultured cells), while retaining the high-throughput potential [38–40].

Zebrafish, being a vertebrate, are evolutionary more similar to humans compared to animal models such as the Caenorhabditis elegans nematode and the fruit fly (Drosophila) which also exhibit several of the attractive characteristics mentioned above.

In section 2.3 the zebrafish cardiovascular system will be discussed including the major differences compared to the human system. On the other hand, advantages of zebrafish compared to mammals also include the ability to comfortably house a much larger number of animals at relatively small spaces, with lower maintenance, lower overall cost and much higher fecundity. Also from an ethical viewpoint, the use of zebrafish is preferred over mammals and up to 5 dpf zebrafish are not considered as laboratory animals by the legislation [41, 42]. Note that the advantages mentioned in this paragraph also favor the mouse when compared to larger mammal animal models. In zebrafish, these advantages are far more pronounced, even compared to mice. For example: a mouse breeding couple can produce approximately 10 litters of typically 6 but sometimes more pups per year, while one zebrafish breeding pair is able to produce hundreds of embryos every 1-2 weeks.

A complete replacement of other animal models by zebrafish is certainly not feasible. Instead, zebrafish should be viewed as a vertebrate first-line screening option, complementing mammals and ideally suited to efficiently form and test hypotheses on, e.g., disease mechanisms and drug effects, before resorting to mammal animal models which are more time- and resource-consuming.

2.3 The cardiovascular system in zebrafish and humans

2.3.1 The human cardiovascular system

First, to allow comparisons with the zebrafish cardiovascular system, the human cardiovascular circulation is introduced. In humans as well as in other mammals and birds, the heart consists of four chambers: the left ventricle, the right ventricle, the left atrium and the right atrium. The two atria receive blood that enters the heart while the ventricles are structurally more muscular and pump the blood out of the heart. Two circuits or circulations are present in the human cardiovascular system, each with its own ventricle and atrium:

the pulmonary circulation and the systemic circulation. A visual presentation is provided in Figure 2.2.

Two large veins, the superior vena cava and the inferior vena cava, collect venous blood from different body parts and drain into the right atrium. The right ventricle then pumps the blood through the pulmonary artery to the lungs. Oxygenated blood returns to the heart via pulmonary veins into the left atrium. This circulation is called the pulmonary circulation.

From the left atrium, blood is transferred to the left ventricle and is pumped to the aorta and distributed all over our body through arteries. Eventually, blood reaches the capillaries which connect the smallest arteries and smallest veins. The capillaries deliver oxygen and nutrients to the cells constituting the different organs. Larger veins collect the venous blood throughout our body and eventually drain into the right atrium, as described earlier. This second circuit is called the systemic circulation.

The aorta is the largest artery and the part of the aorta from the aortic root to the diaphragm is called the thoracic aorta. Distal to the diaphragm, the abdominal aorta begins. The thoracic aorta is arched and consists of an ascending (from the aortic root to the aortic arch) and descending (from the aortic arch to the diaphragm) part.

On a macrostructural level, three layers are commonly identified in the wall of arteries: the intima, media and adventitia. Key microstructural constituents of the vessel wall are endothelial cells, vascular smooth muscle cells, fibroblasts and the extracellular matrix (ECM). Endothelial cells do not have any load-bearing function but act as a selective barrier and also have important sensing and signaling functions. Vascular smooth muscle cells regulate the aortic diameter actively and are steered by the autonomous nervous system. Smooth muscle cells are also involved in elastin synthesis (predominantly during late embryonic development [43]) as well as collagen synthesis (and extracellular matrix synthesis in general) [44]. Elastin and collagen are constituents of the ECM and are load-bearing elements in large elastic arteries. Elastin is organized in concentric sheets or lamellae, alternating in between layers of smooth muscle cells. Elastin fibers are load-bearing both in the axial and circumferential direction [45].

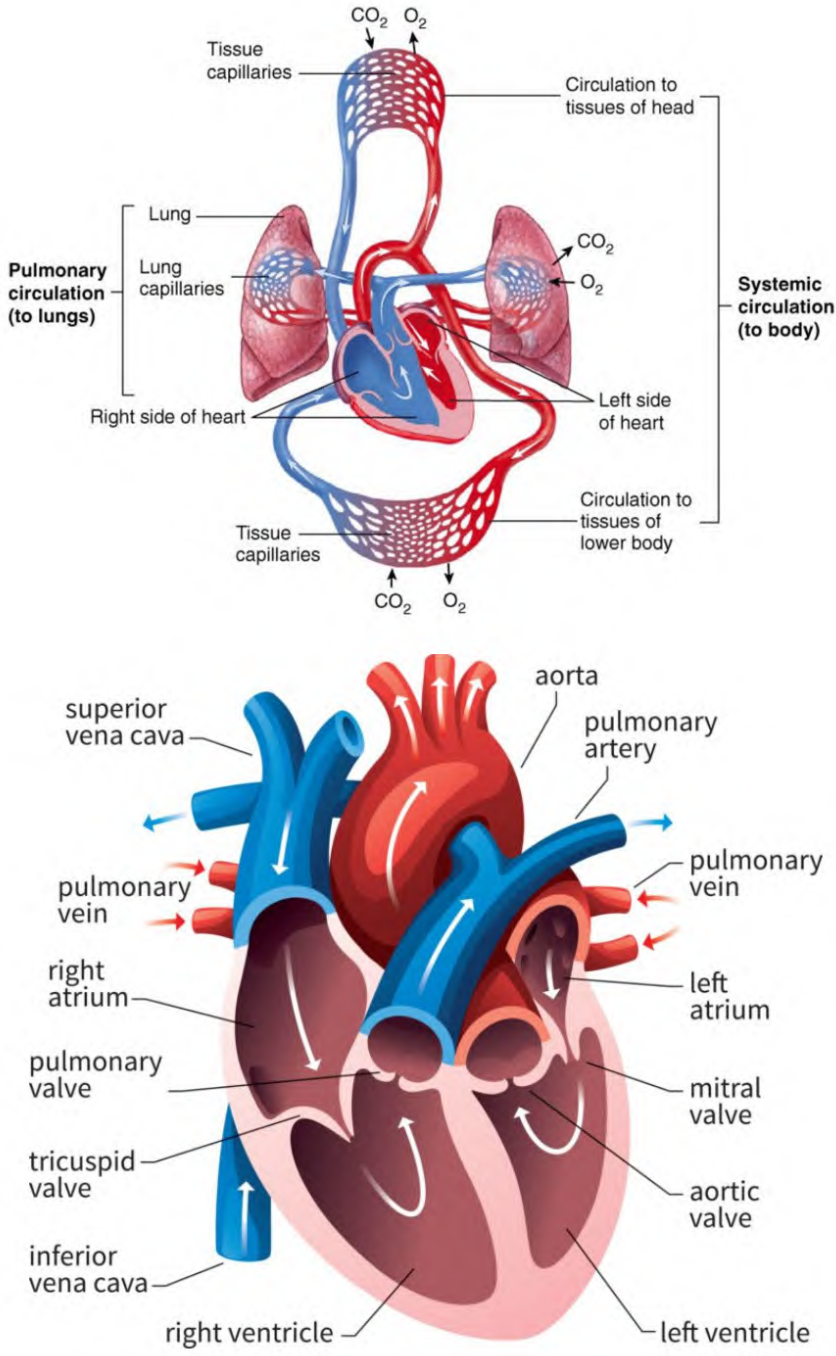

Figure 2.2: Top: schematic illustration of the human cardiovascular system (pulmonary circulation and systemic circulation). The blue color indicates deoxygenated blood, the red color indicates oxygenated blood. Bottom: a more detailed schematic of the human heart. Images adapted from [46] (top) and qcg.com.au (bottom).

Collagen ensures high-load resistance of the arterial wall. The collagen fibers do not bear any load until they are stretched completely (without any load, collagen fibers are coiled up). Collagen fibers are only load-bearing along the direction of the fibers. A visual presentation of the arterial wall structure and organization is provided in Figure 2.3.

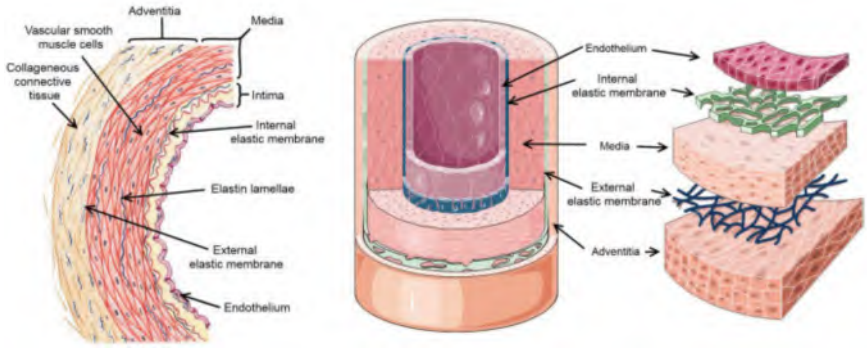

Figure 2.3: 2D (left) and 3D (middle and right) illustration of the arterial wall structure. The three major vessel wall layers being the intima, media and adventitia as well as major constituents are indicated. Adapted from [47].

Whereas the same macroscopic three-layered structure is found both in elastic arteries, muscular arteries and veins, the lumen size, wall thickness and wall composition vary greatly between these different vessels. The arterial walls are thicker than venous walls given the higher pressure load. Elastin is predominantly present in elastic arteries being the arteries closest to the heart, such as the aorta. The thick-walled elastic arteries convert the pulsatile blood flow ejected from the heart into a slower, low-pressure and continuous capillary blood flow. The crucial buffering function of elastic arteries is also called *Windkessel* function.

2.3.2 The zebrafish cardiovascular system

Zebrafish only have one cardiovascular circuit, with one ventricle and one atrium. Also other major anatomical differences are obviously present compared to the human cardiovascular system such as the presence of gills, positioned in between the zebrafish ventral aorta and dorsal aorta to oxygenate the blood. This notwithstanding, the organization and constituents of for example the ventricular and vascular wall show important similarities to the human counterparts.

Different key components of the zebrafish cardiovascular system are now described (inspired by the overview of the zebrafish cardiovascular system provided in [48] and [49]) and a simplified illustration of the adult zebrafish cardiovascular system is provided in Figure 2.4.

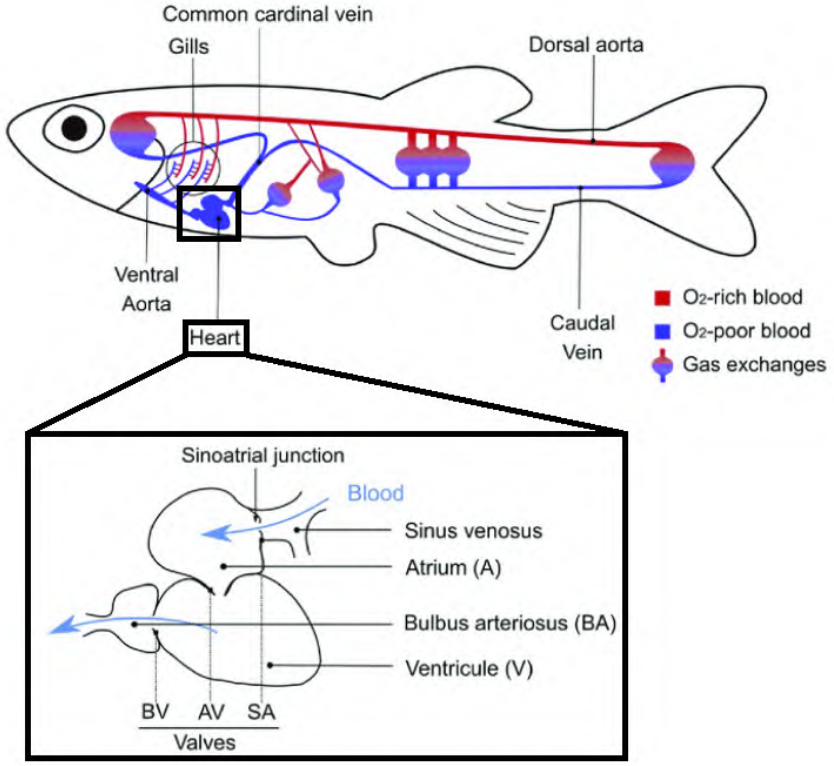

Figure 2.4: Simplified illustration of the adult zebrafish cardiovascular system. Blood is pumped by the heart and is oxygenated in the gill capillary vasculature. The gill vasculature is encircled and the heart is boxed in the top image of the zebrafish circulation. A more detailed illustration of the heart is provided at the bottom half. Blue arrows indicate the direction of blood flow. Also the position of different valves is denoted. BV: bulboventricular, AV = atrioventricular, SA = sinoatrial. Adapted from [49].

2.3.2.1 Sinus venosus

Venous blood drains via the common cardinal vein and the hepatic portal vein into the sinus venosus before it reaches the atrium. The sinus venosus of the zebrafish is extremely thin-walled and almost no myocardium is present. The sinus venosus plays an important role in the initiation and regulation of the rhythmic contractions of

the heart, as it contains pacemaker cells and conductive tissue. The sinus venosus is also present in the embryonic human heart, but becomes incorporated into the right atrium during heart development whereas this structure persists in the zebrafish. Although located inside the pericardium, the adult zebrafish sinus venosus is barely to non-contractile, and is not counted as a pumping chamber.

2.3.2.2 Atrium

Just like in the human heart, the wall of the zebrafish atrium can be divided into an endocardium, myocardium and epicardium, all with a largely similar composition as its human counterparts. Endothelial cells line the endocardium, the myocardium consists of cardiomyocytes, and the epicardium is mostly made up of epithelial cells and connective tissue. Cardiac muscle, i.e., the myocardium makes up the largest part of the atrial wall. The atrium-developed systolic pressure in zebrafish is around 0.5-1 mmHg [48]. Human right and left atrial systolic pressure reach around 8 and 12 mmHg, respectively.

2.3.2.3 Ventricle

The zebrafish ventricle also consists of an endocardium, myocardium and epicardium, again resembling the human ventricular wall organization. Compared to the zebrafish atrium, the zebrafish ventricle also mainly consists of cardiomyocytes but the ventricular wall is clearly thicker. The myocardium has two layers, an inner trabecular layer and an outer, thinner, compact layer. The density of the trabecular layer of the zebrafish ventricle is much higher compared to the zebrafish atrium. The ventricle-developed systolic pressure in zebrafish is around 2.5-3 mmHg [48]. Human right and left ventricular systolic pressure reach around 25 and 120 mmHg, respectively.

2.3.2.4 Bulbus arteriosus

The bulbus arteriosus is located just downstream of the ventricle. The bulbus arteriosus is sometimes simply named *bulbus* or, especially at embryonic or larval stages, *outflow tract*. The bulbus is a tapered, pear-shaped structure and evolves into the ventral aorta. The bulbus is located inside the pericardium but this structure mainly shows vascular characteristics. No cardiac muscle is present and the bulbar wall is organized in three layers, an intima, media and adventitia, thus following the same organization of (mammal) vascular vessels. Consequently, the bulbus is not counted as a pumping chamber and the zebrafish heart should thus be described as two-chambered, consisting of the atrium and ventricle [48].

Functionally, the bulbus can be seen as a very elastic or compliant reservoir. The bulbus provides an essential buffering or *Windkessel* role as it reduces the ventricular pressure peaks, protecting the delicate gill vasculature and other downstream nearby organs. The bulbus also ensures a more continuous blood supply to the gills allowing efficient oxygen exchange. The high ratio of elastin compared to collagen allows large distensions of the bulbus, considerably larger than the distensions seen in mammal large elastic arteries or in the zebrafish ventral aorta. In Chapter 8, computational modeling of the bulbus will be discussed and the structure and function of the bulbus are revisited at that point.

2.3.2.5 Cardiac valves

In Figure 2.4 three valves are displayed: the sinoatrial valve in between the sinus venosus and atrium, the atrioventricular valve in between the atrium and ventricle and the bulboventricular valve in between the ventricle and bulbus arteriosus. Although all three of these valves are described as cardiac valves in [49], often only the zebrafish atrioventricular and bulboventricular valves are reported as cardiac valves, e.g., [220]. In the human heart, four valves named the tricuspid, pulmonary, mitral and aortic valve, ensure one-way blood flow and pressure generation. The zebrafish bulboventricular valve could be regarded similar to the human aortic valve but the bulboventricular valve has two leaflets instead of the three-leaflet human aortic valve in the majority of individuals. Some researchers consider instead a homology between the zebrafish atrioventricular valve and human (mammalian) aortic valve.

2.3.2.6 Ventral aorta

The tapering bulbus transitions into the ventral aorta. Similar to mammals, the wall of the zebrafish ventral aorta can be divided into an intima, media an adventitia and similar key constituents are present. Up to approximately 10 layers of elastin lamellae are found near the transition of the bulbus into the ventral aorta, whereas around 5 layers of elastin lamellae are found further downstream the ventral aorta [49]. In the human ascending thoracic aorta, around 80 layers of elastin lamellae are found [50].

In contrast to the human aorta, the zebrafish ventral aorta is not arched. The zebrafish ventral aorta is straight and divides into four pairs of afferent branchial arteries supplying the blood to the gill vasculature. Functionally, the ventral aorta and the bulbus have a

similar buffering or Windkessel role as the large elastic arteries in mammals. The short distance between the delicate gill vasculature and the heart could explain the presence of the bulbus. The buffering capabilities of the ventral aorta only would be insufficient to dampen and smooth the high-pressure and highly pulsatile blood flow over such a short distance.

Common diastolic and systolic blood pressures in human aorta are 80 mmHg and 120 mmHg, respectively. In the zebrafish ventral aorta, the blood pressure varies from approximately 0.8 mmHg (diastole) to 2.2 mmHg (systole) [48].

2.3.2.7 Dorsal aorta

Downstream of the gill vasculature, oxygenated blood is collected by four pairs of efferent branchial arteries and these efferent arteries or arches merge into the dorsal aorta. The dorsal aorta is much longer than the ventral aorta and runs dorsally over the majority of zebrafish length, just beneath the vertebra. Regularly spaced branch pairs of intersegmental arteries along the dorsal aorta ensure blood supply to all regions of the fish body.

The three-layered macrostructure of the vessel wall is also observed in the dorsal aorta [51]. Whereas high elastin contents are observed in the bulbus, the elastin content is lower in the ventral aorta and further decreases along the dorsal aorta [49]. In the dorsal aorta, one to two elastic lamellae are observed in combination with one or two layers of smooth muscle cells [49, 51]. The peak pressure drops from 2.2 mmHg in the ventral aorta to 1.5 mmHg in the dorsal aorta due to the (resistive) gill vasculature [48]. Arterial valves are sporadically seen in the dorsal aorta [51].

2.4 Zebrafish models of cardiovascular development, function and disease

Multiple animal models are used in cardiovascular research [52–54]. Mouse models remain the dominant animal model in cardiovascular research but zebrafish are growingly popular and at this point used in several areas of cardiovascular research [55–66].

A dedicated section, Section 2.5, will be used to discuss HTAD both from a human and zebrafish perspective as these aortapathies are the primary target diseases in this dissertation. Next to HTAD, the

zebrafish is used to study a broad range of cardiovascular aspects and an overview is now provided.

Around 30 years ago, the first detailed descriptions of cardiovascular development in the zebrafish were reported [67–69]. Shortly afterwards, many mutations affecting the formation and function of the cardiovascular system of the zebrafish embryo were identified as part of a large-scale mutagenesis screen [70–73]. Over the past decades, most zebrafish cardiovascular research has focused on the embryonic and larval stages. The zebrafish is optically transparent during these early life stages which allows effective in vivo imaging of the developing cardiovascular structures [74]. Another interesting advantage of embryonic zebrafish is their ability to survive several days without a functional cardiovascular system, which improves the chance to recover otherwise lethal mutants compared to mammals.

A number of applications and disease models of embryonic and larval zebrafish (also referred to as developing zebrafish) are now provided. Zebrafish disease models of several congenital heart diseases are available [75,76], including tetralogy of Fallot [77], looping defects [78] and heart valve malformations [79–83]. Developing zebrafish also contribute to atherosclerosis research [84], including the role of hemodynamics in atherosclerosis [85, 86]. Hemodynamics does not only play an important role in atherosclerosis but also influences heart development and disease and the developing zebrafish is well suited for this line of research [5–7, 87–99]. Finally, developing zebrafish are an effective model for phenotypic cardiovascular drug screening [100, 101].

Both developing and adult zebrafish are a well-suited animal model to study cardiac electrophysiology, including cardiac arrhythmias. The resting heart rates of rodents (300–600 bpm) are much higher than normal adult human resting heart rates (50-100 bpm) while normal adult zebrafish resting heart rates (120-180 bpm) are still higher but more similar to the human heart rate. Also the ion channel functioning and phase timings of zebrafish resemble the human physiology better compared to rodents [102, 103]. Several arrhythmogenic cardiomyopathies have been modeled successfully in zebrafish [103–106].

A remarkable characteristic of zebrafish is their capability to regenerate a number of body parts at adult stages, including the heart and cardiac valves. Several zebrafish studies have tried to elucidate the mechanisms that allow heart and valve regeneration [24, 107–110], ultimately hoping to facilitate cardiac tissue regeneration in humans,

but a translation to the human setting has not been accomplished at this point.

Adult zebrafish are also used to study drug induced cardiomyopathies. An example is Doxorubicin, a therapeutic agent used in cancer (tumor) treatment with cardiotoxic side effects. The mechanisms that cause the cardiotoxicity, including the role of genetic predisposition, are investigated using the zebrafish [111–115].

2.5 Heritable thoracic aortic disease in zebrafish and humans

2.5.1 Human heritable thoracic aortic disease

HTAD refers to a spectrum of heritable (genetic) diseases with as common denominator the increased risk of *aortic aneurysm*, i.e, the bulging of the weakened aortic vessel wall, *aortic dissection*, i.e., tearing of the middle layer of the aorta, leading to a split of the intimal and medial aortic layers and presence of a false lumen, and eventually *rupture*, i.e., a tear through all layers of the aorta. HTAD can have an identifiable genetic cause but can also occur in families without known genetic abnormality.

Thoracic aortic aneurysms can manifest at different locations: at the aortic root, in the ascending part of the thoracic aortic, in the aortic arch or in the descending part of the thoracic aorta. These aneurysm locations are illustrated in Figure 2.5. An aortic aneurysm may also manifest in the abdominal aorta but in that case the aneurysm is likely - but not necessarily - less directly linked to a monogenetic cause but rather caused by a combination of multiple genetic and environmental factors (e.g., atherosclerotic abdominal aortic aneurysms).

Aortic dissections are categorized depending on where the dissection presumably *originates*. Following the Stanford classification, Type A aortic dissections originate in the ascending thoracic aorta while Type B aortic dissections originate in the descending thoracic aorta, distal from the left subclavian artery. Both Type A and Type B aortic dissections may extend toward the abdominal aorta.

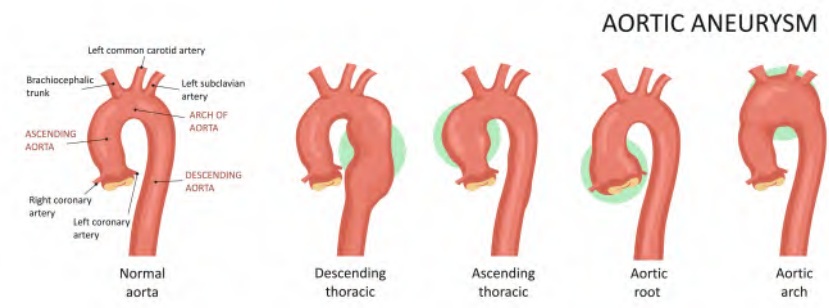

Figure 2.5: A simplified illustration of the human thoracic aorta (first image on the left) as well as illustrations of four different aneurysm locations. Image adapted from adelaidecardiothoracic.com.au.

The spectrum of HTAD ranges from monogenetic disorders caused by a defect in one specific gene to polygenetic disorders caused by a combination of several genetic and environmental factors. Monogenetic disorders are rare but the clinical manifestations are often severe. The prevalence of the polygenetic disorders is higher while the clinical manifestations can be less pronounced. Overall, the clinical manifestations in HTAD are heterogeneous and HTAD can also be subdivided into syndromic and non-syndromic diseases (with and without clinical manifestations beyond the cardiovascular system, respectively).

The genes involved in HTAD can be divided in different groups depending on the underlying mechanisms leading to the aortic manifestations [116, 117]. The genes *FBN1*, *COL3A1*, *MFAP5*, *BGN* and *LOX* encode components of the extracellalur matrix, affecting the structure of the aortic vessel wall. The genes *TGFBR1*, *TGFBR2*, *SMAD2*, *SMAD3*, *SMAD4*, *TGFβ2* and *TGFβ3* encode components of the transforming growth factor beta (TGFβ) pathway, affecting the ability to modify structure in response to changes in mechanical load imposed on the aortic wall. The genes *ACTA2*, *MYLK*, *PRKG1* and *MYH11* encode proteins involved in the contractile apparatus of vascular smooth muscle cells, also affecting the ability to modify structure in response to changes in mechanical load imposed on the aortic wall. More genes are certainly involved in HTAD since the majority of familial cases have been reported without identifiable underlying genetic defect.

Examples of syndromic HTAD linked to one or more of the aforementioned genes include Marfan syndrome (*FBN1*) [118], Loeys-

Dietz syndrome (*TGFBR1*, *TGFBR2*, *SMAD3*) [119] and vascular Ehlers-Danlos syndrome (*COL3A1*) [120]. Marfan syndrome is the longest known and most studied syndromic HTAD but also in Marfan syndrome the genotype-phenotype correlations are not yet fully understood. The prevalence of Marfan syndrome is estimated as 1 in 3.000-5.000 individuals [121]. Common cardiovascular complications in Marfan syndrome are aortic root aneurysm and dissection of the aorta, which can be fatal [122–124]. Several examples of non-syndromic HTAD are reported, for example in [125–128]. Note that in HTAD, the cardiovascular complications are often not limited to the aorta. In, e.g., Marfan syndrome, also mitral valve prolapse [129] and primary impairment of left ventricular function [130] are reported. In general, the clinical manifestations in HTAD are progressive and can require life-long follow-up.

2.5.2 Zebrafish as a model for heritable thoracic aortic disease

Several of the earlier mentioned characteristics of (developing) zebrafish are very powerful advantages in HTAD research. The fact that new genetic variants can be induced relatively easy and considerable sample sizes can be obtained time- and cost-effectively are key factors. Combined with the (in vivo) imaging options to visualize the developing cardiovascular structures, the zebrafish holds a unique position for screening and first-line HTAD research among all vertebrate animal models.

Zebrafish can be used to investigate (screen) the pathogenicity of specific genetic variants (i.e., variants of uncertain significance identified in patients). Recently, a zebrafish embryo assay successfully validated known pathogenic *SMAD3* variants while classifying another *SMAD3* variant of unknown significance as likely pathogenic [131].

Similary, *EMILIN1* and *MIB1* variants of uncertain significance identified in clinical testing have been assessed using zebrafish [132]. In [132] known pathogenic variants of *FBN1*, *COL1A2*, *COL5A1* and *COL5A2* were used as positive controls. In general, the timeframe to classify a specific variants of uncertain significance using zebrafish can be as short as two weeks [133] while purely clinically demonstrating the pathogenicity could easily take many years.

Also the role of (altered) TGFβ-signaling in aneurysm formation is investigated using zebrafish models. In [134], a zebrafish model lacking the TGFβ-receptor *alk5* is generated, and dilatation of the outflow tract (in 2.3.2 also described as the bulbus arteriosus in adult

zebrafish) is observed. In [135], a zebrafish model lacking the *ltbp1* and *ltbp3* genes (genes encoding latent-transforming growth factor beta-binding protein 1 and 3) is described and severe aneurysm formation of the outflow tract is reported.

The majority of developed zebrafish models related to HTAD do not survive until adulthood, and most reports thus *only* focus on the embryonic and larval stages. This is an important limitation. As mentioned in 2.5.1, often part of the clinical cardiovascular manifestations in HTAD are progressive and/or only present after adolescence. Zebrafish HTAD models showing similarities to the clinical manifestations seen in patients, also during adulthood, are very likely to be more accurate and comprehensive disease models than zebrafish models of which the embryos do not survive more than a few days. Developing such zebrafish HTAD models is possible, as demonstrated recently [12, 13].

In [13], a zebrafish model showing cardiovascular manifestations overlapping with Marfan syndrome is reported. Different fibrillin genes in the zebrafish are targeted and a promising zebrafish model showing dilatation of the bulbus arteriosus both during developing and adult stages is found.

In [12], a zebrafish model targeting the zebrafish smad3 and smad6 genes is described. In humans, loss of function of *SMAD3* and/or *SMAD6* results in, a.o., thoracic aortic aneurysm and dissection. A zebrafish model of thoracic aortic dissection and rupture is reported in this study.

To conclude this overview, two review articles are worth mentioning. Recently, state-of-the-art research on zebrafish models of thoracic aortic genetic variants was summarized in [133]. In [49], the use of zebrafish to study several vascular elastic fiber pathologies is discussed. Part of the included vascular elastic fiber pathologies are heritable thoracic aortic diseases (HTADs).

Chapter 3

Model-derived aortic biomechanics

3.1 Introduction

Many important cardiovascular biomechanical metrics, e.g., the stress within the wall of the aorta, or the shear stress exerted by blood flow on its wall (wall shear stress), cannot be (easily) obtained experimentally. Numerical simulations are therefore often used to compute the aortic hemodynamics and biomechanics. Numerical simulations are calculations run on a computer to solve a set of equations mimicking a real-life problem and for which there is no analytical solution. Numerical simulations thus refer to the solving process of a model of a certain physical system, using numerical techniques to do so.

Numerical simulations are very valuable to virtually investigate (i.e., *simulate*) different scenario's, to optimize certain parameter choices or to provide information about metrics that would not be available otherwise. At this point, numerical simulations are widespread in different engineering fields such as aerodynamics, fire safety engineering, mechanical construction and biomedical engineering.

Three different types of problems can be considered: (i) flow problems considering only the aortic fluid dynamics inside the vessel lumen, (ii) structural problems considering only the aortic solid mechanics of the vessel wall and (iii) problems considering both the fluid dynamics

inside the lumen and the solid mechanics of the vessel wall at the same time. This third type of problem is called a fluid-structure interaction (FSI) problem.

The governing equations as well as several common constitutive relations describing aortic fluid dynamics and solid mechanics are now provided (Section 3.2). Afterwards, the actual numerical simulations are discussed from a practical point of view (Section 3.3).

3.2 Governing equations and constitutive models

3.2.1 Aortic fluid dynamics

Two conservation principles dictate the behavior of any fluid: the conservation of mass and the conservation of momentum.

In fluid mechanics, the principle of conservation of mass is mathematically expressed via the continuity equation:

$$\frac{\partial}{\partial t}\rho_f + \nabla \cdot (\rho_f \vec{v}) = 0 \tag{3.1}$$

In this equation, ρ_f is the fluid density and $\vec{v}$ is the velocity vector field.

Within this dissertation, blood in the zebrafish arterial system is modeled as an incompressible fluid which implies that its density is constant. Equation 3.1 then reduces to:

$$\nabla \cdot \vec{v} = 0 \tag{3.2}$$

The conservation of momentum for an incompressible fluid is expressed as:

$$\rho_f \frac{\partial \vec{v}}{\partial t} + \rho_f (\vec{v} \cdot \nabla)\vec{v} = \nabla \cdot \vec{\vec{\sigma_f}} + \vec{f_f} \tag{3.3}$$

Body forces $\vec{f_f}$ are neglected in this dissertation. The stresses $\vec{\vec{\sigma_f}}$ are the sum of normal stresses caused by the internal pressure p_f (per unit area) and shear stresses $\vec{\vec{\tau_f}}$ caused by viscous forces (per unit area). Taking these aspects as well as the notation $\vec{\vec{I}}$ for the identity matrix into account, Equation 3.3 can be written as:

$$\rho_f \frac{\partial \vec{v}}{\partial t} + \rho_f (\vec{v} \cdot \nabla)\vec{v} = \nabla \cdot (-p_f \vec{\vec{I}} + \vec{\vec{\tau_f}}) \tag{3.4}$$

In this dissertation, blood is modeled as a Newtonian fluid, implying that the shear stress $\vec{\tau_f}$ can be linked to the velocity vector $\vec{v}$ via the following constitutive relation:

$$\vec{\tau_f} = \mu(\nabla\vec{v} + \nabla\vec{v}^T) \tag{3.5}$$

where μ is the dynamic viscosity, assumed constant.

3.2.2 Aortic solid mechanics

The governing equation to model aortic solid mechanics is based on the conservation of linear momentum (Newton's second law):

$$\rho_s \frac{\partial^2\vec{u}}{\partial^2 t} = \nabla\vec{\sigma_s} + \vec{f_s} \tag{3.6}$$

In left hand side of this equation, ρ_s is the solid density and $\vec{u}$ is the displacement vector field. In the right hand side of this equation, $\vec{\sigma_s}$ is the Cauchy stress tensor and the vector $\vec{f_s}$ represents body forces working in on the solid. Body forces are again neglected in this dissertation.

Different constitutive relations to link the stress tensor $\vec{\sigma_s}$ to the displacement vector field $\vec{u}$ can be considered for aortic tissue, for example a linear elastic material assumption, Neo-Hookean material assumption or the Holzapfel-Gasser-Ogden material model. More details are provided in the relevant chapters: see Chapter 7 and 8.

3.3 Numerical simulations in practice

Often, no analytical solution can be found for the (set of) partial differential equations representing the cardiovascular flow and/or structural problem. The problem is therefore discretized in space and (for time-dependent simulations also in) time allowing to apply numerical methods to find a (numerical) solution. All numerical simulations in this chapter were performed using COMSOL Multiphysics®. A detailed review of the theory of numerical simulations is beyond the scope of this dissertation. Below, several key aspects are to set up numerical simulations of arterial mechanics and fluid dynamics in practice.

3.3.1 Obtaining the geometry

The geometry in simulations of human cardiovascular biomechanics is often based on medical imaging. Geometries can for example be obtained from CT imaging datasets covering the volume of interest and a 3D geometry of the aorta can be extracted by a technique called *segmentation*. In this dissertation, the Mimics (Materialise, Leuven, Belgium) software is used to perform the segmentations.

Figure 3.1-A, displays a 3D reconstruction of a dissected aorta, obtained from a CT imaging dataset after segmentation. Depending on the aim of the study, either an idealized geometry or patient-specific (or mouse-specific or zebrafish-specific) geometry is used in the simulations. An idealized geometry is often still inspired by imaging but is a simplified, generalized geometry and can be defined by a combination of parameters (diameters, lengths, curvature radii, etc.) as illustrated in Figure 3.1-B. A patient-specific geometry on the other hand is directly obtained from the segmentation of a specific imaging dataset and and expample is provided in Figure 3.1-C.

Patient-specific geometries, or in the context of this dissertation, zebrafish-specific geometries are thus anatomically (and physiologically) more accurate than idealized geometries but require suitable 3D imaging data and often require more computation resources.

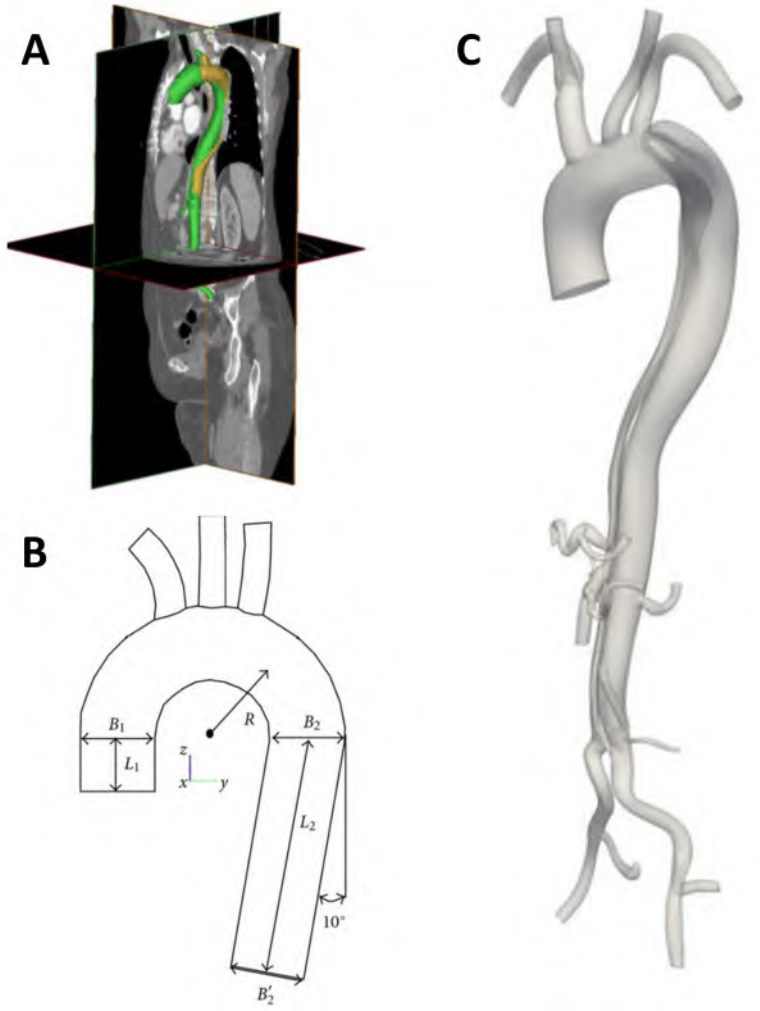

Figure 3.1: A: after segmentation, 3D reconstructions of, e.g., the aorta can be obtained from (CT-)imaging datasets. Adapted from [136]. B: idealized geometry of the aorta. Adapted from [137]. C: patient-specific geometry of the aorta. Adapted from [138].

3.3.2 Material properties

The material behavior can be simulated by employing appropriate constitutive models and accompanying material constants. To model the blood (under the incompressible and Newtonian assumptions), values for the density and dynamic viscosity need to be provided. The number of material constants to model the vessel wall depends on the used constitutive relation and the choice to model the vessel wall as a whole or the combination of, e.g., three layers reflecting

the typical three-layered aortic macrostructures. The used material property values for the different simulations in this dissertation are provided in the relevant chapters (Chapter 7 and Chapter 8).

3.3.3 Boundary conditions

Next to the geometry and the material properties, also the boundary conditions need to mimic the true situation as realistic as possible in order to obtain meaningful simulation results. Boundary conditions are applied at the boundaries of the model, i.e., the faces that form the geometric border of the model.

In cardiovascular CFD simulations, inlets (faces through which the flow enters the considered geometry), outlets (faces through which the flow exits the considered geometry) and walls (faces not allowing fluid to enter or exit the considered geometry) are distinguished. Prescribing the flow or pressure are possible boundary conditions at the in- and outlets. Also defining the ratio of pressure over flow is an example of an (outlet) boundary condition (referred to as a resistive boundary condition). A no-slip boundary condition is commonly imposed on the wall surface, indicating that the velocity of the blood is the same as the velocity of the walls.

An example of in- and outlet boundary conditions in a CFD model of the aortic arch is shown in Figure 3.2. A flow rate time profile is defined at the inlet while different resistive boundary conditions are applied at the four outlets.

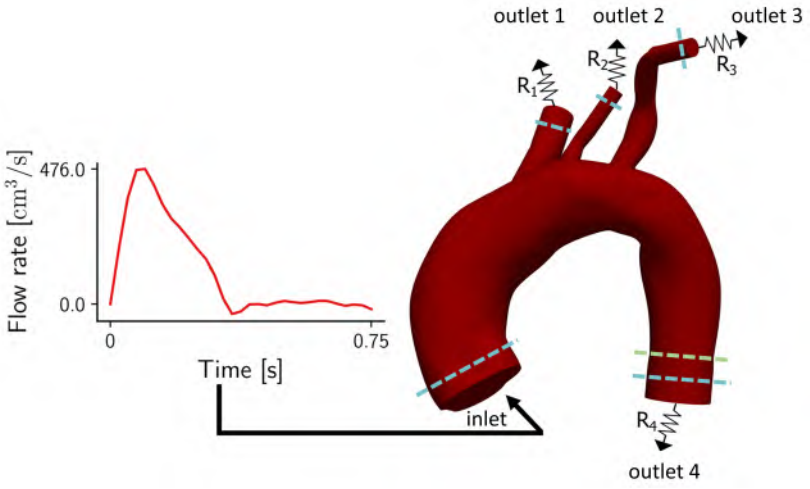

Figure 3.2: Example of in- and outlet boundary conditions in a CFD model of the aortic arch. Adapted from [139].

For computational solid mechanics (CSM) and FSI simulations, additional boundary conditions are applied to the vessel wall (outer surfaces). Possible boundary conditions can be the constraining of the surface, constraining of the surface but only in specific directions but also free movement can be allowed.

The used boundary conditions for the different simulations in this dissertation are provided in the relevant chapters (Chapter 7 and Chapter 8).

3.3.4 Meshing

A mesh can be described as a division of the volume of interest into small blocks (mesh elements). In CFD simulations, tetrahedral elements (bounded by four triangular faces) are commonly combined with prismatic boundary layer elements to mesh the lumen volume. Such meshes can be generated via the used simulation software in this dissertation. A boundary layer is often meshed with prismatic elements to allow more accurate calculations of the velocity near the wall (and thus to allow more accurate calculations of wall shear stress (WSS) - see also Section 3.4).

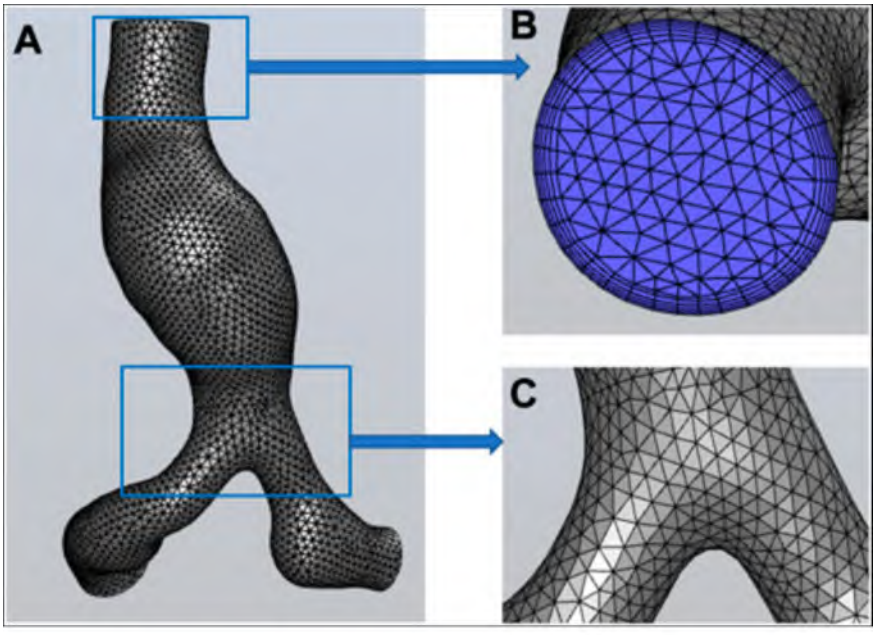

Figure 3.3: Panel A: mesh for a CFD simulation of an abdominal aortic aneurysm (AAA). The boxed areas indicate zoomed in views shown in panel B and panel C. The mesh consists of tetrahedral elements and a prismatic boundary layer (visible in panel B). Adapted from [140].

To mesh the vessel wall, again, tetrahedral elements can be used. Note that both in CFD, CSM and FSI cardiovascular simulations, structured meshes might also be used (using hexahedral elements) instead of the unstructured meshes (mainly) consisting of tetrahedral elements. Generally speaking, structured meshes reduce the numerical error but structured meshes are also more difficult to generate, often requiring specialized software and/or custom coding.

The numerical (accuracy of the) simulation solution depends on the number of mesh elements (the more elements, the better the accuracy but also the longer the computation time) and a mesh independence study should be performed to select a suitable mesh.

3.4 Wall shear stress

Numerical simulations can be used to obtain details on, e.g, the pressure, flow field or displacement in a cardiovascular problem. Very often, another (biomechanical) metric, wall shear stress (WSS) is also investigated in cardiovascular simulations. Wall shear stress (in this context) is the shear (i.e., tangential) stress exerted by the blood on the inner surface (consisting of endothelial cells). Wall shear stress equals the shear rate (i.e., the rate of change of blood velocity near the wall) multiplied by the blood viscosity. Blood pressure on the other hand results in a normal stress acting on vessel walls. An illustration is provided in Figure 3.4.

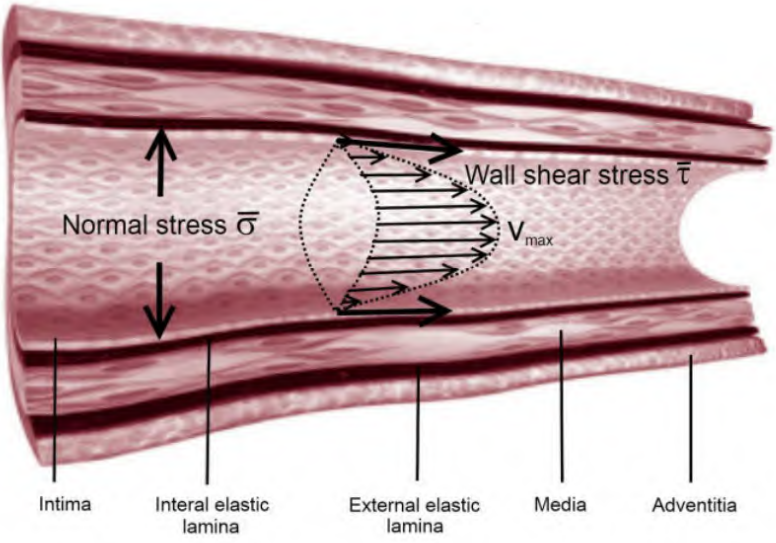

Figure 3.4: Schematic illustration of the velocity profile, wall shear stress and normal stress in a vessel wall. Adapted from [141].

Chapter 4

Cardiovascular imaging in adult zebrafish

4.1 Introduction

This chapter reviews several adult zebrafish cardiovascular imaging modalities. State-of-the-art cardiovascular disease characterization in e.g. human or murine research often involves the combination of multiple imaging techniques, commonly including histology, microCT, ultrasound and MRI. Also numerical simulations of the human or murine cardiovascular system are often based on one or more of these techniques, and therefore these four imaging modalities are discussed first in 4.2.2, 4.3, 4.4 and 4.5, both from a general and zebrafish cardiovascular research viewpoint. An explicit comparison of these techniques for zebrafish cardiovascular research is provided in 4.6. In addition to histology, microCT, ultrasound and MRI, a few other, in adult zebrafish research less frequently applied imaging modalities, are briefly discussed in 4.7.

4.2 Histological imaging

4.2.1 General principle

Microscopic imaging of histological slides is one of the most frequently used techniques to examine the (micro)structure of tissues in preclinical research. Histological slide preparation involves several steps,

important ones being *fixation*, *embedding*, *sectioning* and *staining*. A short and simplified explanation of each of these steps is provided below.

First, after sacrificing the animal, degeneration of the tissues is stopped. This step is called *fixation* and tissues are usually fixed using a formalin solution, which leads to cross-linking of proteins in the tissue. In the *embedding* step, the fixed specimens are embedded, often after trimming, dehydration, decalcification and/or clearing. Paraffin wax is the common embedding medium. The embedded tissue is *sectioned* with a specialized device: the microtome. This produces thin tissue sections which are attached to glass slides. Differential histochemical *staining* of these tissue slices is performed using specific dyes to enhance the contrast and highlight tissues of interest. This way, visibility is improved for (bright-field) microscopic imaging. A common example is hematoxylin-eosin staining.

Immunohistochemical staining of tissue sections involves the same overall steps but instead of dyes, antibodies are used to label certain proteins and dedicated sample preparation and processing steps are necessary. Fluorescent-labeled secondary antibodies can be used and fluorescence microscopy, instead of bright-field microscopy, is then used to visualize the sample.

4.2.2 Histological imaging in adult zebrafish

Also in adult zebrafish cardiovascular research, histology is often performed. Different protocols have been compared and optimized [142, 143], both for larval, juvenile and adult zebrafish. Different staining reagents to visualize the adult zebrafish cardiovascular microstructure are encountered in literature. Hu et al. were one of the first groups rigorously describing cardiovascular morphology and microstructure in adult zebrafish [48]. They presented a hematoxylin-eosin stained cross section of the bulbus arteriosus (Figure 4.1, Left) as well as Masson trichrome stained sections of the bulboventricular (valve) region (Figure 4.1, Right). In Masson trichrome staining the muscle fibres, predominantly present in the ventricle, appear red, while the collagen, predominantly present in the bulbus arteriosus, appears blue.

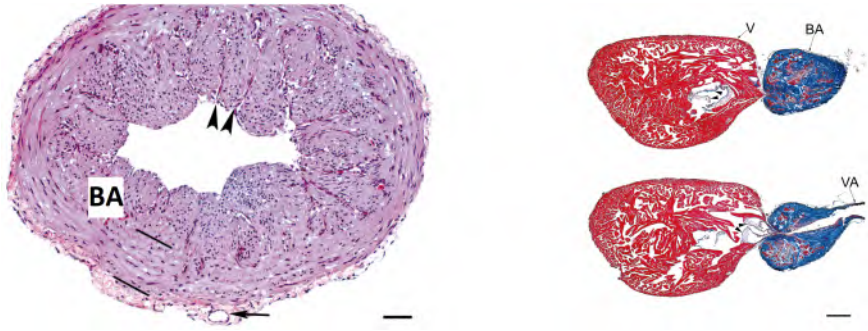

Figure 4.1: Left: Hematoxylin-eosin stained cross section of the bulbus arteriosus. The two line bars separate the three concentric layers. Arrowheads indicate ridges separating the luminal surface and subjacent tissue into a lobed formation. At the bottom, the coronary vessel is indicated by the arrow. Scale bar: 20 µm. BA: bulbus arteriosus. Right: Masson trichrome stained sections showing the atrioventricular valve leaflets (arrowheads in the top image) and bulboventricular valve leaflets (arrowheads in the bottom images). Scale bar: 100 µm. BA: bulbus arteriosus, V: ventricle, VA: ventral aorta. All image panels were adapted from [48].

Menke et al. reviewed the entire adult zebrafish anatomy [144] and hematoxylin-eosin stained sections of the heart region can be appreciated in Figure 4.2 and Figure 4.3.

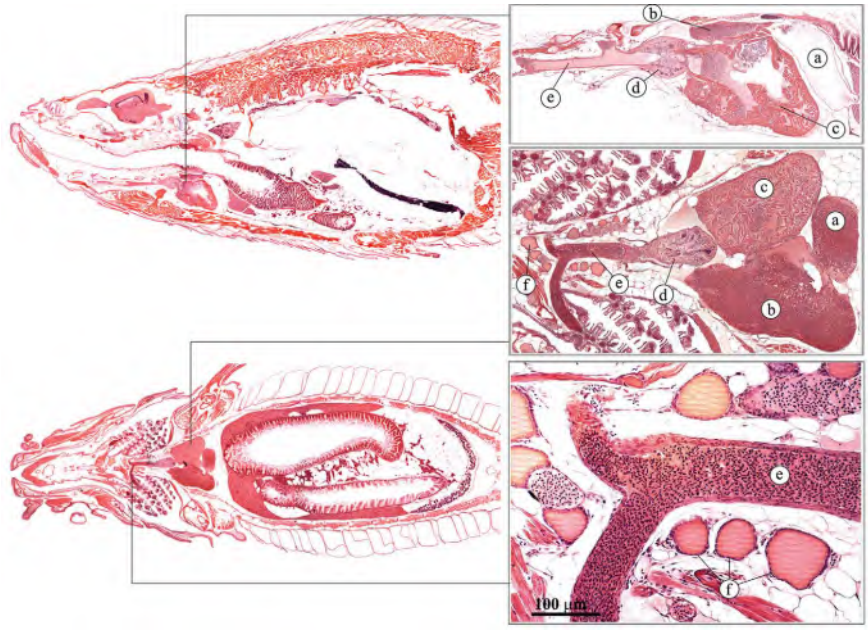

Figure 4.2: Hematoxylin-eosin stained sections of the heart region in different views. (a) Sinus venosus; (b) atrium; (c) ventricle; (d) bulbus arteriosus; (e) ventral aorta; (f) thyroid follicles. Adapted from [144].

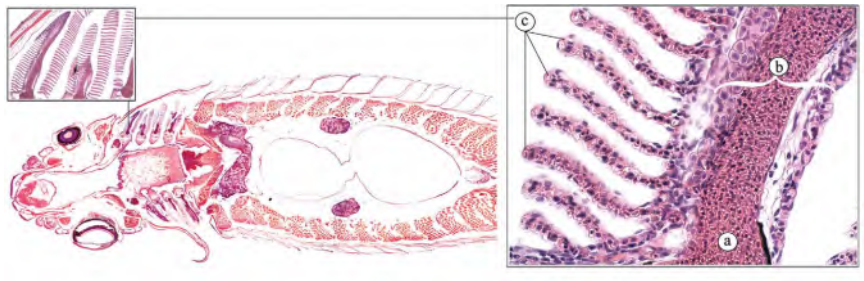

Figure 4.3: Hematoxylin-eosin stained section of the gill vasculature, depicting a lamellar artery (a); primary lamella (b) and secondary lamellae (c). Adapted from [144].

Hoareau et al. discussed different elastin related vascular pathologies in zebrafish [49,145] and used both Masson trichrome staining, orcein staining and immunolabeling with anti-elastin antibodies (immunohistochemical staining) as depicted in Figure 4.4.

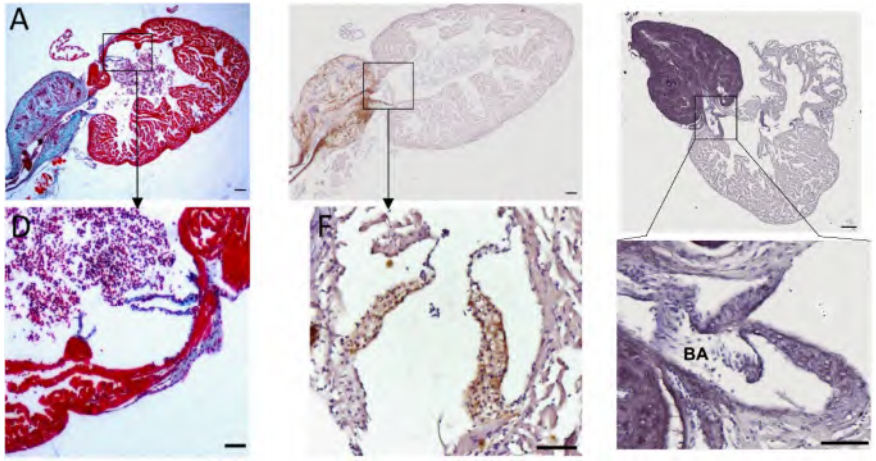

Figure 4.4: Histological sections of the bulboventricular (valve) region in adult zebrafish. Left: Masson trichrome staining. Images adapted from [49]. Mid: immunohistochemistry against elastin. Images adapted from [49]. Right: Orcein staining. Images adapted from [145]. Scale bars top row (all three panels): 100 µm and bottom row: 50 µm (all three panels).

Several other examples of (immuno)histochemical staining of the adult zebrafish cardiovascular structures can be found in literature but the discussed examples should suffice to provide the reader an impression up to which level of detail microstructural and morphological aspects of zebrafish cardiovascular structures can be assessed using histological imaging.

4.3 (Synchrotron) X-ray computed tomography

4.3.1 General X-ray and X-ray computed tomography principle

X-rays are, just like for example infrared, visible light and ultraviolet, part of the electromagnetic spectrum. Compared to these other electromagnetic waves, the wavelengths of X-rays are shorter and their energy is higher. When an X-ray beam encounters a material, this material absorbs or scatters a portion of the X-rays. This property can be exploited for imaging purposes by capturing the remaining transmitted X-rays that pass through the material. More X-rays pass through soft materials such as the arterial vessel wall compared to denser materials such as bones. Soft tissues appear dark (gray) on the resulting X-ray image while bones appear white on the X-ray image.

Plain X-ray imaging (also called projectional radiography) and X-ray computed tomography imaging (also called computed tomography imaging or CT-imaging) should be distinguished. In both cases, X-rays are used and the underlying working principles as explained above are the same. The difference is that a plain X-ray image is a 2D image resulting from a single scan while in X-ray computed tomography, multiple scans of the same object or patient are taken under different angles which are combined and computer processed resulting into a 3D dataset.

In clinical practice, plain X-ray scans are sometimes used for, e.g., a (first) evaluation of bone fractures, since they are less expensive and the radiation dose a patient receives is lower compared to a CT scan. On the other hand CT scans provide more complete and more detailed information.

4.3.2 General synchrotron X-ray computed tomography principle

In synchrotron X-ray computed tomography imaging used the same X-ray computed tomography principle as described above. But, in synchrotron imaging, X-rays beams are produced by particle acceleration in dedicated (large) facilities contrary to conventional X-rays which are produced in smaller laboratory or clinical settings by electron bombarding of a (often tungsten) target. The synchrotron radiation allows better image quality compared to conventional X-rays.

In synchrotron phase-contrast CT imaging, the coherence of synchrotron radiation (in-phase X-ray waves) is used to exploit differences in

refractive indices of materials. This produces a phase shift in the X-rays passing through the sample. By placing the imaging detector at a specific distance from the sample, interference between waves can be used to enhance contrast in the image. These methods provide higher contrast compared to normal absorption-based X-ray imaging, making it possible to distinguish (small) soft tissue structures from each other that have almost similar density. It is particularly useful for enhancing the contrast of surfaces and interfaces in samples, which would not be visible using absorption contrast.

Synchrotron imaging is not used in clinical practice but has, for example, been applied to mice in cardiovascular research [146].

4.3.3 X-ray computed tomography in adult zebrafish

For cardiovascular imaging of adult zebrafish, only (3D) CT-scans are used because of the desired level of soft tissue detail. Due to the needed high resolution ($\sim$ µm order) and accompanied field-of-views (mm $\times$ mm $\times$ mm order) the phrase *micro CT-imaging* is commonly used. Imaging at this level of detail has technical implications on for example the required detectors.

Dullin and Habich [147] described protocols both for *in vivo* and *ex vivo* micro CT-imaging, but focused on the gonads. While cardiovascular *in vivo* micro CT-imaging of mice is possible since a couple of years [148], in zebrafish, whose cardiovascular dimensions are more than a fivefold smaller compared to mice, the cardiovascular soft tissue level of detail obtainable with *in vivo* micro CT-imaging is not sufficient. All upcoming mentioned micro CT studies in zebrafish are performed *ex vivo*, allowing, compared to *in vivo* imaging, better spatial resolution and soft tissue contrast because, a.o, (i) no twitching, breathing or cardiac motion is present during the scan, (ii) scan modalities such as the duration of the scan or X-ray energy are not a limiting factor in *ex vivo* studies and (iii) dedicated sample preparation, possibly involving contrast-enhancing staining, is feasible.

Babaei et al. [149] investigated different contrast (staining) agents for micro CT imaging of adult zebrafish, but did not focus on the cardiovascular structures in particular.

Bensimon-Brito and Boezio et al. [150] used different imaging techniques to study cardiovascular disease in adult zebrafish, one of them being *ex vivo* micro CT-imaging. They could obtain 3D reconstructions of the largest cardiovascular structures: atrium, ventricle and bulbus (they use the phrase *outflow tract*), as depicted in Figure 4.5.

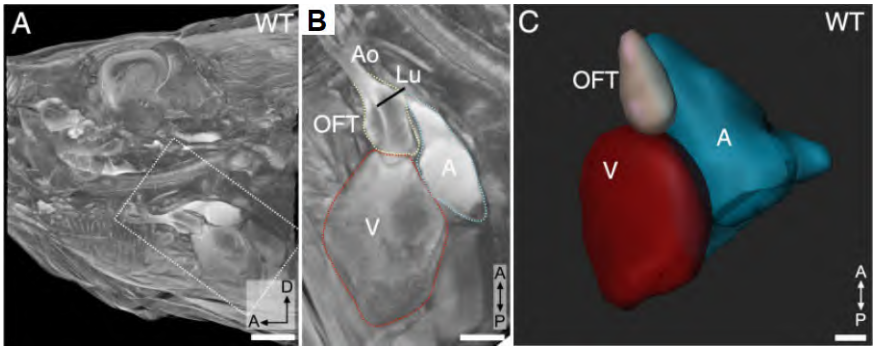

Figure 4.5: Panel A: A sagittal micro-CT cross section of the anterior part of an adult zebrafish, showing a.o. the eye and heart region. The white dashed box encloses the heart region. Panel B: a zoomed and translated view of the white dashed box heart region of panel A. Panel C: 3D reconstruction of the adult zebrafish heart based on micro CT-imaging. WT: wild-type, Ao: (ventral) aorta, Lu: lumen (of the bulbus), OFT: outflow tract or bulbus, A: atrium, V: ventricle. Scale bars: 1 mm (A), 500 µm (B), 300 µm (C). Adapted from [150]

4.3.4 Synchrotron X-ray computed tomography in adult zebrafish

Weinhardt et al. used synchrotron micro CT-imaging for automated segmentation of several organs in adult zebrafish [151]. Also Seo et al. used synchrotron phase-contrast micro CT-imaging but studied hypercholesterolemic zebrafish and do not mention the cardiovascular structures [152].

Ding et al. [153] report zebrafish phase-contrast synchrotron micro CT-imaging in a fairly comprehensive study, but just like in the studies of Babaei et al. [149] and Weinhardt et al. [151], the cardiovascular structures are part of their study but not a primary focus. They report near histological level of details, but (due to limitations of the field-of-view) only larval and juvenile (33 dpf) zebrafish samples are included.

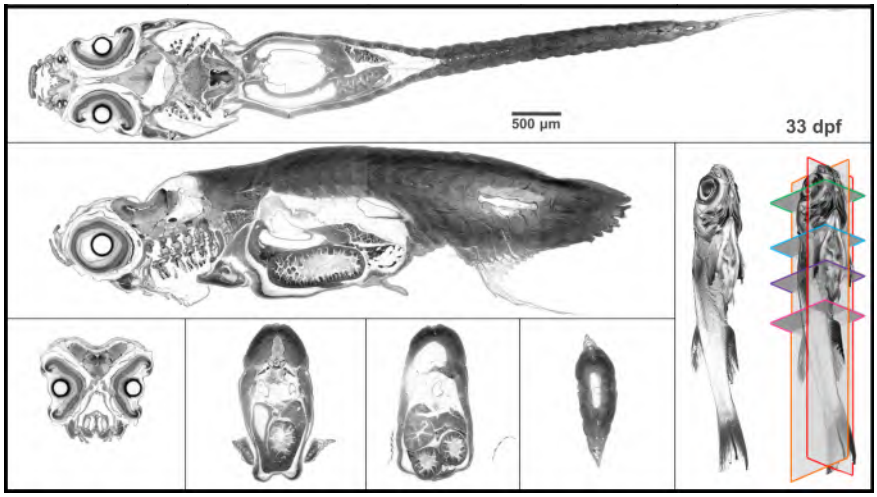

Figure 4.6: Whole body synchrotron phase contrast microCT imaging of a juvenile (33 dpf) zebrafish scanned at 1.43 µm^3 isotropic voxel size. Coronal, sagittal and axial cross sections are shown, as well as a 3D rendering at the bottom right. Adapted from [153].

4.4 Echocardiography

4.4.1 General principle

Echocardiography or cardiac ultrasound imaging is a non-invasive technique allowing in vivo imaging and measurements. An ultrasound transducer, also called probe, containing piezoelectric material is used to convert electrical energy into pressure waves of ultrasonic frequency. These waves travel through the imaged medium and at each change in acoustic impedance the wave is partially reflected and/or scattered while the remaining wave is transmitted further into the medium.

In cardiovascular ultrasound imaging, reflections caused by the tissues constituting vessel walls and heart chambers are often targeted. Reflections are predominantly oriented opposite to the incoming direction and occur when a change in impedance is encountered on an object that is much larger than the ultrasound wavelength. Red blood cells on the other hand can be targeted scatter objects. Scattered waves do not have a preferred direction and occur predominantly on objects that are smaller than the ultrasound pulse wavelength. Reflected and scattered waves that reach the transducer are reconverted into an electric signal and further processed to visualize and characterize the imaged area.

Different applications of this general principle result in different ultrasound modes such as B-mode ultrasound imaging, color Doppler ultrasound imaging and pulsed wave Doppler ultrasound imaging.

4.4.2 High-frequency echocardiography in adult zebrafish

In the first report of ultrasound imaging in adult zebrafish, ultrasonic frequencies of 7 and 8.5 MHz were used to image the heart [154] but the obtained cardiovascular functional information was limited. In general higher wave frequencies of 50-80 MHz are needed to image the small zebrafish heart at useful resolution. In a human setting, a 2-18 MHz range is commonly used. Several research groups made use of custom-developed high-frequency ultrasound setups [155–160] which allow several evaluations of cardiovascular function in the adult zebrafish. Commercial high-frequency ultrasound machines and transducers suited for preclinical small animal ultrasound imaging are also available and used [161–164].

As water is a good medium to transmit the ultrasound waves, the fish can remain under water during ultrasound imaging. Most groups reported the use of a simple sponge and made an incision in the sponge to fit and stabilize the zebrafish with their ventral side facing upwards during the measurement (Figure 4.7 top). At Ghent University, a custom set up was developed (Figure 4.7 bottom).

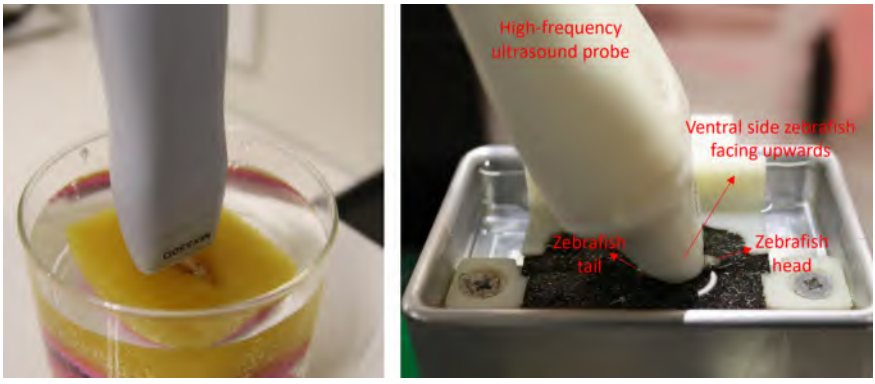

Figure 4.7: Adult zebrafish ultrasound imaging is often performed under water using a simple sponge (left image, adapted from [163]). A custom developed (3D printed) holder was developed at the Center for Medical Genetics Ghent (right image, adapted from [9]).

High-frequency ultrasound imaging is currently the only fairly widespread technique to assess functional cardiovascular parameters in

adult zebrafish but limitations compared to the human setting are present. Whereas in human or murine ultrasound imaging blood velocity time profiles at several positions along the aorta or major branches can be obtained, this is not feasible in zebrafish at this point. Anesthesia is practically unavoidable to perform the zebrafish ultrasound measurements but since anesthesia has an impact on the cardiovascular parameters it is important to minimize both the dose of the anesthesia and duration of the measurement. A standardized experimental protocol is crucial [163, 164].

The positioning of the probe with respect to the zebrafish depends on the desired imaging mode, and different probe positions are illustrated in Figure 4.8.

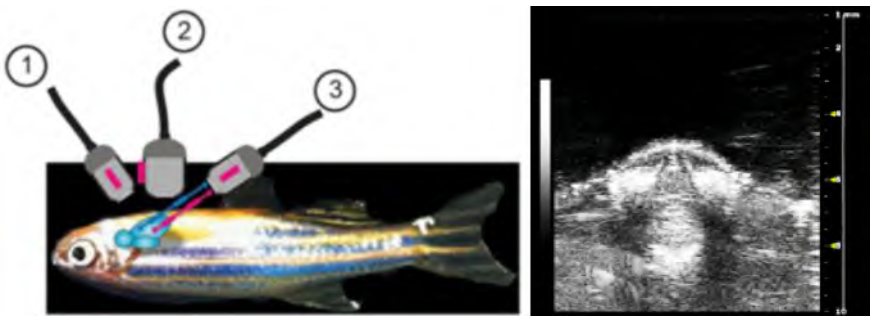

Figure 4.8: Left: schematic illustration of 3 different probe positions resulting in three common views for zebrafish ultrasound imaging of the heart. 1: Short Axis view, 2: Long Axis view and 3: Abdominal-Cranial Axis view. Right: B-mode Short Axis image. Adapted from [162].

B-mode imaging results in a 2D image plane and is used to view (the motion of) larger structures. The denser the tissue, the brighter the gray tone on the image. In zebrafish echocardiography, B-mode imaging is mainly used to examine the ventricle. Fluid-filled spaces appear darker but the moving red blood cells are clearly visible in the heart as moving speckles. B-mode ultrasound imaging in adult zebrafish is illustrated in Figure 4.8 (right panel) and Figure 4.9.

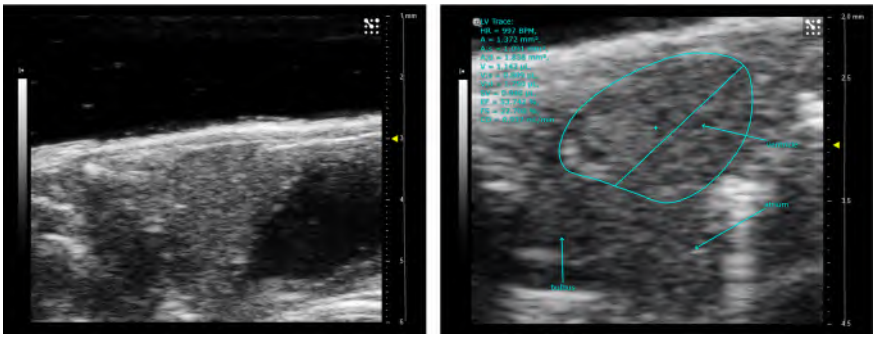

Figure 4.9: B-mode Long Axis images of the heart area in a wider view (left) and zoomed in view of another sample (right). The (motion of the) ventricular wall is traced in blue in the right panel. Images acquired at the Infinity small animal imaging core facility, UGent, using a VEVO 2100 ultrasound machine.

In color Doppler imaging, color information representing the velocity is superimposed onto the 2D B-mode information with blue colors indicating flow away from the probe and red colors indicating flow towards the probe. In adult zebrafish, color Doppler imaging is used to image ventricular in- or outflow (Figure 4.10 and 4.11).

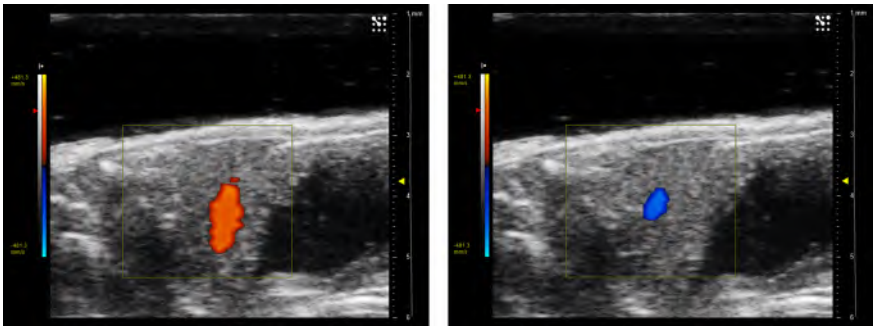

Figure 4.10: Color Doppler Long Axis images of ventricular inflow (left) and ventricular outflow (right). Images acquired at the Infinity small animal imaging core facility, UGent, using a VEVO 2100 ultrasound machine.

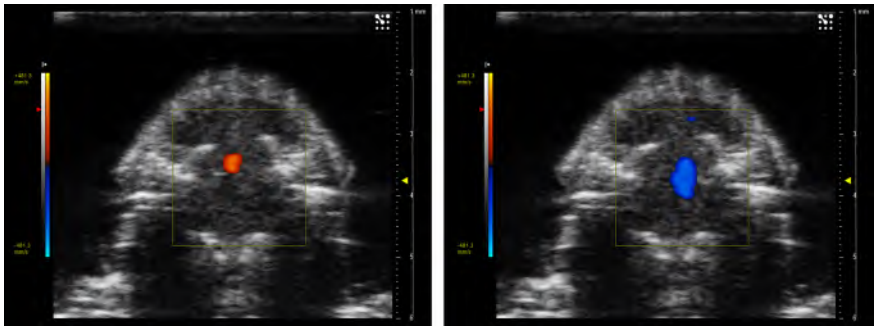

Figure 4.11: Color Doppler Abdominal-Cranial Axis images of ventricular inflow (left) and ventricular outflow (right). Images acquired at the Infinity small animal imaging core facility, UGent, using a VEVO 2100 ultrasound machine.

Pulsed wave Doppler imaging no longer images a 2D area but targets a smaller sample volume where the velocity is measured as a function of time. Again, ventricular in- and outflow are usually imaged in adult zebrafish (Figure 4.12).

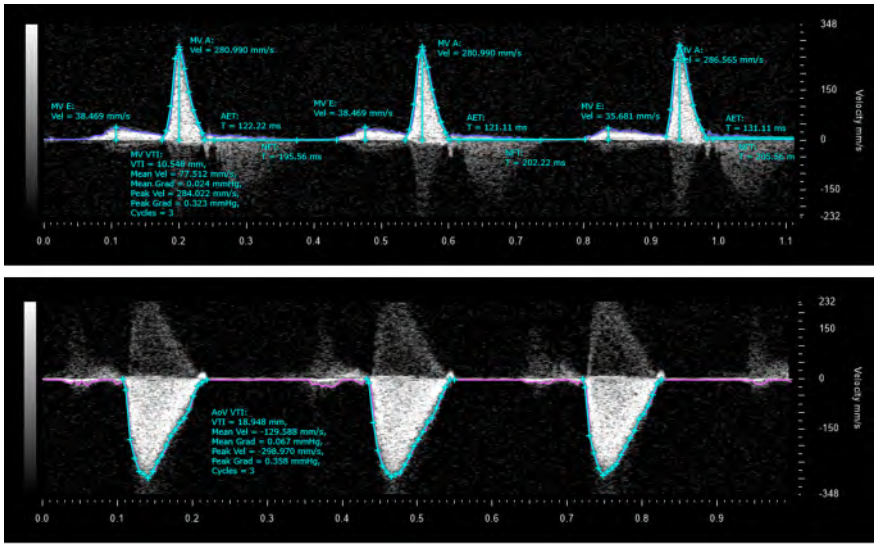

Figure 4.12: Pulsed Doppler images of ventricular inflow (top) and ventricular outflow (bottom). The sample volume for these Pulsed Doppler measurements was selected based on Color Doppler Abdominal-Cranial Axis images. Images acquired at the Infinity small animal imaging core facility, UGent, using a VEVO 2100 ultrasound machine.

In Figure 4.9 (right) and Figure 4.12, post-processing annotations are visible on the ultrasound images. In the presented images, these an-

notations were made by an operator using the VEVO Lab software. The strong importance of a standardized protocol in zebrafish echocardiography was expressed earlier and also the operator-dependency should be minimized, both regarding the measurement itself and regarding the post-processing. To reduce operator-dependency and allow faster processing, post-processing of the measurements is sometimes automated. Automated masking of the zebrafish ventricle on B-mode images has been reported [165]. In human cardiovascular ultrasound, also automated post-processing of Pulsed Wave Doppler measurements is reported but [166, 167] but similar resources in zebrafish were not found at the onset of this PhD.

4.5 Magnetic resonance imaging

4.5.1 General principle

In MRI, a strong magnet is used to align the hydrogen nuclei (single protons) throughout the body with that magnetic field. Subsequently, a pulsed radiofrequency current is applied to spin the protons out of equilibrium. As the protons realign with the magnetic field (due to the radiofrequency current being turned off) energy is released which can be detected by MRI sensors. Different types of tissue can be distinguished on the resulting images because the response of the protons is affected by other atoms to which they are bound. The faster the protons realign with the magnetic field, the brighter the resulting image and contrast agents (e.g., containing Gadolinium) may be administered intravenously before or during the MRI scan to increase the speed at which protons realign. Different slices representing the whole body can be obtained by altering the local magnetic field spatially by small increments. This way, radiofrequency currents of different frequencies will cause different slices throughout the body to resonate.

4.5.2 Magnetic resonance imaging in adult zebrafish

Magnetic resonance imaging allows in vivo recordings in zebrafish, but resolution levels usable for zebrafish cardiovascular research are hard to obtain. Specialized preclinical MRI systems are needed as well as miniature flow chambers to position the zebrafish and allow water perfusion during in vivo imaging. The use of anesthesia is necessary to reduce the motion of the zebrafish during MRI. The first report of zebrafish MRI did not focus on a single organ but describes zebrafish MRI in general [168]. Later, zebrafish MRI, again from a general point of view but at improved resolutions was reported [169].

A number reports focus on the zebrafish brain [170–172]. Recently, ex vivo MRI was used to investigate organ-specific growth abnormalities and both the brain and heart were included [173]. In vivo MRI with a focus on the zebrafish heart was first reported in a study investigating heart regeneration. Advanced MRI (processing) techniques to reduce scan times were used [174]. In the same study also ex vivo MRI in adult zebrafish was performed and a comparison of ex vivo and in vivo or live MRI is presented in Figure 4.13.

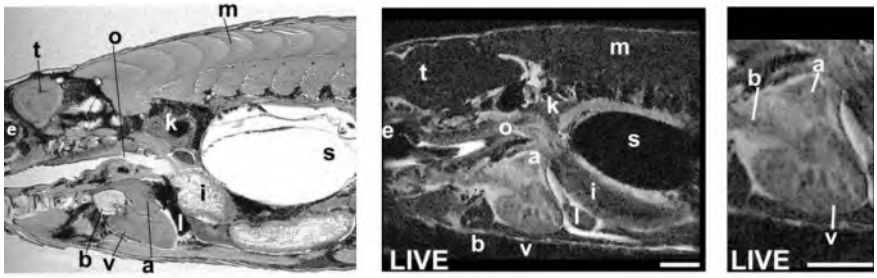

Figure 4.13: In vivo (left) and ex vivo (middle and right) MRI of and adult zebrafish in sagittal images planes. (h) or the whole scan field (i) from eye to mid swim bladder in (sagittal view). Scale bars: mm. a: atrium, b: bulbus arteriosus, e: eye, i: intestine, k: kidney, l: liver, m: muscle, n: olfactory pit, o: oesophagus, p: pharynx, s: swim bladder, t: tectum opticum, v: ventricle. Adapted from [174].

In vivo MRI was used to analyze both luminal and outer wall dilation of the outflow tract or bulbus arteriosus during the cardiac cycle [150]. Images illustrating the obtainable level of detail are presented in Figure 4.14

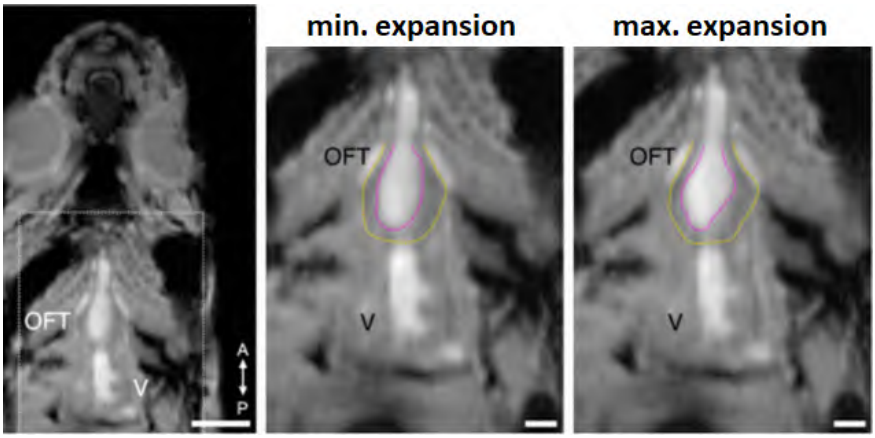

Figure 4.14: Left: single frame of an in vivo MRI cine of a wild-type adult zebrafish in a coronary plane. The white box indicates the zoomed in views in the middle and right image panels. The outer (yellow) in inner (pink) wall of the outflow tract is indicated in the middle (timeframe of minimal expansion of the outflow tract) and right (timeframe of maximal expansion of the outflow tract) image panels. Scale bar (left): 1.5 mm (A), scale bar (middle and right): 500 µm. OFT: outflow tract, V: ventricle, A: anterior, P: posterior. Adapted from [150].

4.6 Histology, microCT, echo and MRI: a comparison

Histology provides most structural details but is a post mortem technique resulting in 2D slices and loss of the sample. 3D information can be obtained using microCT imaging and synchrotron (phase contrast) microCT imaging can provide more tissue details compared to conventional microCT. In vivo CT imaging focusing cardiovascular structures of the adult zebrafish has not been reported. MRI can provide in vivo data, also in 3D, but the soft tissue level of detail is limited. Ultrasound imaging is inherently in vivo but its 3D capabilities (sometimes also referred to as 4D ultrasound counting the time dimension) are very limited for adult zebrafish. Also the spatial (soft tissue) level of detail is very limited in zebrafish ultrasound imaging. Table 4.1 provides a concise comparison of the four mentioned imaging techniques in the context of adult zebrafish cardiovascular research.

Table 4.1: Comparison of selected imaging techniques for adult zebrafish cardiovascular research

Modality	**Histology**	**(Synchr.) microCT**	**Echo**	**MRI**
in vivo ***ex vivo***	*ex vivo*	*ex vivo*	*in vivo*	*in vivo*
2D or 3D	2D	3D	2D	3D
Resolution limit ∼	0.3 x 5 µm	1 x 1 µm	30 x 75 µm	30 x 30 µm
Key reference	[144]	[153]	[163]	[174]

In 2011, both the need and possibilities to image zebrafish at different developmental stages, including adulthood, were explicitly expressed in the context of the Zebrafish Phenome Project [175]. An overview of zebrafish imaging possibilities (focused on whole-animal imaging rather than blood flow imaging) was presented. Almost 15 years later, considerable technical advancements have been made both for histology, microCT, echocardiography and MRI but the key advantages and disadvantages of each of these imaging techniques with respect to each other are still (roughly) the same.

4.7 Other imaging techniques

A few imaging techniques less frequently encountered in adult zebrafish cardiovascular research are grouped in this section.

The use of scanning electron microscopy (SEM) has been reported to visualize the adult zebrafish cardiovascular system, as illustrated in Figure 4.15. SEM can only be used to visualize superficial structures (if coated with an electron-dense material). The internal structures can only be visualised using SEM after physical dissection of the region of interest, making this technique less suited for image-based 3D computational modeling.

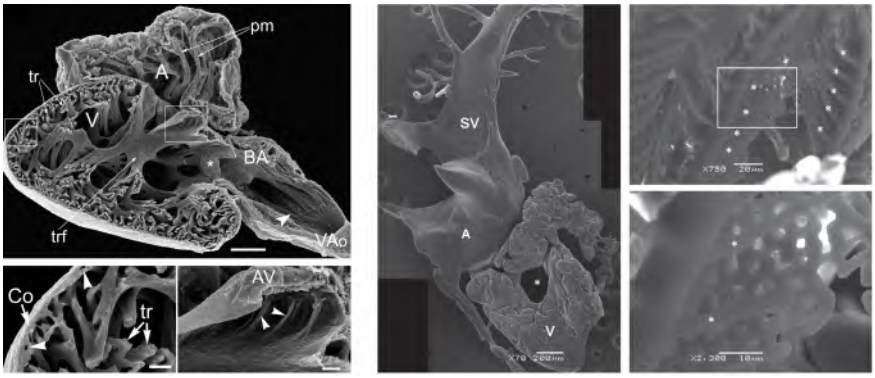

Figure 4.15: Scanning electron microscopy images of the adult zebrafish cardiovascular system. The image panels on the left (adapted from [48]) depict the atrium (A), ventricle (V) and bulbus arteriosus (BA) in the largest image. Zoomed in areas are shown below, focusing on the trabeculated (tr) ventricle and atrioventricular valve (AV). In the image panels on the right (adapted from [10]), a corrosion cast of the adult zebrafish cardiovascular system is scanned, first showing the sinus venosus (SV), atrium (A) and ventricle (V) and on the far right image panels depicting the gill vasculature.

Light-sheet fluorescence microscopy (LSFM) is a very powerful technique for zebrafish research, but mainly suited for developing zebrafish due to their optical transparency. LSFM is a confocal imaging technique but instead of illumination of a single point, a while sheet is illuminated. For developing zebrafish, LSFM can be used to set up in vivo computational models of the developing heart, as illustrated in, e.g., [5] and [91]. In adult zebrafish, two related reports show that after tissue clearing of the (opaque) ventricle, ex vivo LSFM of the adult zebrafish heart is feasible [112] (see also Figure 4.16) and semi-automatic segmentation of the major cardiovascular structures can be performed [113] (see also Figure 4.17).

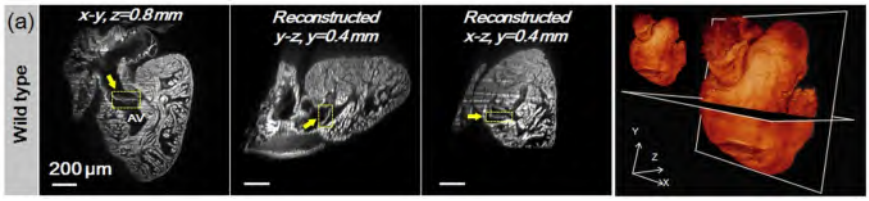

Figure 4.16: Illustration of three different slices (sheets) of the adult zebrafish heart imaged with light-sheet fluorescence microscopy. Tissue clearing was applied before imaging. The panel on the far right renders a 3D reconstruction of the adult zebrafish heart (outer surfaces). Adapted from [112].

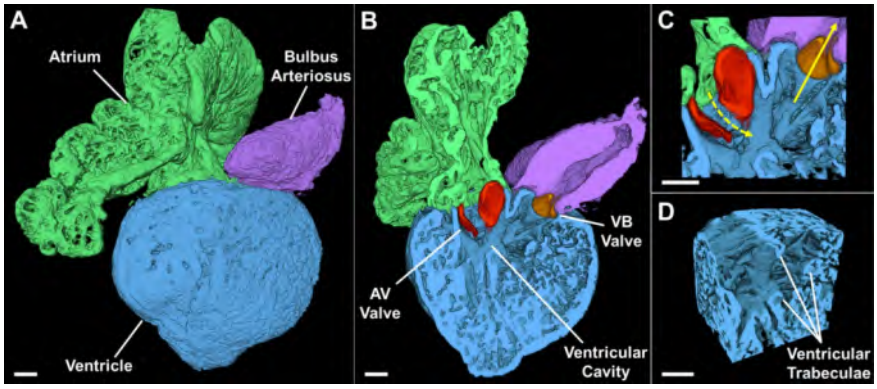

Figure 4.17: Based on the LSFM methodology depicted in Figure 4.16, different adult zebrafish cardiovascular structures can be segmented (semi-)automatically. Adapted from [113].

Also confocal microscopy can be used to set up in vivo computational models of the developing heart, as illustrated in, e.g., [88, 89, 176] but no promising results for (future) image-based 3D computational modeling of the adult zebrafish cardiovascular structures have been reported.

II

Cardiovascular imaging and biomechanical modeling in adult zebrafish

Chapters

CHAPTER 5

Automated pulsed wave Doppler annotation and analysis in adult zebrafish

The work presented in this chapter is based on the publication:

Application of an automated analysis framework for pulsed-wave Doppler cardiac ultrasound measurements to generate reference data in adult zebrafish (**Van Impe, M.**, Caboor, L., Deleeuw, V., De Rycke, K., Vanhooydonck, M., De Backer, J., Segers, P. and Sips, P., AMERICAN JOURNAL OF PHYSIOLOGY REGULATORY INTEGRATIVE AND COMPARATIVE PHYSIOLOGY, 2023) [9].

5.1 Introduction

Commercially available ultrasound systems and probes for preclinical small animal imaging substantially improved over the past 15 years. Brightness mode (B-mode) imaging, visualizing the contracting ventricle, and PWD measurements of ventricular in- and outflow are now widely used to characterize cardiovascular function in adult zebrafish [150, 162]. Several research groups have also explored the use of custom-made ultrasound setups for zebrafish imaging [158, 160, 177, 178]. Overall, high-frequency ultrasound can be considered as a widespread state-of-the-art technique for in vivo adult zebrafish cardiovascular research [163, 164].

Specialized commercial software such as Vevo LAB (FUJIFILM VisualSonics, Toronto, Ontario, Canada) can be used to trace the PWD signals automatically but different points of interest, including peaks and time intervals, still need to be characterized by manual point indications on the recording. Analyzing zebrafish ultrasound measurements therefore usually requires a considerable amount of dedicated hands-on time. In addition, the reported interindividual variability regarding cardiovascular (patho)physiological parameters between zebrafish of the same sex, age and genotype complicates accurate PWD based phenotyping [150]. One way to address this variability is to analyze larger numbers of individuals per group, but this leads to considerably longer analysis times. On the other hand, out of practical considerations only a limited number of cardiac cycles collected in one recording (often as small as three) is selected for analysis [163], resulting in an undersampling of the recorded data which could lead to an unintended bias due to the existing beat-to-beat variability within one recording. Increasing the number of analyzed cardiac cycles per recording improves the accuracy of the (per sample averaged) results and allows the detection of (phenotypic) variability and irregularities but unfortunately this is usually not feasible for large-scale experiments.

The general topic of (PWD) ultrasound processing automation has gained interest in humans [166, 179], but no studies that fully automatically provide an extensive set of PWD parameters in zebrafish were found. Zebrafish are often used to study genetic cardiovascular diseases, which are frequently associated with variable phenotypic expression [180]. Therefore, to maximize the relevance of the disease model a comprehensive understanding of the cardiovascular phenotype is required, which necessitates the efficient extraction of as much relevant information as possible from a relatively large sample size.

In this study, we present a fully automated framework to process PWD adult zebrafish echocardiography measurements, allowing the evaluation of all cardiac cycles in a large number of recordings without operator-dependent inputs. An automatic analysis of irregularities, correlations and statistical differences is integrated as well. The method operates on DICOM data which is available from ultrasound equipment used for routine small animal cardiac ultrasound present in most specialized labs. We applied this algorithm to a large number of ultrasound measurements in both male and female wild-type adult zebrafish of varying ages to validate the framework and we both confirm existing findings and discuss previously unreported correlations.

The reference measurement set provided in this study can be used as a benchmark for future projects.

5.2 Methods

5.2.1 High-frequency pulsed wave Doppler ultrasound imaging

A Vevo 2100 ultrasound machine (FUJIFILM VisualSonics, Toronto, Ontario, Canada) and MS 700 linear array probe (FUJIFILM VisualSonics, Toronto, Ontario, Canada) were used to perform the echocardiography experiments. The probe has a frequency range of 30 - 70 MHz and a center frequency of 50 MHz. Anesthesia was induced by immersing the zebrafish in a 0.16 $\mathrm{g\,L^{-1}}$ tricaine methanesulfonate (MS-222) solution at 28°C until a lack of response to external stimuli was observed. Next, the zebrafish were transferred to a new 0.08 $\mathrm{g\,L^{-1}}$ tricaine methanesulfonate solution at 28°C to maintain anesthesia during the experiment, while minimizing the impacts of anesthesia on the cardiovascular parameters.

All measurements were obtained within 3-4 minutes after the start of anesthesia induction. PWD measurements of ventricular in- and outflow were recorded with the probe in an abdominocranial short axis configuration at a 45° angle towards the abdominal wall (Figure 5.1 b). In between measurements in different individuals, the solutions were returned to a 28°C temperature-controlled water bath to maintain a constant temperature during the ultrasound measurements throughout the experiment.

A customized 3D printed holder, filled with the 0.08 $\mathrm{g\,L^{-1}}$ tricaine solution and including spongy (submerged) clamps, was used to stabilize the zebrafish during echocardiography (Figure 5.1 a and Figure 5.1 b). Note that both the spongy end of the sliding part and the complete fixed part are submerged in water inside the box during the experiment (Figure 5.1 a).

Figure 5.1 c and Figure 5.1 d illustrate representative Doppler angles corresponding to measurements of ventricular in- and outflow, respectively. The yellow arrowhead indicates the focal zone. A typical inflow (atrioventricular valve flow) signal (AV flow) is shown in Figure 5.2 (top) and annotations of the atrial peak (A peak), atrial velocity time integral (A VTI), early peak (E peak), early velocity time integral (E VTI), inflow regurgitation (A regurg), heart rate (HR), aortic

ejection time (AET) and no flow time (NFT) are provided. A typical outflow (aortic valve flow) signal (AoV flow) is shown in Fig 5.2 (bottom) and annotations of the outflow peak (Ao peak), outflow velocity time integral (Ao VTI) and outflow regurgitation (Ao regurg) are provided. Also the aortic ejection time (AET) and heart rate (HR) can be evaluated based on the outflow signal. An overview of all used PWD parameters is provided in Table 5.1.

Table 5.1: Overview of the parameter abbreviations describing pulsed wave Doppler measurements of ventricular in- and outflow, i.e., atrioventricular valve (AV) flow and aortic valve (AoV) flow, respectively.

Parameter	**Unit**	**Description**
A peak	mm/s	Peak (maximum) value of the atrial wave (ventricular inflow)
A VTI	mm	Velocity time integral of the atrial wave (ventricular inflow)
A regurg	mm/s	Peak (maximum) value of the atrioventricular valve regurgitation
E peak	mm/s	Peak (maximum) value of the early wave (ventricular inflow)
E VTI	mm	Velocity time integral of the early wave (ventricular inflow)
AET	ms	Aortic ejection time, i.e., the duration the aortic valve is opened
NFT	ms	No flow time, i.e., the duration the atrioventricular valve is closed
HR	bpm	Heart rate, either based on the peak locations of the atrial or aortic wave
Ao peak	mm/s	Peak (maximum) value of the outflow wave (ventricular outflow)
Ao VTI	mm	Velocity time integral of the outflow wave (ventricular outflow)
Ao regurg	mm/s	Peak (maximum) value of the aortic valve regurgitation

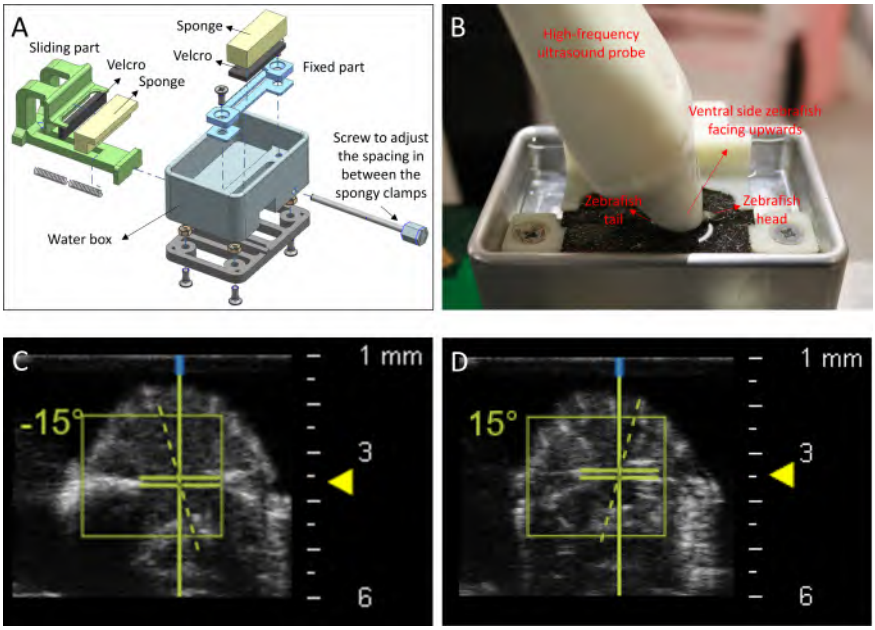

Figure 5.1: Representative pulsed wave Doppler (PWD) measurements of ventricular in- and outflow in adult zebrafish. **A** Schematic drawing of a customized holder to stabilize the zebrafish during echocardiography experiments. **B** 3D printed holder based on the schematic in panel A. The holder is filled with water and the submerged zebrafish is stabilized by the spongy clamps. The probe is oriented in an abdominocranial short axis configuration at a 45° angle towards the abdominal wall for PWD measurements. **C** Abdominocranial view with an indication of the Doppler angle for PWD measurements of ventricular inflow. **D** Abdominocranial view with an indication of the Doppler angle for PWD measurements of ventricular outflow.

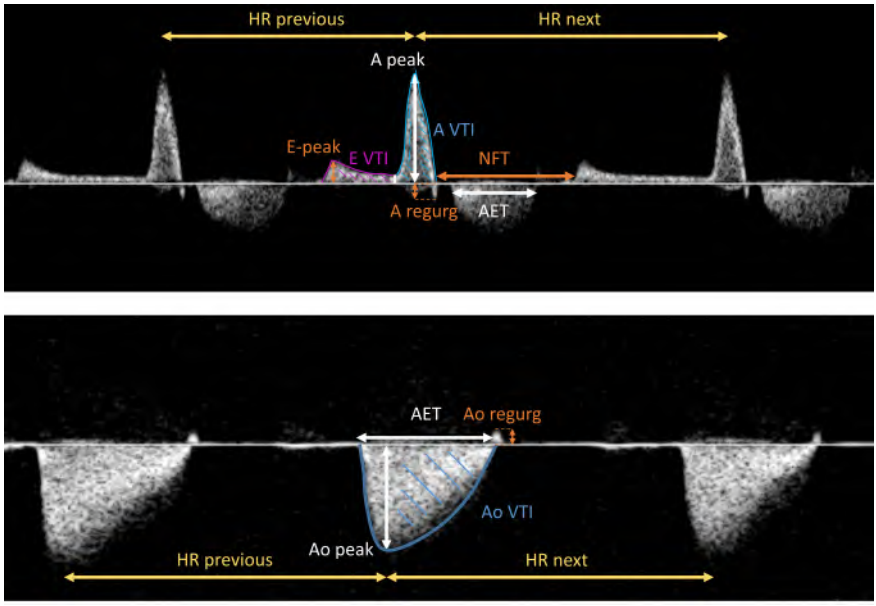

Figure 5.2: Representative pulsed wave Doppler (PWD) measurements of ventricular in- and outflow in adult zebrafish. Top: PWD inflow measurement showing three cardiac cycles. Bottom: PWD outflow measurement showing three cardiac cycles. A: atrial wave, E: early wave, Ao: aortic wave, VTI: velocity time integral, regurg: regurgitation, AET: aortic ejection time, NFT: no flow time, HR: heart rate. Note that the indication (in yellow) of HR in this figure actually corresponds to the time interval (cardiac cycle duration) used to calculate the heart rate.

5.2.2 Zebrafish (*Danio rerio*)

The ultrasound data originates from experiments performed in a 1.5 year timeframe on N = 80 wild-type (AB background) animals (63 males and 17 females). The ages of the different groups range between 9 and 21 months. All zebrafish experiments were conducted in strict accordance with the FELASA (Federation of European Laboratory Animal Science Associations) guidelines and recommendations for the care and use of laboratory animals. Full approval by the local ethical committee was obtained and all applicable international, national and institutional guidelines for the care and use of animals and the conduction of animal experiments, including the Directive 2010/63/EU, were followed.

5.2.3 Automated processing of pulsed wave Doppler measurements

The DICOM data of the inflow (AV flow) and outflow (AoV flow) PWD signals of all samples was imported in MATLAB (MathWorks,

Natick, Massachusetts, USA) and processed with custom, newly developed algorithms. Below, we summarize the key aspects of the fully automated algorithms to process PWD measurements of ventricular in- and outflow (two separate algorithms). A simplified schematic overview is presented in Figure 5.3. For all details on the procedure, functions used and parameter settings, we refer to the code, including comments to improve readability, which is openly available at Zenodo.

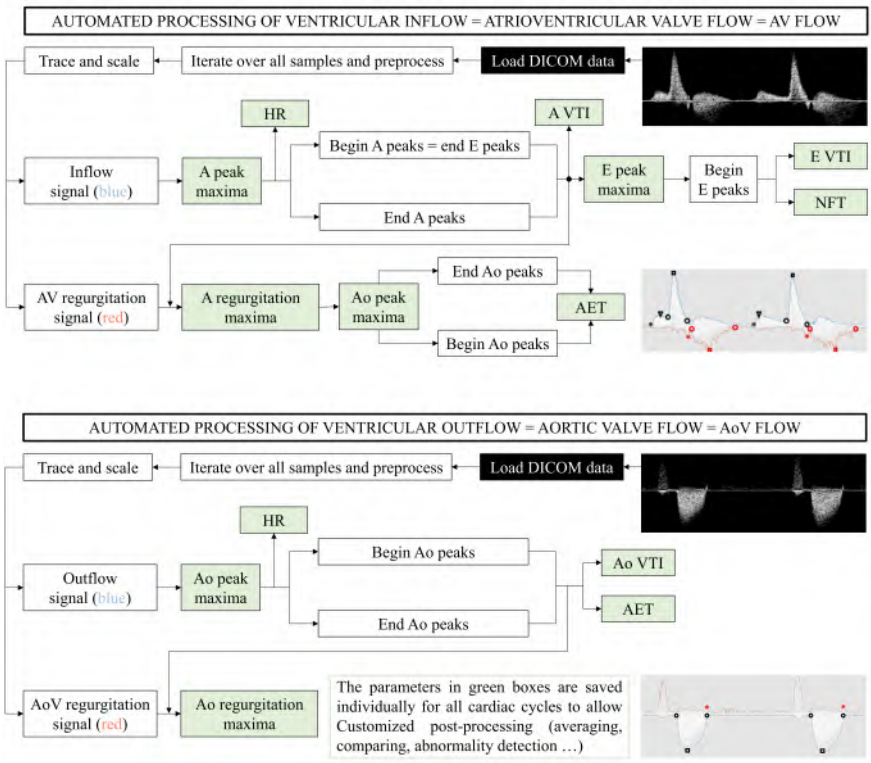

Figure 5.3: Schematic overview of the custom developed algorithms to automatically process adult zebrafish pulsed wave Doppler (PWD) measurements of ventricular inflow (top half) and outflow (bottom half). Parameters in green boxes are used in the current post-processing pipeline. Both for the inflow and outflow processing algorithm, a representative PWD measurement is shown top right and the traced signals and points of important are overlaid on the bottom right images. Ao: aortic wave (ventricular outflow), A: atrial wave (ventricular inflow), E: early wave (ventricular inflow), VTI: velocity time integral, regurg: regurgitation, AET: aortic ejection time, NFT: no flow time, HR: heart rate.

For the inflow measurement, the actual inflow signal is situated above the zero line, i.e., the horizontal line visible in Figure 5.2 (top). On

the signal below the zero line, immediately after the atrial wave, the AV regurgitation peak can be detected. Note that (a part of) the (aortic) outflow is often also visible on the signal below the zero line, after the AV regurgitation peak of the ventricular inflow. In the inflow processing algorithm, the DICOM data is first (pre)processed to trace and scale both the signal above and the signal below the zero line based on gray value thresholding and common edge detection principles. For each point in time (horizontal axis), the signal value (vertical axis) is searched row by row starting at the zero line. To trace the signal, one of several conditions has to be met; either comparing a single pixel to a gray value threshold or comparing the average of multiple pixels (rows) to a (lower) threshold. All threshold values are (for each sample) determined by the intensity of the first pixels (rows) close to the zero line. Smoothing was applied to obtain the final trace.

To start the actual extraction of points of interest, the A peak maxima and afterwards also the beginning and end of all A peaks are detected (i.e., the beginning and end of the atrial waves). HR and A VTI are then calculated based on the detected points and available trace. The aortic outflow peak maxima are detected on the signal of the inflow measurement below the zero line (i.e., on the outflow traces visible in the inflow recording), and afterwards also the beginning and end of all outflow peaks are detected to calculate the AET. Next, the regurgitation peaks A regurg (maxima) are detected below the zero line in predetermined windows based on the end of the atrial wave and the beginning of the AET. Next, switching again to the inflow signal above the zero line, the E peak maxima are detected in predetermined windows based on the end of the AET and the beginning of the A peak. Afterwards also the beginning of the E peaks is detected. E VTI and NFT can now be calculated based on the detected points and available trace. Note that the initially obtained A peak and E peak values are multiplied with correction factors of 1.05 and 1.10, respectively, to compensate for the smoothing of (sharp) peaks during the signal tracing. In total, eight AV flow parameters (A peak, A VTI, A regurg, E peak, E VTI, HR, AET and NFT) are saved individually per sample and per cardiac cycle to allow customized post-processing.

For the outflow measurement, the actual outflow signal is situated below the zero line, i.e., the horizontal line visible in Figure 5.2 (bottom). On the signal above the zero line, immediately after the aortic wave, the AoV regurgitation peak can be detected. In the outflow

processing algorithm, the DICOM data is first (pre)processed to trace and scale both the signal below and the signal above the zero line based on gray value thresholding and common edge detection principles as described for the inflow measurement. To start the actual extraction of points of interest, the Ao peak maxima and afterwards also the beginning and end of all Ao peaks are detected. Ao VTI, HR and AET can now be calculated based on the detected points and available trace. Using the signal above the zero line, the regurgitation peaks Ao regurg (maxima) are detected in predetermined windows around the end of the aortic wave. In total, five AoV flow parameters (Ao peak, Ao VTI, Ao regurg, HR and AET) are saved individually per sample and per cardiac cycle to allow customized post-processing.

5.2.4 Manual processing of pulsed wave Doppler measurements

Manually processed results of 24 out of the 80 samples, analyzed in Vevo LAB (FUJIFILM VisualSonics, Toronto, Ontario, Canada) by an experienced operator (L.C.), were used to quantitatively validate the automatically processed results. For these 24 samples, six AV flow parameters (A peak, A VTI, A regurg, E peak, AET and NFT) and three AoV flow parameters (Ao peak, Ao VTI and Ao regurg) were manually evaluated and annotated in three consecutive cardiac cycles, selected by the operator. All steps were performed without knowledge of the automated processing results ensuring unbiased manual processing.

5.2.5 Validation and comparison: automated versus manual pulsed wave Doppler processing

The manually processed parameter values (nine PWD parameters, all evaluated in 24 samples for three cardiac cycles per sample) and the corresponding automated results were compared quantitatively. R-squared values of the automated results with respect to a perfect fit to the manual results as well as Bland-Altman (also known as Tukey mean-difference) plots were calculated. In the Bland-Altman plots, the average of the manual and automated result was used as independent variable while the difference of the automated result minus the manual result was taken as the dependent variable. For all 80 samples, a visual quality check of all automated results was performed to evaluate the detection of the points and traces of interest.

5.2.6 Statistics

Throughout this work, one-sample t-tests and two-sample t-tests (both two-tailed) were used and correlations were always evaluated using a Pearson's correlation analysis. For all statistical tests, an initial significance level α=0.05 was used but because in many cases multiple hypotheses were tested, the Bonferroni correction for multiple testing was used to calculate the adjusted alpha-level according to Eq. 5.1:

$$\alpha_{adj} = \frac{\alpha}{N_{tests}} \tag{5.1}$$

where N_{tests} is the total number of tests part of a specific analysis and α_{adj} is the resulting adjusted alpha-level.

In several analyses and statistical tests, certain PWD parameters were first normalized with respect to body surface area (BSA). BSA was defined by Eq. 5.2:

$$\mathrm{BSA}[\mathrm{cm}^2] = 8.46 \cdot (\frac{\mathrm{Weight}[\mathrm{mg}]}{1000})^{0.66} \tag{5.2}$$

as validated by [181] for fish similar to zebrafish regarding size and shape. If a PWD parameter showed a significant correlation with BSA, normalization with respect to BSA was performed for all (following) analyses. For each sample, a (dimensionless) BSA normalization factor was calculated by dividing the sample BSA by the group mean BSA. BSA normalized PWD parameters were obtained by dividing the original PWD parameter by the BSA normalization factor.

5.3 Results

5.3.1 Validation of automated pulsed wave Doppler processing

Data from 24 samples was used to perform a validation study of the automated workflow. First, all automated annotations on the images were qualitatively (visually) validated and overall an excellent accuracy was obtained. When evaluating the images, we saw that for one sample the (start of the) early wave was very hard to distinguish and this was also noted during the manual annotation performed by an experienced operator. The NFT, E peak and E VTI values of this sample were excluded both from the quantitative validation analyses in the next paragraph and all following analyses. For one PWD parameter, AV (in)flow based AET, the automated annotations were

visually incorrect for a number of samples. For these samples, the aortic ejection signal part in the inflow recording was very noisy or only partially visible, as illustrated in Figure 5.6. Note that for these recordings, also a manual AET annotation is not straightforward.

We also performed a quantitative validation study for nine PWD parameters (Ao peak, Ao VTI and Ao regurg from outflow recordings and A peak, A VTI, E peak, E VTI, A regurg, AET and NFT from inflow recordings) based on the same 24 samples. Please note that the fact at this point the AET values are based on the inflow recording is important, since these values are also (and more clearly) available on outflow recordings. Using the inflow recording was our standard approach before this study as also the NFT is delineated on the inflow recording and sometimes both parameters are combined to calculate the myocardial performance index. In Figure 5.4, the relationship between the manual result (independent variable) and automated result (dependent variable) is displayed for nine PWD parameters. Data from 24 samples is used and a total of 72 data points (cardiac cycles) is plotted. The R-squared value is calculated with respect to first quadrant bisector (diagonal black lines) for each comparison. In Figure 5.5, Bland-Altman plots are displayed for the same parameters and data points.

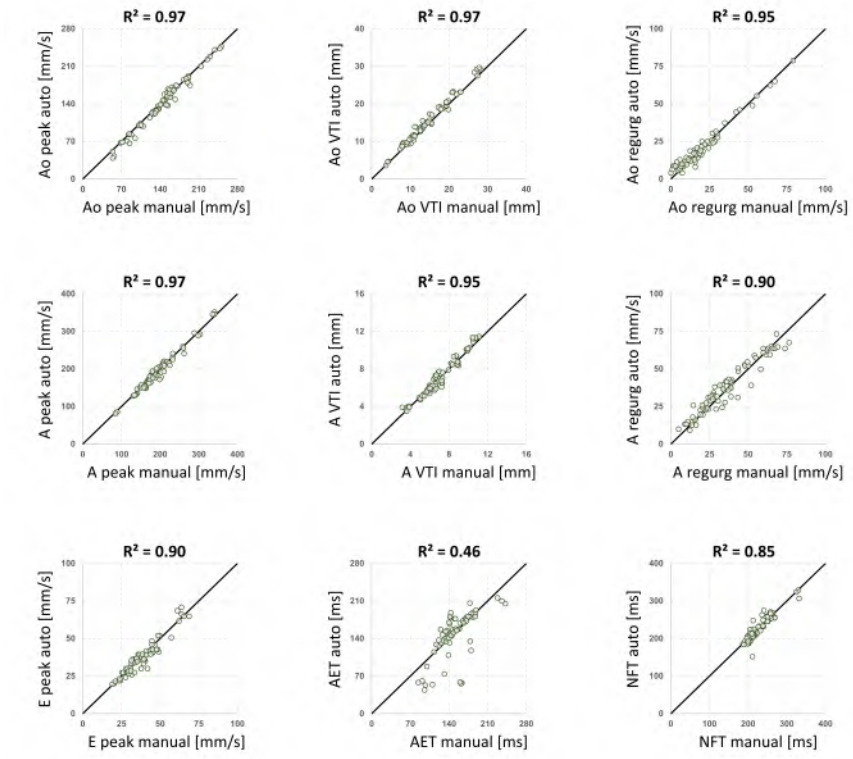

Figure 5.4: Agreement between manually and automatically processed parameters of both ventricular outflow adult zebrafish pulsed wave Doppler (PWD) measurements (top row) and ventricular inflow PWD measurements (middle and bottom row). In each panel, the diagonal black line represents a perfect agreement and the R-squared values displayed at the top of each panel were calculated with respect to this perfect fit. Ao: aortic wave (ventricular outflow), A: atrial wave (ventricular inflow), E: early wave (ventricular inflow), VTI: velocity time integral, regurg: regurgitation, AET: aortic ejection time, NFT: no flow time.

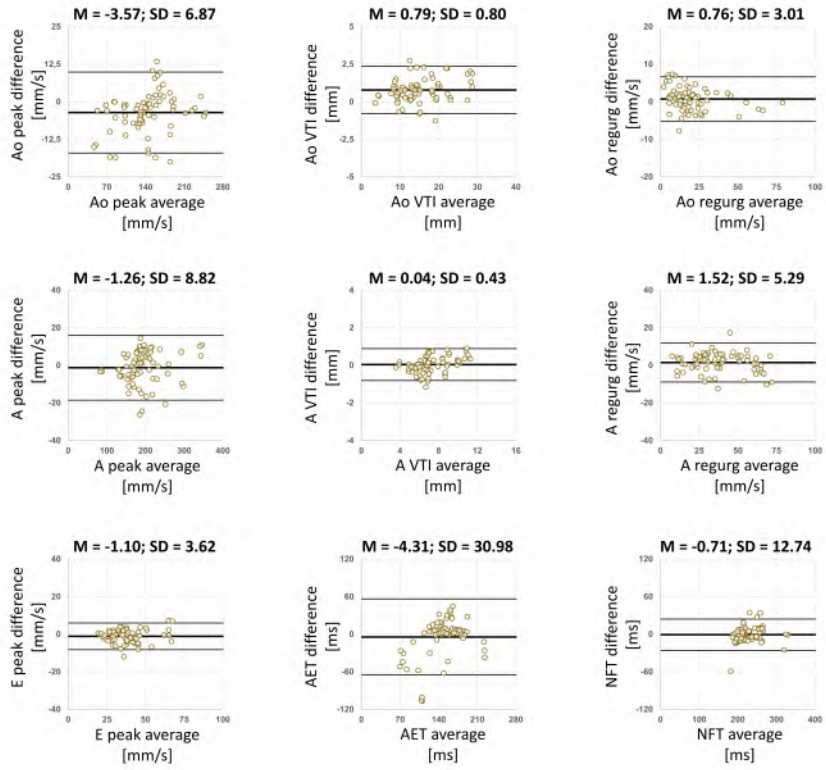

Figure 5.5: Bland-Altman plots to compare (differences between) manually and automatically processed adult zebrafish pulsed wave Doppler (PWD) parameters of both ventricular outflow (top row) and inflow (middle and bottom row). The average of the automatic and manual results is the independent variable (horizontal axis) while the difference of the automatic minus the manual result is the dependent variable (vertical axis). In each panel, the central (thick) solid black line corresponds to the average difference, the outer solid black lines indicate the average difference plus or minus 1.96 standard deviations of the difference. M: mean, SD: standard deviation, Ao: aortic wave (ventricular outflow), A: atrial wave (ventricular inflow), E: early wave (ventricular inflow), VTI: velocity time integral, regurg: regurgitation, AET: aortic ejection time, NFT: no flow time.

For the maximum values (Ao peak, Ao regurg, A peak, A regurg and E peak), R-squared values between 0.90 and 0.97 were obtained and for the velocity time integrals (Ao VTI and A VTI), R-squared values of 0.97 and 0.95 were obtained. For the AET and NFT, the R-squared values were 0.46 and 0.85, respectively. For the AET, a considerably lower R-squared value was observed compared to all other PWD parameters. This mismatch present for certain samples between the

automated and manual annotations could (mainly) be allocated to inaccurate automated annotations, often present in samples for which the aortic ejection signal in the inflow recording was very noisy.

5.3.2 Reference data in wild-type adult zebrafish

After validation of the automated analysis pipeline, we applied it to analyze the measurements of an additional 56 zebrafish, adding up to a total of 80 samples, resulting in the analysis of 3839 cardiac cycles from ventricular inflow measurements and 1643 cardiac cycles from ventricular outflow measurements. The higher number of beat-to-beat inflow measurements is due to the increased total length of inflow PWD recordings (on average 19.0 seconds) as compared to outflow recordings (on average 8.1 seconds). A part of the in- and/or outflow recording of a limited number of samples was automatically excluded and not analyzed due to insufficient or inconsistent measurement quality. A qualitative (visual) accuracy check of the automated annotations was performed for all samples, overall showing excellent results for all PWD parameters except for the AV flow based AET. We identified 14 samples for which the automated AV flow based AET detection was insufficient (examples shown in Figure 5.6 but a fairly good accuracy was observed for the remaining 66 samples. We have made the automatically annotated images of our complete dataset as well as a detailed numerical overview summarizing all automatically evaluated PWD parameters together with age, sex, BSA and the time difference between the start of the outflow and inflow recording for all samples available at Zenodo.

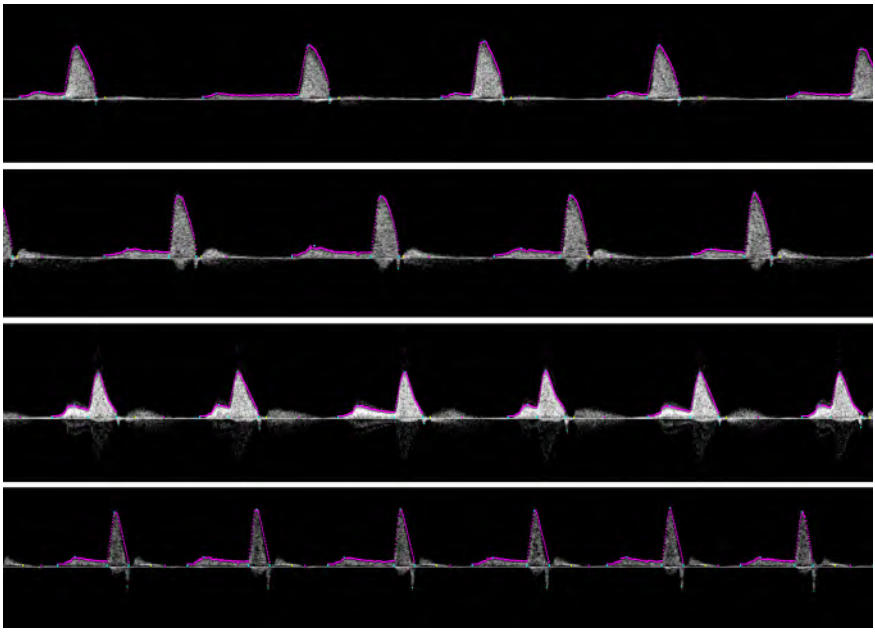

Figure 5.6: Examples of automatically annotated zebrafish pulsed wave Doppler recordings of ventricular inflow for which the aortic ejection time could not be detected accurately. Sometimes, the aortic outflow is very noisy or barely visible on the inflow recording. All four of these samples were excluded when comparing the aortic ejection time between inflow and outflow recordings (a total of 14 out of the 80 samples were excluded).

5.3.3 Time effects

Figure 5.7 illustrates beat-to-beat variability commonly present in the recordings. Qualitatively, the most pronounced variations were observed for the duration of the early wave, HR and NFT but also for other variables, substantial beat-to-beat variations are sometimes present. Note that also in Figure 5.6 beat-to-beat variability is clearly present.

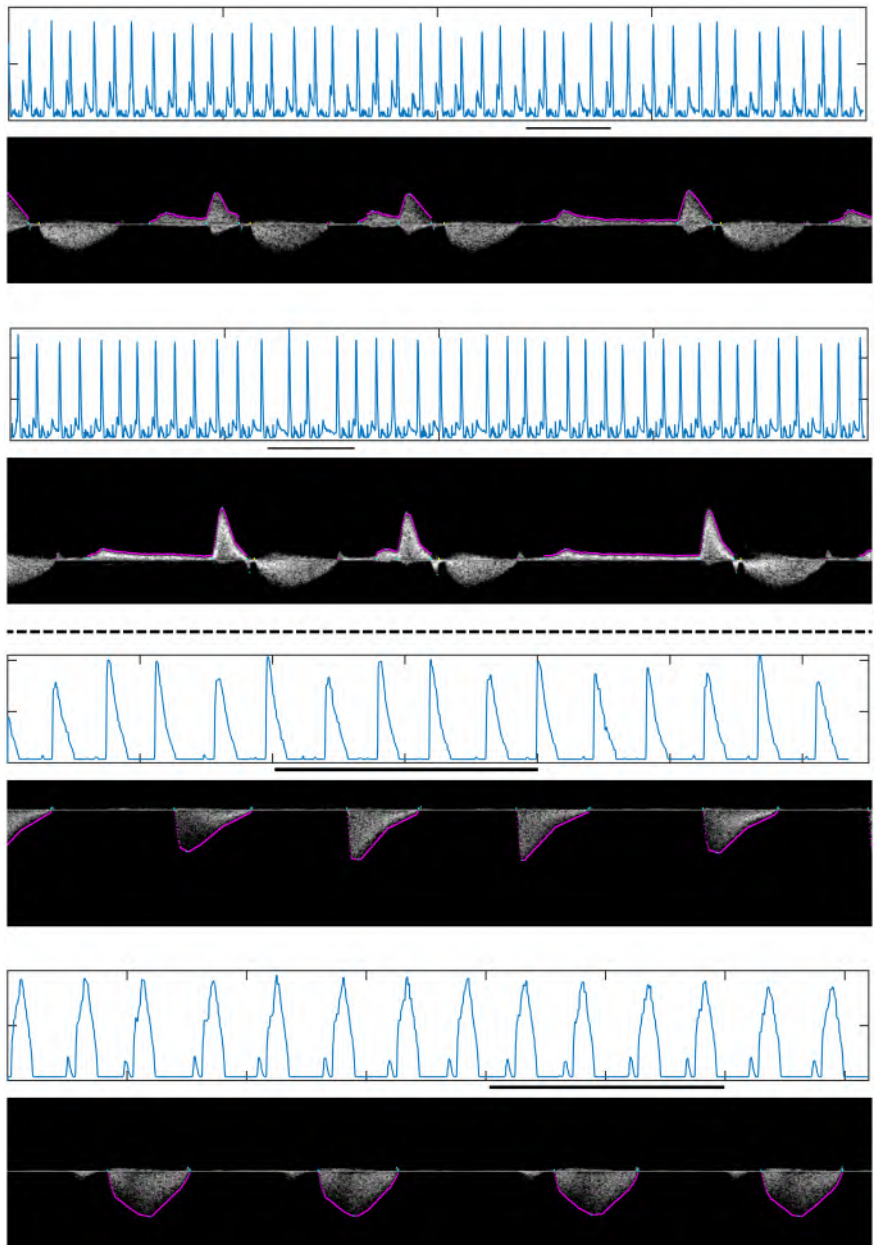

Figure 5.7: Illustration of observed beat-to-beat variations. Top half: the blue signals depict two complete inflow recordings of approximately 20 seconds. The black bars indicate the part of the signal shown directly below the boxed blue signal. Bottom half: the blue signals depict two complete outflow recordings of approximately 7 seconds. The black bars indicate the part of the signal shown directly below the boxed blue signal.

We investigated whether HR and inflow and outflow peak values remained stable (on average) throughout the (short) duration of a single ultrasound recording (approximately 20 seconds for inflow recordings and 7 seconds for outflow recordings). To this end, we evaluated the PWD measurements as a function oftime, and one-sample t-tests confirmed that none of the slopes of the fitted trendlines (i.e., evolution of A peaks, Ao peaks, atrial wave-based HR and aortic wave-based HR over time in a recording) were significantly different from zero.

On a longer time scale, order of minutes, it can be expected that anesthesia has an impact on cardiovascular parameters, especially HR [163, 182]. Therefore, we examined to what extent the order of and time in between the inflow and outflow PWD measurements (available from the DICOM data) affects the PWD parameters that were extracted from both recordings (AET and HR). We found that HR mildly but significantly decreased between the two measurements (taken approximately 1 minute apart) for one zebrafish, while no significant correlation was observed between the time difference and AET difference (Figure 5.8).

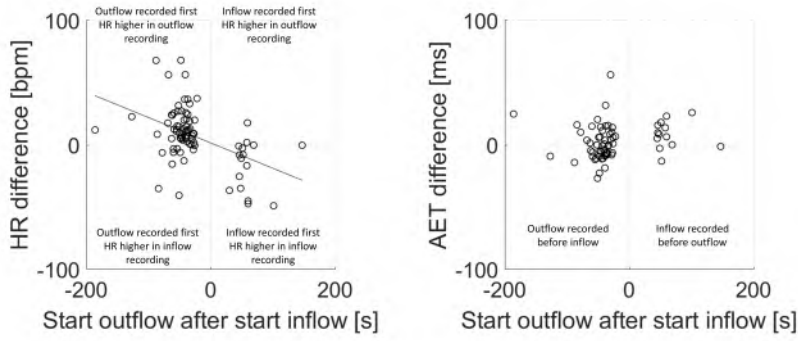

Figure 5.8: Difference in heart rate (HR, left panel) and aortic ejection time (AET, right panel) defined as the values from the outflow recording minus the values from the inflow recording of the same samples. In the X-axis the time difference between the start of the inflow and the start of the outflow PWD measurement is indicated. On average, a higher HR is observed for the recording that was measured first and the HR difference significantly correlates with the time difference between the start of the inflow and outflow measurement (R = -0.46). The AET difference does not significantly correlate with the time difference between the start of the inflow and outflow measurement (R = 0.16). R: Pearson correlation coefficient.

We also compared the values of (recording averaged) HR and AET of inflow versus outflow recordings and one-sample t-tests revealed that the mean difference was significantly different from zero for HR (N = 80) but not for AET (N = 66 as only the samples with accurate AV flow based AET were included). In subsequent analyses, AV flow based HR was used if combined with other AV flow based PWD parameters. Similarly, AoV flow based HR was used if combined with other AoV flow based PWD parameters. The average of AV flow based HR and AoV flow based HR was used if combined with BSA, age or sex. For the aortic ejection time, AoV flow based AET was used in all subsequent analyses.

5.3.4 Normalizing PWD parameters with respect to body surface area

The maximum heights of the aortic wave, the aortic regurgitation, the atrial wave and the atrial regurgitation (Ao peak, Ao regurg, A peak and A regurg) all correlated significantly with the BSA of the zebrafish measured (Figure 5.9) and were normalized with respect to BSA for the rest of this study. The aortic ejection time, the different velocity time integrals, the maximum height of the early wave, the no flow time and heart rate (AET, Ao VTI, A VTI, E VTI, E peak, NFT and HR) did not correlate with BSA (Figure 5.9).

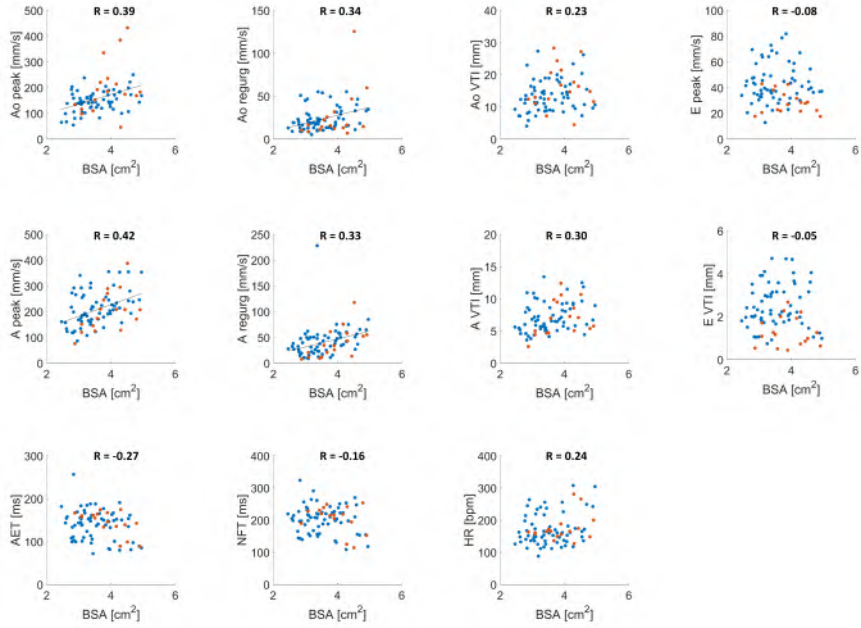

Figure 5.9: Distribution plots (N = 80 samples) of analyzed adult zebrafish pulsed wave Doppler (PWD) parameters all plotted versus body surface area (BSA). Pearson correlation coefficients (R) are displayed for all correlations while the trendline is only shown for significant correlations. A significance threshold $\alpha_{adj} = 0.0045$ was used after correcting for multiple testing ($N_{tests} = 11$), corresponding to R > 0.315 or R < - 0.315 as the limit values for significant correlations. Ao: aortic wave (ventricular outflow), A: atrial wave (ventricular inflow), E: early wave (ventricular inflow), VTI: velocity time integral, regurg: regurgitation, AET: aortic ejection time, NFT: no flow time, HR: heart rate. Color legend - blue: male samples, red: female samples.

5.3.5 Correlations between PWD parameters

A simplified overview of all correlations between different PWD parameters is provided in Figure 5.10 by mapping and dividing the R-coefficients into five color levels. Next to correlations between different PWD parameters also correlations with age are included.

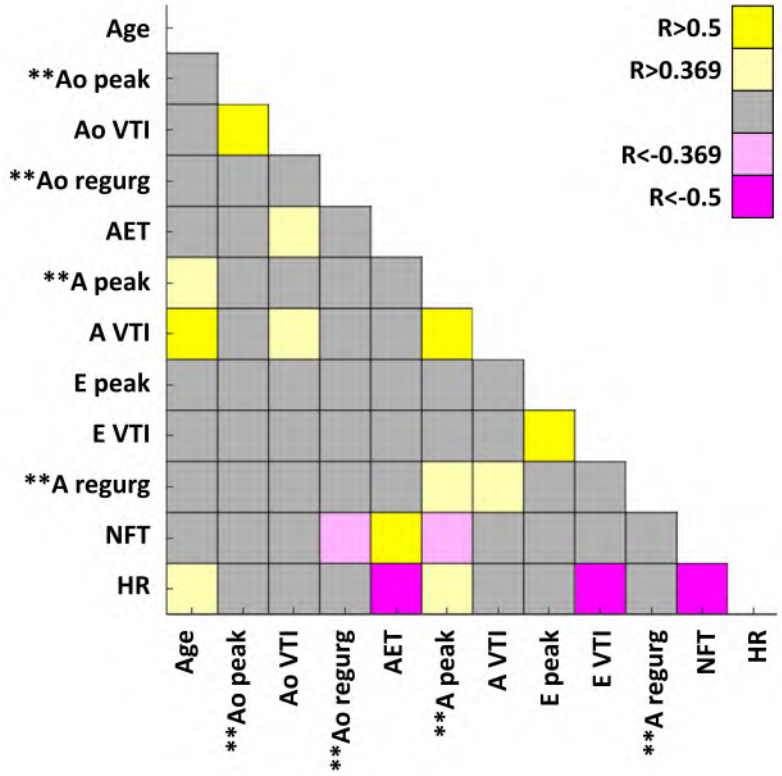

Figure 5.10: Overview of correlations between automatically analyzed PWD parameters as well as age of the zebrafish (N = 80). Variables preceded by two asterisks (**) were normalized with respect to body surface area before the correlation analysis. A significance threshold $\alpha_{adj} = 0.00076$ was used after correcting for multiple testing ($N_{tests} = 66$), corresponding to R > 0.369 or R < - 0.369 as the limit values for significant correlations. Arbitrary correlation limits R = ± 0.5 were used to visualize the strongest correlations. Ao: aortic wave (ventricular outflow), A: atrial wave (ventricular inflow), E: early wave (ventricular inflow), VTI: velocity time integral, regurg: regurgitation, AET: aortic ejection time, NFT: no flow time, HR: heart rate.

Age and A peak, age and A VTI as well as age and HR are correlated positively.

Strong correlations were found between the maximum height and velocity time integrals of the same waves (Ao peak-Ao VTI, A peak-A VTI and E peak-E VTI all correlated positively). Significant positive correlations were also observed between A regurg and both A peak and A VTI, but not between Ao regurg and Ao peak or Ao VTI. Also Ao VTI and A VTI are correlated positively but no correlations

between Ao peak-A peak, Ao regurg-A regurg, A peak-E peak or A VTI-E VTI were observed. All relations between the peak values, regurgitation values and velocity time integrals mentioned in this paragraph are displayed in detail in Figure 5.11.

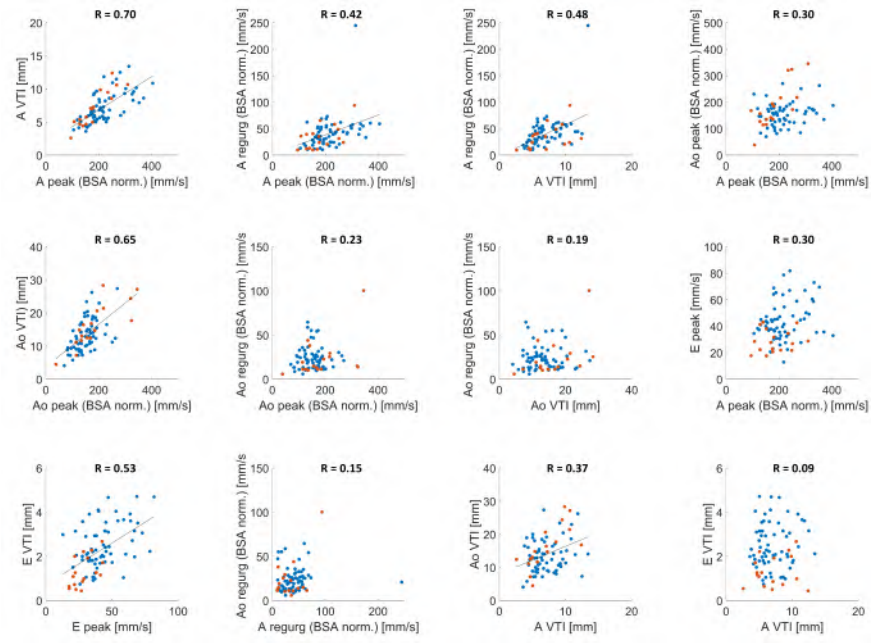

Figure 5.11: Distribution plots (N = 80 samples) displaying the relation between analyzed peaks and peak areas of adults zebrafish pulsed wave Doppler (PWD) parameters. Pearson correlation coefficients (R) are displayed for all correlations while the trendline is only shown for significant correlations. The presented correlations were analyzed as part of a larger correlation analysis (Figure 8) thus the significance threshold was based on the number of tests of the larger correlation analysis (leading to α_{adj} = 0.00076 which corresponds to R > 0.369 or R < - 0.369). Ao: aortic wave (ventricular outflow), A: atrial wave (ventricular inflow), E: early wave (ventricular inflow), VTI: velocity time integral, regurg: regurgitation. Color legend - blue: male samples, red: female samples.

Next to the (expected) strong correlations between heart rate and the aortic ejection time as well as between heart rate and the no flow time (HR-AET and HR-NFT are correlated negatively), a number of peak height and velocity time integral readouts were also found to be dependent on HR. More specifically, the maximum peak of ventricular inflow (HR-A peak) is correlated positively with HR, while the velocity time integral of the early wave is correlated negatively

with HR (HR-E VTI). The relations of all PWD parameters with HR are displayed in detail in Figure 5.12.

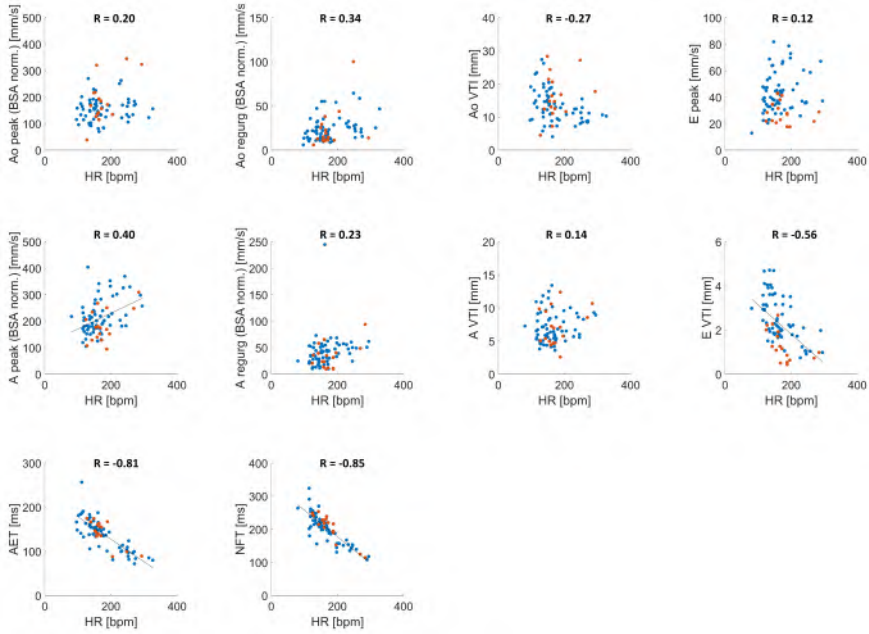

Figure 5.12: Distribution plots (N = 80 samples) of analyzed adults zebrafish pulsed wave Doppler (PWD) parameters all plotted versus heart rate (HR). Pearson correlation coefficients (R) are displayed for all correlations while the trendline is only shown for significant correlations. The presented correlations were analyzed as part of a larger correlation analysis (Figure 8) thus the significance threshold was based on the number of tests of the larger correlation analysis (leading to $\alpha_{adj} = 0.00076$ which corresponds to R > 0.369 or R < - 0.369). Ao: aortic wave (ventricular outflow), A: atrial wave (ventricular inflow), E: early wave (ventricular inflow), VTI: velocity time integral, regurg: regurgitation, AET: aortic ejection time, NFT: no flow time, HR: heart rate. Color legend - blue: male samples, red: female samples.

A numerical overview of all R-coefficients and p-values values resulting from the Pearson correlation analysis of this section is provided in Figure 5.13.

	Age	**Ao peak	Ao VTI	**Ao regurg	AET	**A peak	A VTI	E peak	E VTI	**A regurg	NFT	HR
Age		0.85	0.85	0.06	0.01	2e-4	1e-8	0.23	0.87	1e-3	0.01	6e-4
****Ao peak**	0.02		8e-11	0.04	0.31	0.01	0.03	0.85	0.98	0.44	0.21	0.07
Ao VTI	-0.02	0.65		0.10	4e-4	0.94	7e-4	0.49	0.17	0.78	1e-3	0.02
****Ao regurg**	0.21	0.23	0.19		0.01	0.04	0.46	0.63	0.16	0.18	4e-4	2e-3
AET	-0.29	-0.12	0.39	-0.31		2e-3	0.75	0.44	0.10	0.13	5e-28	1e-19
****A peak**	0.41	0.30	0.01	0.23	-0.34		6e-13	0.01	0.47	1e-4	2e-4	2e-4
A VTI	0.59	0.24	0.37	0.08	0.04	0.70		0.16	0.43	7e-6	0.99	0.23
E peak	0.13	-0.02	-0.08	-0.05	-0.09	0.30	0.16		4e-7	0.94	0.30	0.29
E VTI	0.02	-0.00	0.16	-0.16	0.19	0.08	0.09	0.53		0.42	0.01	9e-8
****A regurg**	0.36	0.09	-0.03	0.15	-0.17	0.42	0.48	0.01	-0.09		0.04	0.04
NFT	-0.28	-0.14	0.36	-0.39	0.89	-0.41	-0.00	-0.11	0.30	-0.23		4e-23
HR	0.37	0.20	-0.27	0.34	-0.81	0.40	0.14	0.12	-0.56	0.23	-0.85	

Figure 5.13: Overview of correlations between automatically analyzed pulsed wave Doppler parameters as well as age of the zebrafish (N = 80). Variables preceded by two asterisks (**) were normalized with respect to body surface area before the correlation analysis. Values below the main diagonal represent the Pearson correlation coefficients (R) while values above the main diagonal represent the corresponding p-values. A significance threshold $\alpha_{adj} = 0.00076$ was used after correcting for multiple testing ($N_{tests} = 66$), corresponding to R > 0.369 or R < - 0.369 as the limit values for significant correlations (positive: lighter yellow, negative: lighter magenta). Arbitrary correlation limits R = ± 0.5 were used to visualize the strongest correlations (positive: yellow, negative: magenta). Ao: aortic wave (ventricular outflow), A: atrial wave (ventricular inflow), E: early wave (ventricular inflow), VTI: velocity time integral, regurg: regurgitation, AET: aortic ejection time, NFT: no flow time, HR: heart rate.

5.3.6 Male-female differences

To evaluate the impact of sex on the PWD parameters, we compared the per sample averaged results for each parameter between male and female samples. We found that two parameters showed a significant male-female difference: both the E peak and E VTI were significantly lower in recordings from female zebrafish (Figure 5.14).

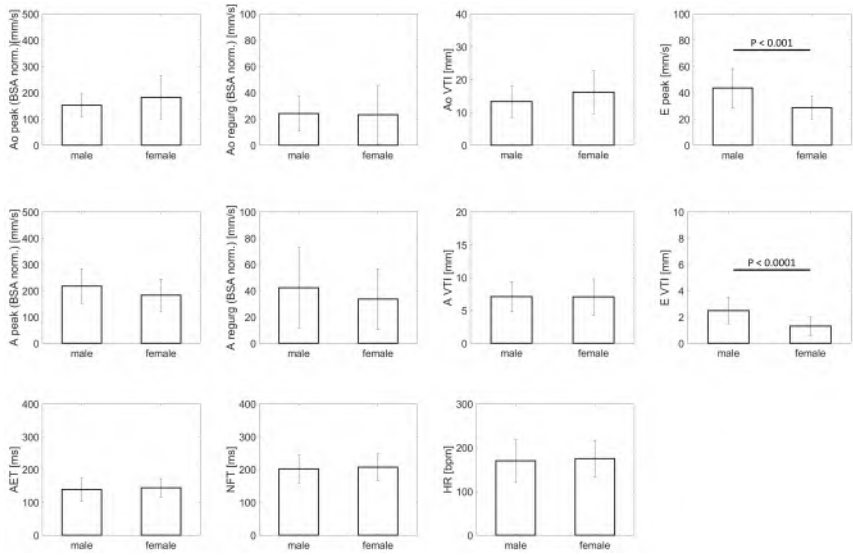

Figure 5.14: Overview of the mean and standard deviation of the automatically analyzed PWD parameters, calculated and grouped separately for male and female animals. P-values are displayed for significant differences between male and female samples resulting from two-sample t-tests. A significance threshold $\alpha_{adj} = 0.0045$ was used after correcting for multiple testing $N_{tests} = 11$). Error bars indicate plus or minus one standard deviation. Ao: aortic wave (ventricular outflow), A: atrial wave (ventricular inflow), E: early wave (ventricular inflow), VTI: velocity time integral, regurg: regurgitation, AET: aortic ejection time, NFT: no flow time, HR: heart rate.

5.4 Discussion

We have developed a fully automated framework to analyze pulsed wave Doppler measurements of ventricular in- and outflow in adult zebrafish and used this to perform unprecedented in-depth analyses of different PW Doppler parameters for a large number of zebrafish.

From a technical perspective, we applied standard gray-value and gradient-based methods to the DICOM images of zebrafish PWD measurements to detect contours of traces, and developed logical rules to extract fiducial points and define timestamps. In our hands, the used code works excellently and it is available to the community. Alternatively, approaches based on artificial neural networks could work equally well provided appropriate training of the chosen network on a sufficiently large database. In fact, by using our fully automated pipeline, a large number automatically extracted contours and points of interest can be generated and used as input data for training and

validation of neural networks. To support this, we have made the automated annotations of our complete dataset openly available at Zenodo Zenodo.

The combination of regression plots (Figure 5.4), Bland-Altman plots (Figure 5.5) and the qualitative (visual) validation of all automated annotations demonstrate a very good agreement between the manually and automatically obtained PWD parameter values. The best agreement was found for the Ao peak, Ao VTI, A peak and A VTI parameters (R-squared between 0.95 and 0.97). A very high agreement was also found for the Ao regurg, A regurg and E peak parameters (R-squared between 0.90 and 0.95) and the slight decrease in agreement can be explained by the fact that the regurgitation and E peaks are typically much lower than the A and Ao peaks, resulting in a slightly larger effect of errors related to the pixel accuracy of both manual and automated annotations. A good agreement was also found for NFT parameter (R-squared of 0.85). AV flow based AET is the only analyzed PWD parameter for which the accuracy of the automated annotations was deemed insufficient, mainly caused by the noisy or barely visible and not clearly bounded signal parts of the AET on the inflow recording for some samples (Figure 5.6).

Regarding all quantitatively validated parameters, it is also worth mentioning that not all differences between the automated and manual annotations necessarily correspond to an error in the automated annotation. In some cases, the signal quality only allows a - to some extent - uncertain manual annotation. Moreover, even if the signal quality was good and the annotations were performed by an experienced operator, a trade-off always exists between the accuracy of the manual annotation and time available for the hands-on analysis.

The order of and the time in between the inflow and outflow measurement of the same sample turned out to have an effect on the heart rate values. To minimize confounded results due to anesthesia effects on cardiovascular performance [163, 182, 183], it thus does not suffice to perform all ultrasound measurements within a certain time window (usually below 3-5 minutes) but a fixed order of measurements, part of a fully standardized protocol is needed. While this may seem a fairly trivial recommendation, the order between the inflow and outflow signal is sometimes changed depending on which signal is detected first to limit the per sample anesthesia time of the total experiment. In our dataset, we found a significant difference

between inflow and outflow based HR (even though measurements were only taken approximately 1 minute apart). In general, we suggest to use the outflow based heart rate when comparing with other AoV (out)flow PWD parameters, to use the inflow based heart rate when comparing with other AV (in)flow PWD parameters and to use the average of both when analyzing the effect of biological variables such as age, sex and body surface area.

Aortic ejection time and no flow time can be combined to calculate the myocardial performance index and both time intervals are usually indicated on the inflow recording [113, 183]. We found that AoV (out)flow based AET can be used instead of AV (in)flow based AET, which is considerably easier to annotate (both manually and automatically) due to the sometimes noisy and only partially visible AET signal part on the inflow recording.

We found that the Ao peak, Ao regurg, A peak and A regurg all showed a significant (positive) correlation with BSA. We recommend to normalize these parameters with respect to BSA for further analyses. Interestingly, BSA significantly influences peak heights (although not the height of the E peak) but not the velocity time integrals of the aortic wave or atrial wave. A positive (not significant) trend is still observed between BSA and Ao VTI or A VTI but this relation is less strong than the correlations between BSA and Ao peak or A peak because a negative (not significant) trend is observed between BSA and the opening time of the aortic or atrioventricular valve.

Also remarkably, our results suggest a (strong) significant negative correlation between heart rate and E VTI but no correlation between heart rate and E peak (maximum height) was observed. On the other hand, a positive correlation between heart rate and A peak (maximum height) was found but no correlation between heart rate and A VTI was present. The E wave corresponds to passive ventricular inflow during the first opening of the AV valve and the A wave represents the active filling of the ventricle due to the contraction of the atrium, together determining diastolic function. A higher heart rate thus mainly seems to reduce the ventricular inflow during the early phase in zebrafish which is accompanied by a limited opening time before the atrial contraction. Also the duration of the atrial wave will (generally) be shorter at higher heart rates but the higher peak flow values in this shorter time window result in a preserved velocity time integral of the atrial wave (A VTI). No correlations were observed between E peak and A peak or between E VTI and A VTI.

In agreement with the study of Wang et al. [163], we observed a significant male-female difference for the maximum height of the early wave (E peak), with lower values for female zebrafish. Also for the velocity time integral of the early wave E VTI (not analyzed by Wang et al.), we found significantly lower values, thus representing lower passive ventricular inflow, in female animals. It is important to note that the (ratio of the) E wave and A wave clearly differ(s) between humans and (zebra)fish. In humans but also in other mammals such as mice, the E wave is higher than the A wave while the opposite is true in (zebra)fish. This is likely caused by a much higher preload in mammals compared to fish which explains the difference between passive and active ventricular filling in humans and zebrafish. Despite these differences, our findings can be crucial to evaluate zebrafish models of impaired diastolic function adequately. The found male-female differences in zebrafish agree with the known lower female (compared to male) ventricular compliance in humans [184].

As mentioned, both regurgitation peaks (Ao regurg and A regurg) correlate with body surface area but other correlations show remarkable differences between the aortic wave regurgitation (Ao regurg) and atrial wave regurgitation (A regurg). Also after normalization with respect to BSA, positive correlations between A regurg-A peak and A regurg-A VTI but no correlations between Ao regurg-Ao peak and Ao regurg-Ao VTI were found. Instead, for the aortic outflow regurgitation, a negative correlation Ao regurg-NFT was found while no such correlation between A regurg-NFT was found. These findings can become especially relevant when analyzing the regurgitation in zebrafish models of cardiovascular disease.

The skewed distributions of the different age groups and male-female ratios within these groups of our dataset could be considered as a limiting factor. We have included all wild-type recordings that were made within a 1.5 year timeframe to maximize the sample size of our dataset. Only the recordings of two very heavy (most likely egg-bound) female samples for which the body weights would be outliers in our dataset were excluded. Older recordings (before the 1.5 year timeframe) were also excluded to ensure that measurements were performed by a single operator with sufficient experience. Some variability is to be expected due to different ages of the zebrafish used in this study, but by applying a strict Bonferroni correction for multiple testing and by carefully interpreting the results of the complete dataset, we aim to provide comprehensive yet still adequate findings

and conclusions. The positive age-A peak correlation agrees with the study of Wang et al. (18) but in general, the observed correlations with age (age-A peak, age-A VTI and age-HR) should be confirmed in experiments specifically designed for this purpose. In general we suggest a study with fully balanced age and gender groups using the automated analysis framework provided in this manuscript as a very relevant future work study. Investigating the effect of the gravid conditions on different parameters could also be included.

5.5 Conclusion

To summarize, we have developed a fully automated framework to analyze pulsed wave Doppler measurements of ventricular in- and outflow in adult zebrafish. All cardiac cycles within a recording can be processed without any operator-dependent inputs. Our algorithms were validated by comparing the automated results with manual annotations performed by an experienced operator and a high level of agreement was found. An extensive reference dataset for different pulsed wave Doppler based parameters in wild-type adult zebrafish is provided. We highlight generally applicable aspects such as normalization with respect to body surface area and report correlations between different PWD parameter values as well as male-female differences in wild-type zebrafish. This framework can be used for advanced, fast and unbiased phenotyping of zebrafish models of cardiovascular disease, a promising and increasingly popular animal model for (human) genetic cardiovascular diseases. Future results can be compared with the wild-type reference data provided in this manuscript.

CHAPTER 6

Cardiovascular CT-imaging and 3D reconstruction in adult zebrafish

6.1 Introduction

Of all the available imaging techniques discussed in Chapter 4, synchrotron CT-imaging was selected as the most promising technique to obtain accurate anatomical and structural three-dimensional cardiovascular information of the adult zebrafish, both for direct morphological phenotyping and as starting point for numerical simulations. Although no reports with a dedicated focus on the adult zebrafish cardiovascular structures are available, CT-imaging seems (one of the few techniques) able to provide accurate three-dimensional cardiovascular information in the adult zebrafish, especially beyond the ventricle. To be able to distinguish the blood spaces and soft tissues and to obtain as much details as possible of the (soft) tissue structures, synchrotron phase-contrast CT-imaging will be used.

This chapter thus mainly investigates the use of synchrotron CT-imaging to view and 3D reconstruct the cardiovascular system in adult zebrafish. This research is structured into Methods 6.2, Results 6.3, Discussion 6.4, Conclusion 6.5 and Application 6.6 sections. Finally, in section 6.7, both CT-imaging and synchrotron CT-imaging in combination with casting of the zebrafish vasculature are discussed.

6.2 Methods

6.2.1 Specimen preparation for synchrotron imaging

Tricaine in lethal dose (1 $g\,L^{-1}$) was used to euthanize the fish. The samples were first fixed in modified Davidson's Fixative overnight and subsequently fixed in 4 % paraformaldehyde. Some samples were decalcified in citric acid. All samples were then stored in 70 % ethanol (EtOH). On the day of transport, samples were rehydrated by subsequent changes to 50 % EtOH, 25 % EtOH and finally phosphate-buffered saline (PBS). As the main cardiovascular structures of interest, being the ventricle, bulbus arteriosus and ventral aorta in this case, are located near the zebrafish head, only the most cranial part of the zebrafish was kept for most samples. A full body scan was taken for two samples. Shortly before the scan, samples were immobilized in 1.5 mL Eppendorf tubes filled with agarose gel. All samples were oriented vertically in the Eppendorf tubes, heads pointing upwards.

6.2.2 Sample overview

The presented results and discussions on synchrotron microCT imaging of non casted zebrafish are based on a sample size of 19 zebrafish. An overview is presented in Table 6.1. Also when referring to specific samples in 7 and Chapter 8, the sample numbering provided in Table 6.1 will be used.

Additionally, more (non casted) samples (including zebrafish with fbn2b and/or ltbp1 mutations) were scanned and pre-processed for segmentation by this PhD thesis author but the actual segmentation and analysis of these samples was performed by other PhD students and master students. Also casted samples were scanned using synchrotron microCT imaging (reported in Section 6.7).

Table 6.1: Overview of included zebrafish samples scanned with synchrotron microCT imaging.

Sample number	Wild-type	Decalcification
#1	Yes	Yes
#2	Yes	Yes
#3	Yes	Yes
#4	Yes	Yes
#5	Yes	Yes
#6	Yes	Yes
#7	No (fbn1-/-)	Yes
#8	No (fbn1-/-)	Yes
#9	No (fbn1-/-)	Yes
#10	No (fbn1-/-)	Yes
#11	No (fbn1-/-)	Yes
#12	Yes	No
#13	Yes	No
#14	Yes	No
#15	Yes	No
#16	Yes	No
#17	Yes	Yes
#18	Yes	Yes
#19	Yes	Yes

6.2.3 Synchrotron phase-contrast imaging

Propagation-based phase-contrast synchrotron X-ray imaging was performed at the Paul Scherrer Institute in Villigen (Switzerland), using the synchrotron Swiss Light Source. More specifically, all experiments were performed at the TOmographic Microscopy and Coherent rAdiology experimentTs (TOMCAT) beamline. In Figure 6.1 panel a, the scan room setting is depicted. Initially, the Eppendorf tubes were fixed onto the robot sample holder using wax (Figure 6.1 panel b). Later on, to ensure faster and more reliable mounting of the samples, custom-made 3D printed holders suitable for the Eppendorf tubes were foreseen (Figure 6.1 panel a and c).

Initially, inspired by the scanning of mouse aorta samples at the same beamline [185], the zebrafish samples were scanned at a monochromatic beam energy of 21.8 keV and object-detector distance of 250 mm. Different monochromatic beam energies (13 keV, 16 keV and 21.8 keV, 30 keV) and object-detector distances (50 mm, 100 mm and 250 mm) are also compared. In all experiments, the same LUAg:CE

20 µm scintillator and PCO.Edge 5.5 detector were used. Two different microscope objectives (UPLAPO 4x and UPLAPO 10x) are compared.

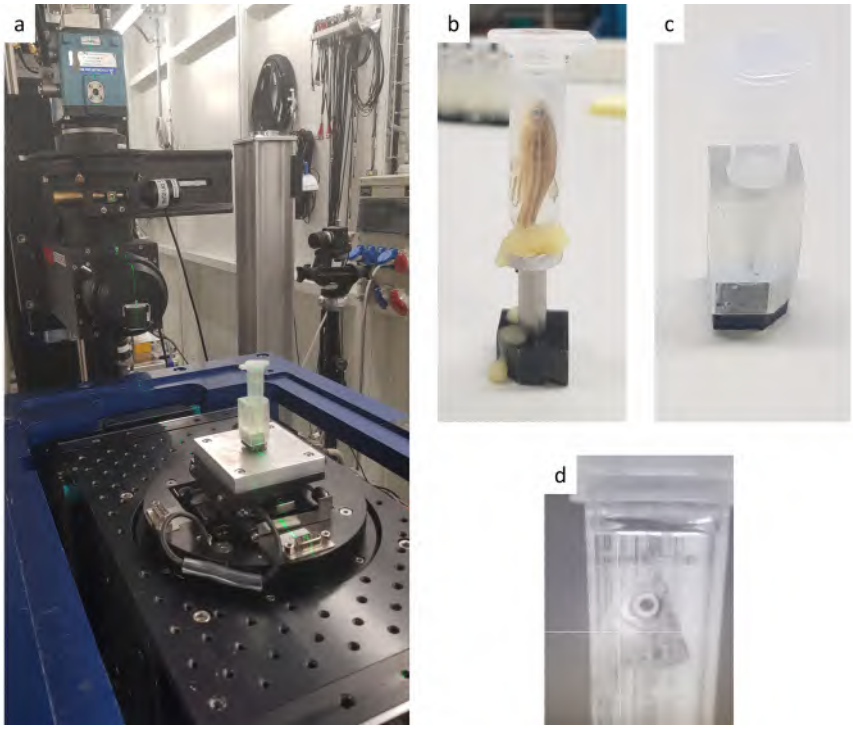

Figure 6.1: (a) View of the synchrotron scan room while a sample is mounted for scanning. (b) A full body sample showing the use of wax to fix the Eppendorf tube. (c) A custom-made 3D printed holder suitable for the used Eppendorf tubes. (d) The depicted cranial part of the zebrafish includes the complete ventricle, bulbus arteriosus and ventral aorta. The white cross indicates the center of the field-of-view (in one of the two planes) aiming to center the bulbus arteriosus in this scan.

The tomographic reconstruction into image stacks was performed onsite using the post-processing pipeline for tomgographic reconstruction at TOMCAT [186]. In this pipeline, the Gridrec reconstruction algorithm [187] is used to reconstruct the projections into a stack of images (3D imaging data set). The effect of phase retrieval as proposed by Paganin [188] was evaluated.

In all cases, the used scan modalities resulted in image stacks of 2160 slices (axially) of 2560 x 2560 pixels (in plane). The 4x magnification

corresponds to an isotropic voxel size of 1.625 µm^3 and a field-of-view of 4.16 x 4.16 mm^2 (in plane) x 3.51 mm (axial). For the 10x magnification, these numbers scale linearly to an isotropic voxel size of 0.65 µm^3 and a field-of-view of 1.66 x 1.66 µm^2 (in plane) x 1.4 mm (axial). Stitching of image stacks (also called image blocks) to expand the field-of-view without having to reduce the resolution, is possible.

6.2.4 Segmentation and 3D reconstruction

The segmentation and 3D reconstruction were performed using the medical image processing software package Mimics (Materialise, Leuven, Belgium). In this chapter, the tissue structures are not differentiated from the blood spaces, but this differentiation will be described in the next chapter. For decalcified samples, first, a threshold interval was visually defined to include the cardiovascular structures of interest. This also (unavoidably for the obtained datasets) results in inclusion of neighboring structures (tissues) in the mask and a region grow operation could not isolate the structures of interest. Therefore, connections in the mask between the structures of interest and neighboring tissues were manually removed on a limited number of slices and the built-in 'multiple slice edit' and 'interpolation' tools were then used to detach the structures of interest completely. A mask of the structure of interest could then be obtained by the region grow operation. Holes in this mask were automatically filled by using the 'smart fill' tool before generating the 3D volume. For non decalcified samples, similar steps were followed but more manual operations were needed.

6.3 Results

6.3.1 Key cardiovascular structures in the adult zebrafish

Figure 6.2 and Figure 6.3 visualize several cardiovascular structures in the adult zebrafish for a non decalcified sample (sample #14) scanned at 21.8 keV, 250 mm object-detector distance and 4x magnification. Paganin phase retrieval was used for the image reconstruction. Key cardiovascular structures such as the ventral aorta, bulbus arteriosus, ventricle and atrium can be identified clearly. The high attenuation of bone structures results in the bright (white) appearance of bone structures on the images and also causes high-density artifacts visible as dark, straight lines extending from the bone structures and distorting the image.

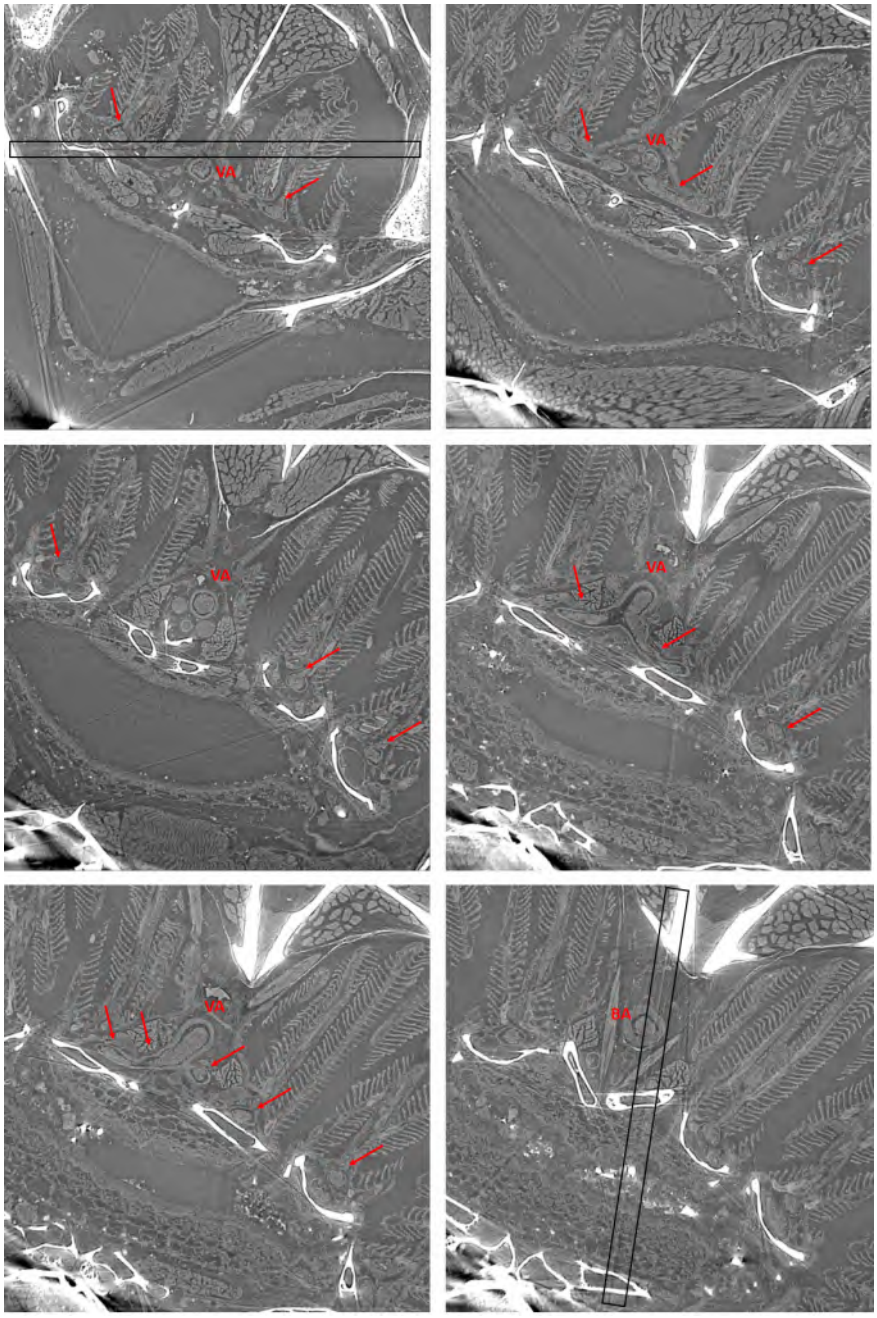

Figure 6.2: Image slices resulting of the synchrotron scan of a non decalcified sample mainly showing the ventral aorta (VA), afferent branchial arteries (red arrows) gill vasculature and part of the bulbus arteriosus (BA) immediately upstream of the ventral aorta. Black rectangles indicate high-density artifacts extending from the bone structures. Sample #14.

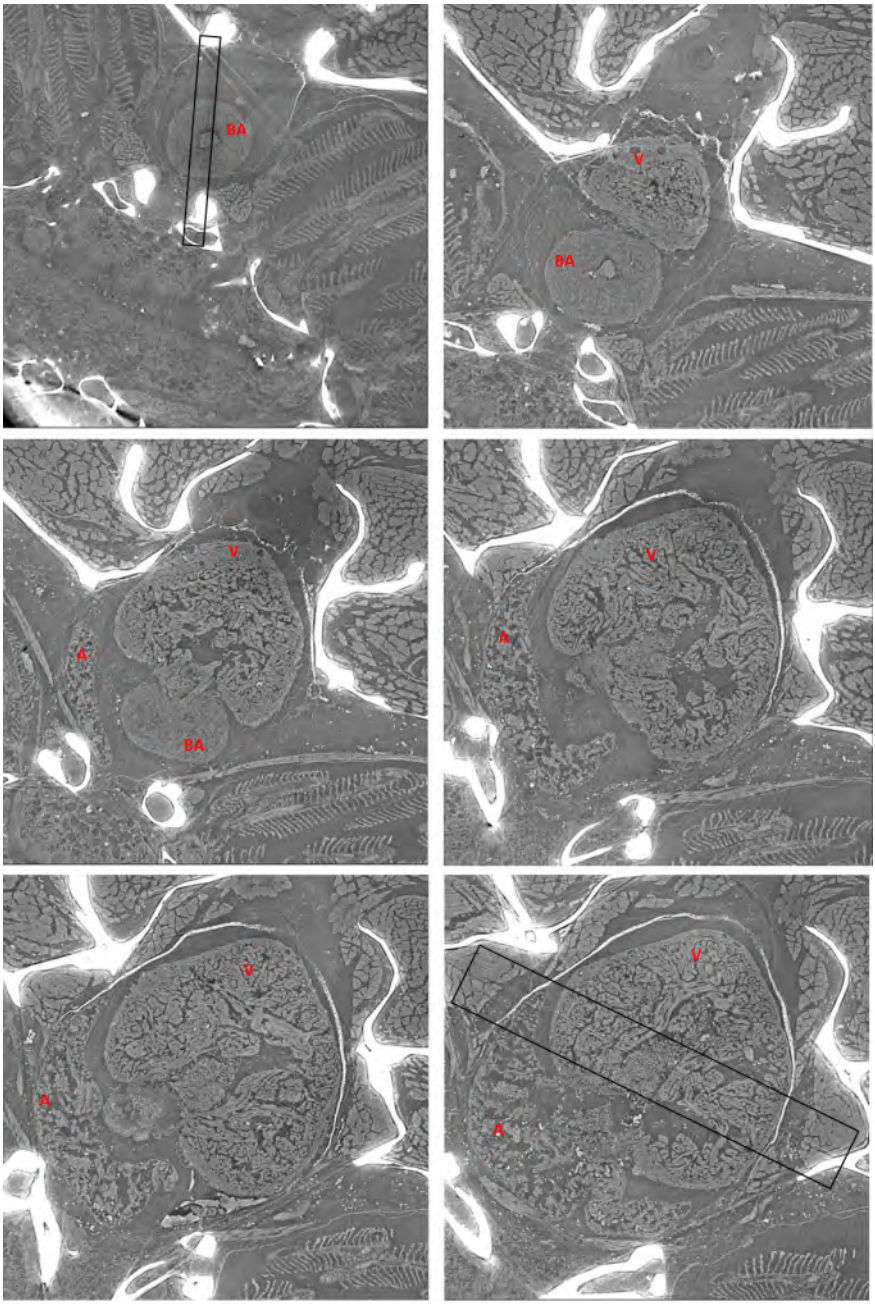

Figure 6.3: Image slices resulting of the synchrotron scan of a non decalcified sample mainly showing the bulbus arteriosus (BA), ventricle (V) and atrium (A). Black rectangles indicate high-density artifacts extending from the bone structures. Sample #14.

6.3.2 Paganin phase retrieval

By visually comparing image stacks reconstructed without and with Paganin phase retrieval, the observation was made that phase retrieval seems to improve the contrast of the images (slices) of resulting images stacks. A representative example is shown in Figure 6.4. This non decalcified sample was scanned at 21.8 keV, 250 mm object-detector distance and 4x magnification.

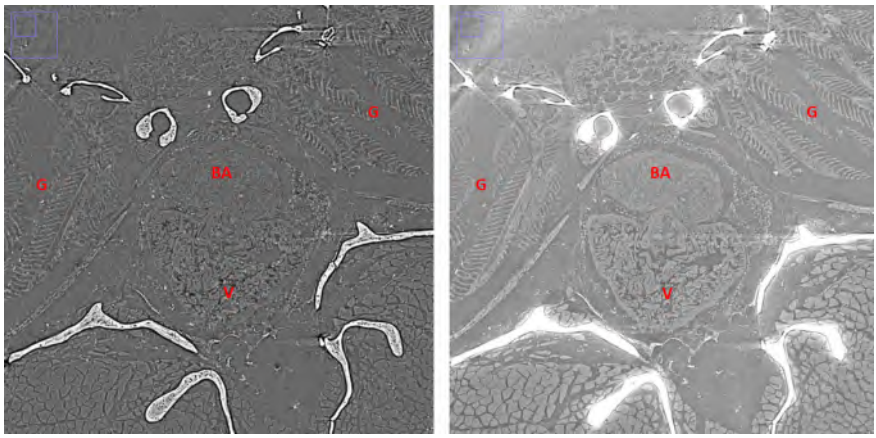

Figure 6.4: Left versus right: Representative images of synchrotron microCT scans reconstructed without (left) and with (right) phase retrieval. Bones appear bright on the images. G: gills, V: ventricle, BA: bulbus arteriosus. Sample #13.

In Figure 6.5, zoomed in views of the bulbus arteriosus of the same sample are shown in all four image panels. The perceived effect of Paganin phase retrieval is now also quantified via the display ranges and pixel gray value distribution provided in the top right corner of each image panel. In the top image panels, the display ranges covers the complete range between the minimal and maximal pixel intensity (gray value) of the data (16 bit image stack). The diagonal line indicates that the image panels are shown according to the complete display range but the narrow histograms peaks indicate that the vast majority of pixels can be captured in a narrowed display range. The display range was altered accordingly in the bottom images (see diagonal lines as well as minimum and maximum values in the bottom images). The greater width of the visible peak in the histogram demonstrates quantitatively that reconstructing images with Paganin phase retrieval improves contrast.

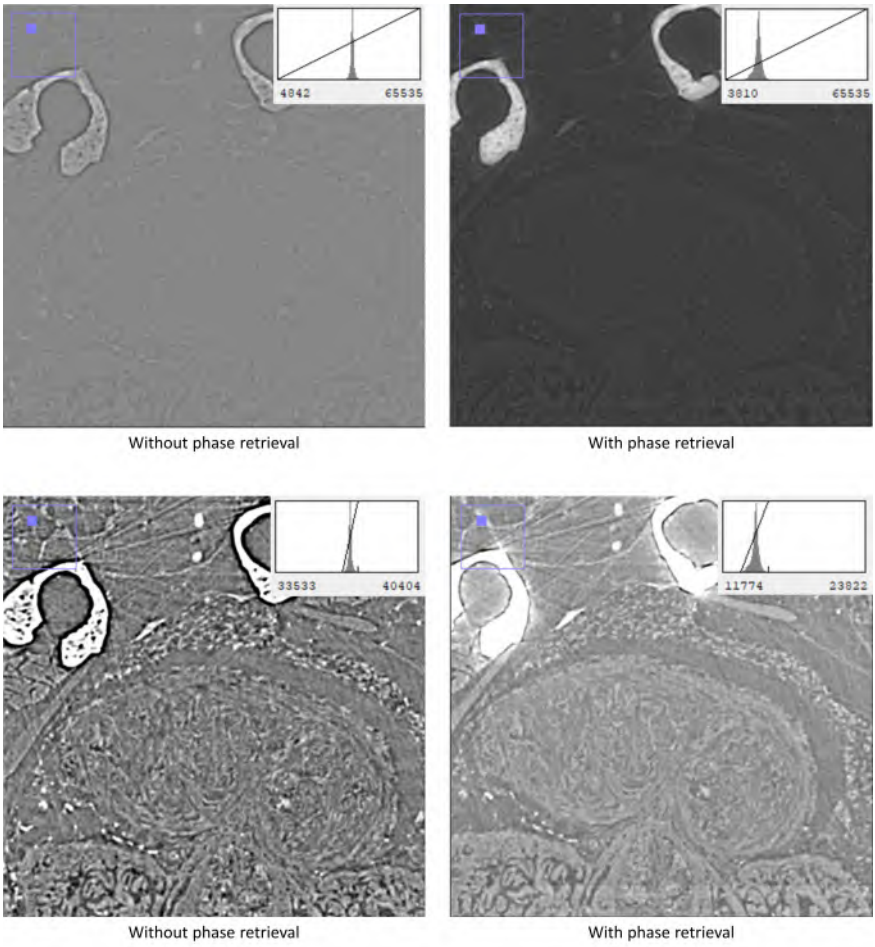

Figure 6.5: Left versus right: propagation-based phase-contrast images reconstructed without (left) and with (right) phase retrieval. Both on the left and right side, the top and bottom images contain the same information but the display ranges, included in the top right corner of each image, differ. Two bone structures are visible in these images, the bulbus arteriosus is visible and also (part of) the bulboventricular valve and ventricle can be seen at the bottom of the images. Sample #13.

6.3.3 Decalcification

The effect of decalcification of the sample prior to scanning is illustrated in Figure 6.6. This decalcified sample was scanned at 21.8 keV, 250 mm object-detector distance and 4x magnification. Paganin phase retrieval was used during the image reconstruction. Bone structures no longer cause high-density artifacts resulting in an improvement of the image quality in soft tissue regions. An animation showing many more 2D slices of this sample, focusing on the gill

vasculature, ventral aorta, bulbus arteriosus, ventricle and atrium is provided online.

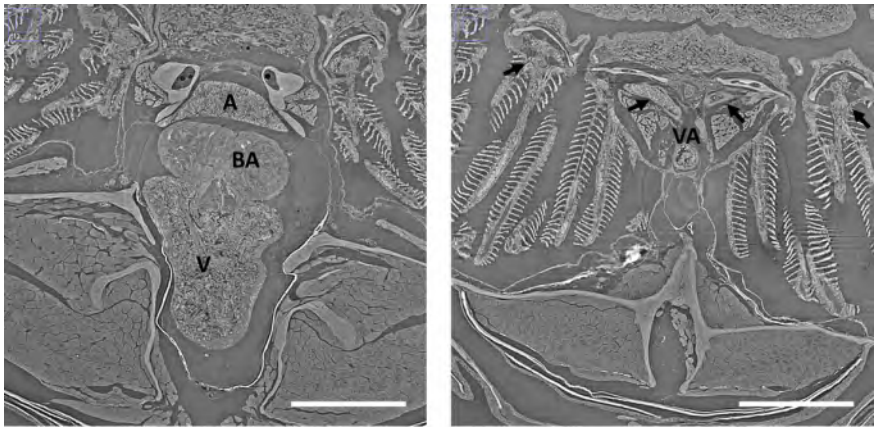

Figure 6.6: Scanning of a decalcified sample showing the atrium (A), ventricle (V), bulbus arteriosus (BA), ventral aorta (VA) and afferent branchial arteries (black arrows). Scale bars: 500 µm. Sample #17.

6.3.4 Optimizing beam energy and object-detector distance

Beam energy and object-detector distance (also called sample-detector distance can be adjusted at the TOMCAT beamline. To determine a suitable combination of beam energy and object-detector distance for scanning of the major cardiovascular structures in adult zebrafish, different combinations were compared. Figure 6.7 depicts the effect of varying beam energy at constant object-detector distance while Figure 6.8 depicts the effect of varying object-detector distance at constant beam energy.

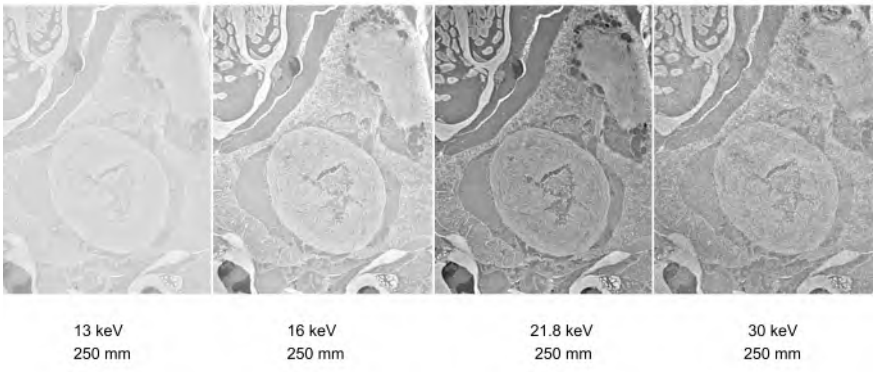

Figure 6.7: Synchrotron images of the bulbus arteriosus of the same sample, each time scanned at the same object-detector distance (250 mm) but at different beam energies (13 keV, 16 keV, 21,8 keV, 30 keV). Scanned at 4x magnification and reconstructed with Paganin phase retrieval. Sample #18.

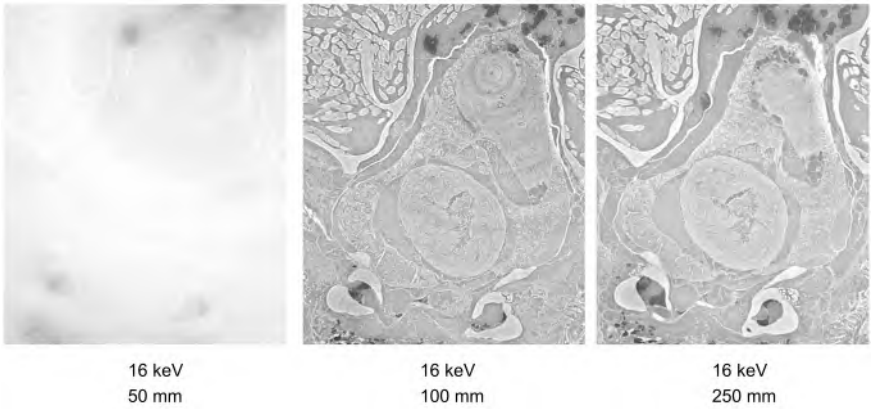

Figure 6.8: Synchrotron images of the bulbus arteriosus of the same sample, each time scanned at the same beam energy (16 keV) but at different object-detector distances (50mm, 100mm, 250 mm). Scanned at 4x magnification and reconstructed with Paganin phase retrieval. Sample #18.

Two extra combinations, 13 keV - 50 mm and 21.8 keV - 100 mm are depicted in the middle image panels in Figure 6.9 and Figure 6.10, respectively. In both figures, the left and right image panels are shown for comparison and correspond to panels also shown in Figure 6.7 or Figure 6.8.

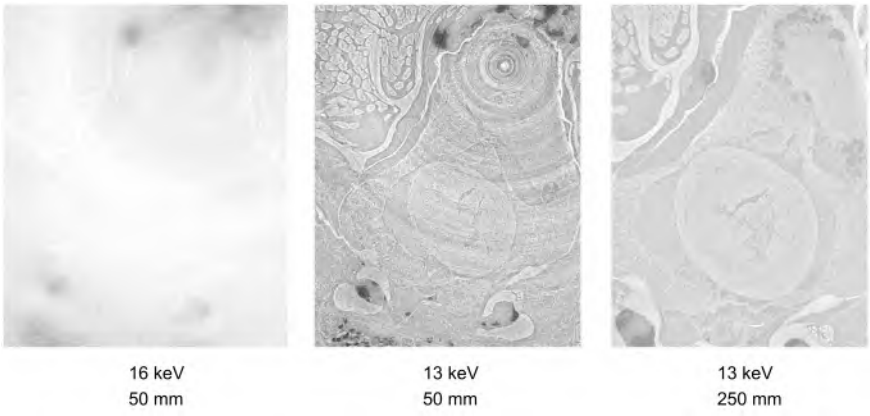

Figure 6.9: Synchrotron images of the bulbus arteriosus of the same sample scanned at 4x magnification and reconstructed with Paganin phase retrieval. Sample #18.

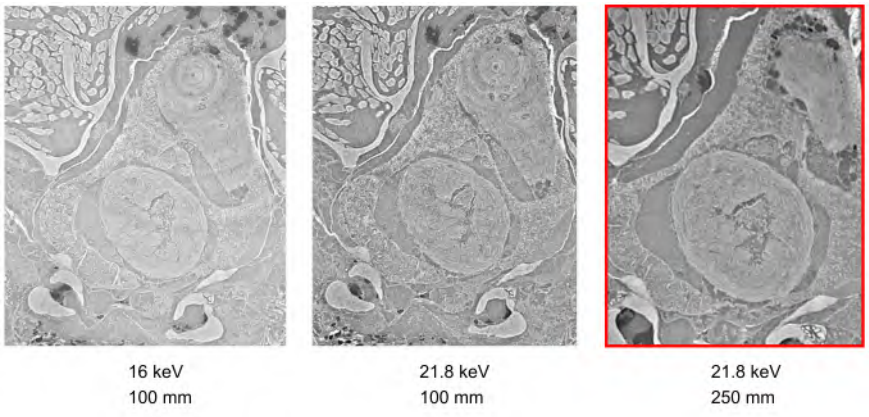

Figure 6.10: Synchrotron images of the bulbus arteriosus of the same sample scanned at 4x magnification and reconstructed with Paganin phase retrieval. The combination of 21.8 keV and object-detector distance of 250 mm was selected as the best option (as highlighted in the red frame). Sample #18.

Of the beam energy - object detector distance combinations presented in Figure 6.7, Figure 6.8, Figure 6.9 and Figure 6.10, the combination 21.8 keV - 250 mm was selected (based on visual inspection) as the best suited option for imaging of major cardiovascular structures (e.g., the bulbus arteriosus).

6.3.5 Different microscope objectives (magnifications)

Two different microscope objectives (4x versus 10x magnification) and corresponding voxel sizes (1.625 μm^3 versus 0.65 μm^3) are compared

in Figure 6.11. A 4x scan (decalcified, 21.8 keV beam energy, 250 mm object-detector distance, image reconstruction with Paganin phase retrieval) is shown on the left and a 10x scan of the same sample (decalcified, 21.8 keV beam energy, 30 mm object-detector distance, image reconstruction with Paganin phase retrieval) is shown on the right. The top image panels depict the complete field-of-view and red boxes indicate the region of a zoomed in view shown in the image panel below. As expected, the resolution of the 10x scan is higher (visibly most clear by comparing the bottom image panels). On the other hand, 3D reconstructions of the major cardiovascular structures were not faster based on 10x image stacks.

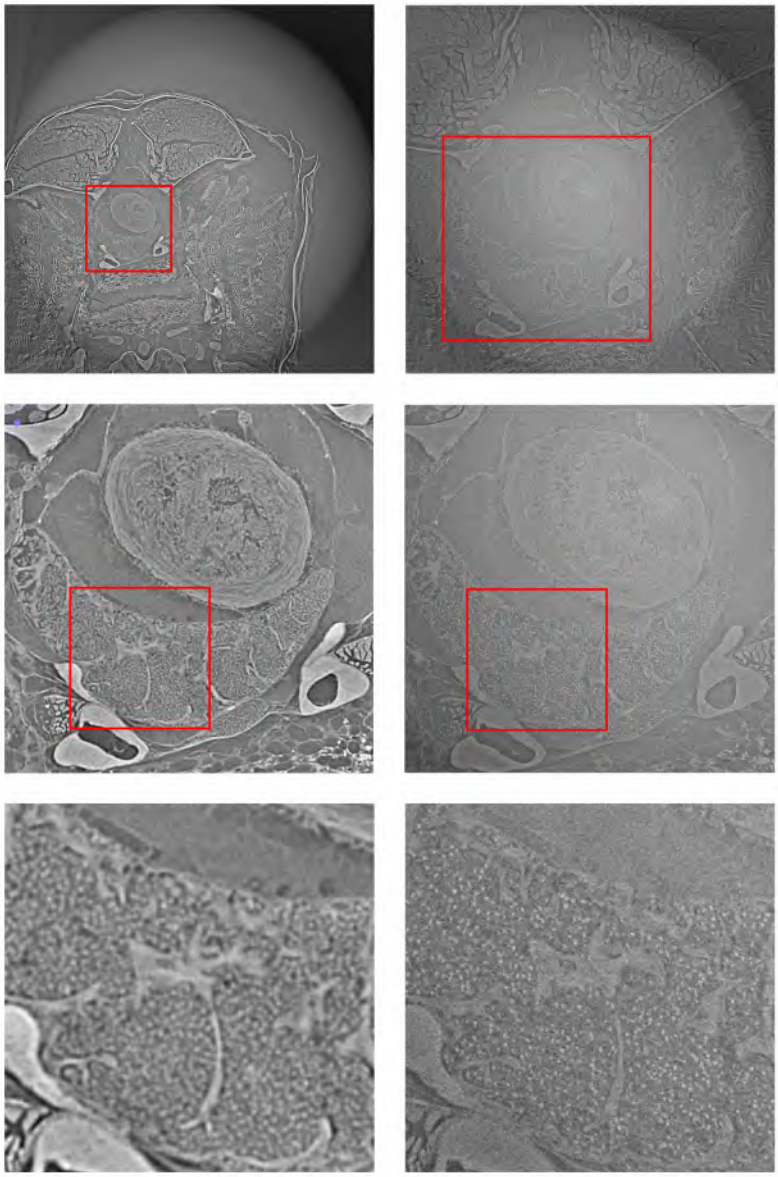

Figure 6.11: Left versus right: comparison based on synchrotron scans using a 4x (left) versus 10x (right) objective. At the top, a complete 4x (left) and 10x (right) image slice of the same sample are shown. In the middle and bottom panels, zoomed in views of the top panel image are shown. A red box correspond to the zoomed in view shown in the panel below. Sample #2.

6.3.6 Segmentation and 3D reconstruction of major cardiovascular structures in adult zebrafish

After decalcification of the sample prior to scanning, synchrotron scanning at 21.8 keV, 250 mm object-detector distance, 4x magni-

fication and using Paganin phase retrieval during the image reconstruction, high-quality image stacks covering the complete bulbus arteriosus and ventral aorta could be obtained in a single scan. Major cardiovascular structures such as the ventral aorta, bulbus arteriosus, ventricle and atrium could be segmented and 3D reconstructed semi-automatically. A representative example illustrating the segmentation of the bulbus arteriosus and ventral aorta is shown in Figure 6.12, Figure 6.13 and Figure 6.14.

In Figure 6.12 the top slices are screenshots after importing the reconstructed images in the segmentation software. The bottom slices show the mask after thresholding. The structures of interest, in this case the bulbus arteriosus (left image panel) and ventral aorta (right image panel) are included in the mask but also (many) other structures have similar intensities and are included in the mask.

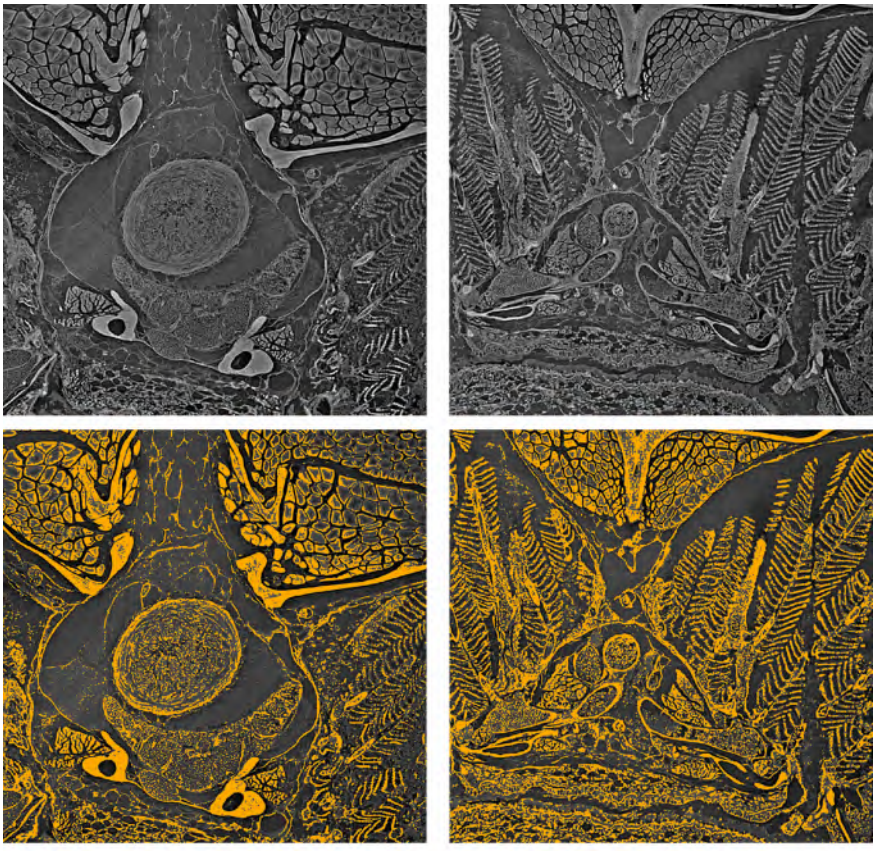

Figure 6.12: Segmentation (thresholding) of a decalcified sample scanned at 21.8 keV and 250 mm object-detector distance. Paganin phase retrieval was performed during the image reconstruction. Sample #2.

The structures of interest in the mask were detached manually from other structures included in the mask (top image panels in Figure 6.13). A region growing operation was used to obtain a mask only including the structures of interest (bottom image panels in Figure 6.13).

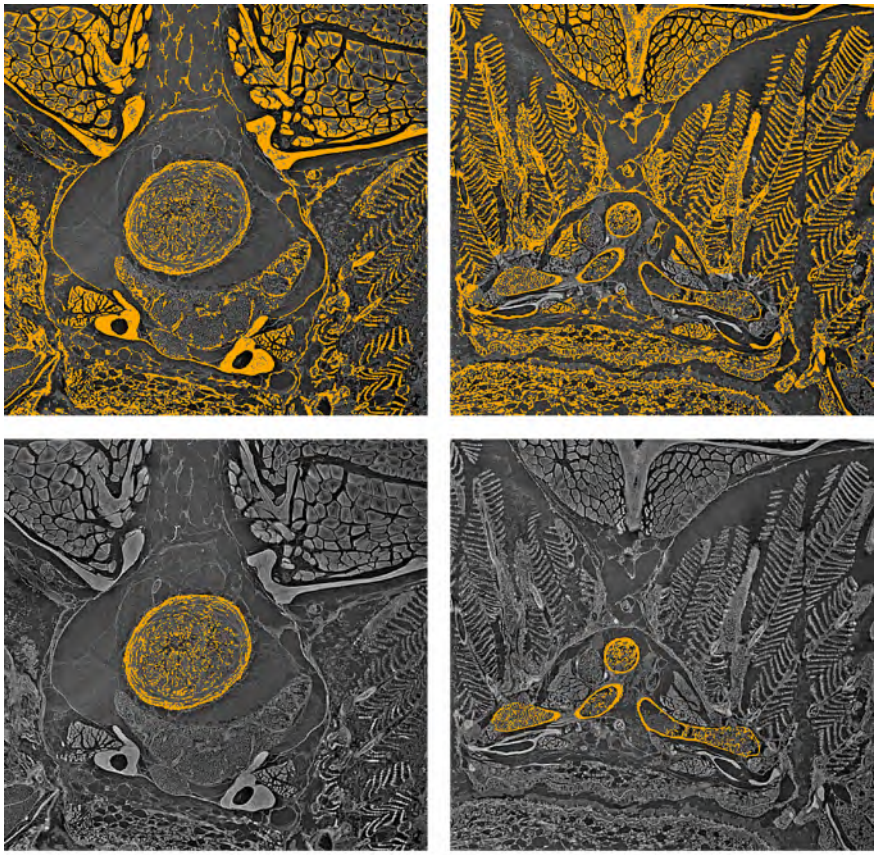

Figure 6.13: Segmentation (detaching from neighboring structures and region growing) of a decalcified sample scanned at 21.8 keV and 250 mm object-detector distance. Paganin phase retrieval was performed during the image reconstruction. Sample #2.

A smart fill operation was used fill the mask (top image panels in Figure 6.14). The mask of the bulbus and ventral aorta is shown in another image plane in the bottom image panels in Figure 6.14, both before (left) and after (right) the smart fill operation. Using different image planes during the segmentation can be helpful to obtain accurate segmentations (e.g., including or removing a cardiac valve in the mask).

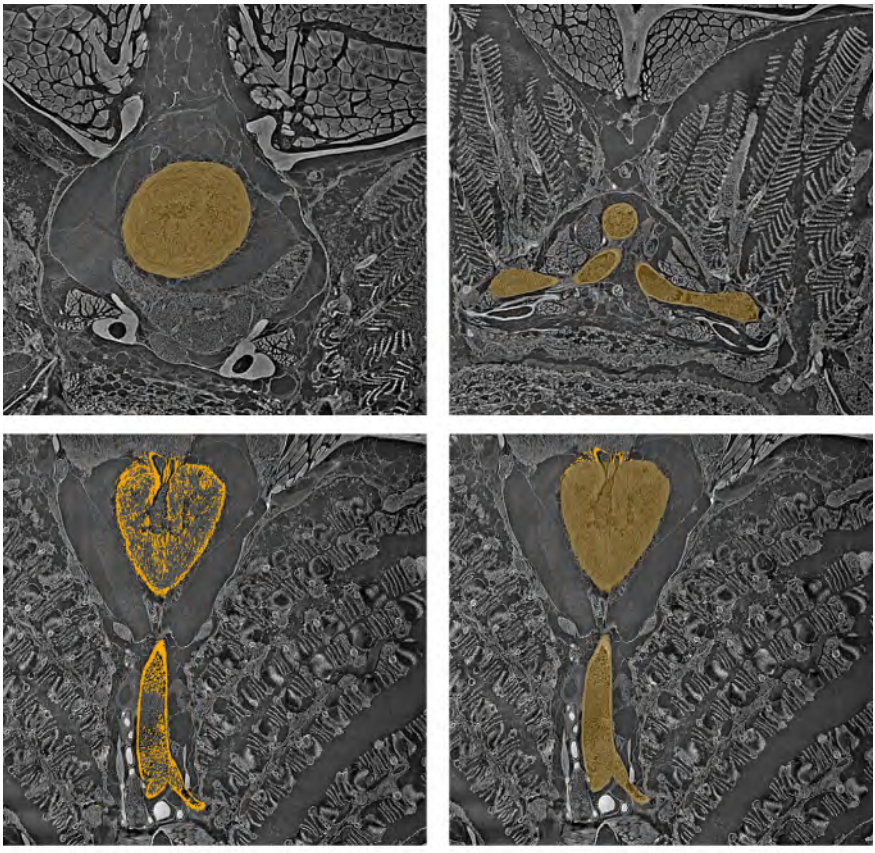

Figure 6.14: Segmentation (smart fill) of a decalcified sample scanned at 21.8 keV and 250 mm object-detector distance. Paganin phase retrieval was performed during the image reconstruction. Sample #2.

Figure 6.15 visualizes a 3D reconstruction, resulting from the segmentation reported in Figure 6.12, Figure 6.13 and Figure 6.14. Next to the bulbus arteriosus and the ventral aorta, also the afferent and efferent branchial arteries as well as the dorsal aorta is visualized. Gill vasculature sprouting from the aortic arches was not included in the segmentation or 3D reconstruction.

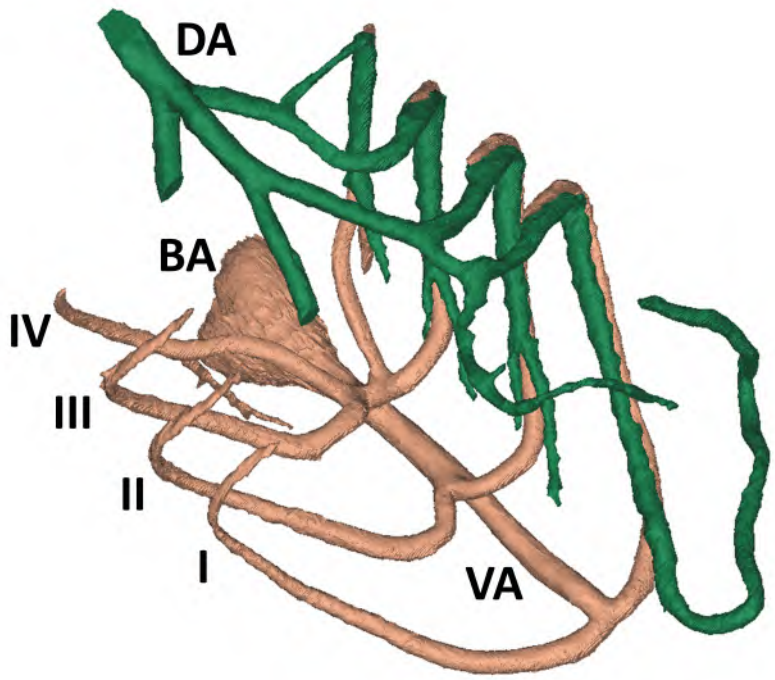

Figure 6.15: 3D reconstruction showing the bulbus arteriosus (BA), ventral aorta (VA) and dorsal aorta (DA). At one side, the efferent branchial arteries were clipped for better overall visualization. Roman numbers I, II, III and IV denote the 1st, 2nd, 3rd and 4th pair of afferent branchial arteries (arches), respectively. The sample was decalcified, scanned at 21.8 keV and 250 mm object-detector distance and Paganin phase retrieval was performed during the image reconstruction. Sample #2.

Also if decalcification is not performed, 3D reconstruction of major cardiovascular structures is possible as illustrated in Figure 6.16. The image quality of non decalcified samples in general necessitates more manual operations which can result in a 'layered' appearance of the 3D reconstruction, clearly showing in which image planes considerable manual operations were performed (Figure 6.16 - top). The bottom image in Figure 6.16 shows the same 3D reconstruction after smoothing.

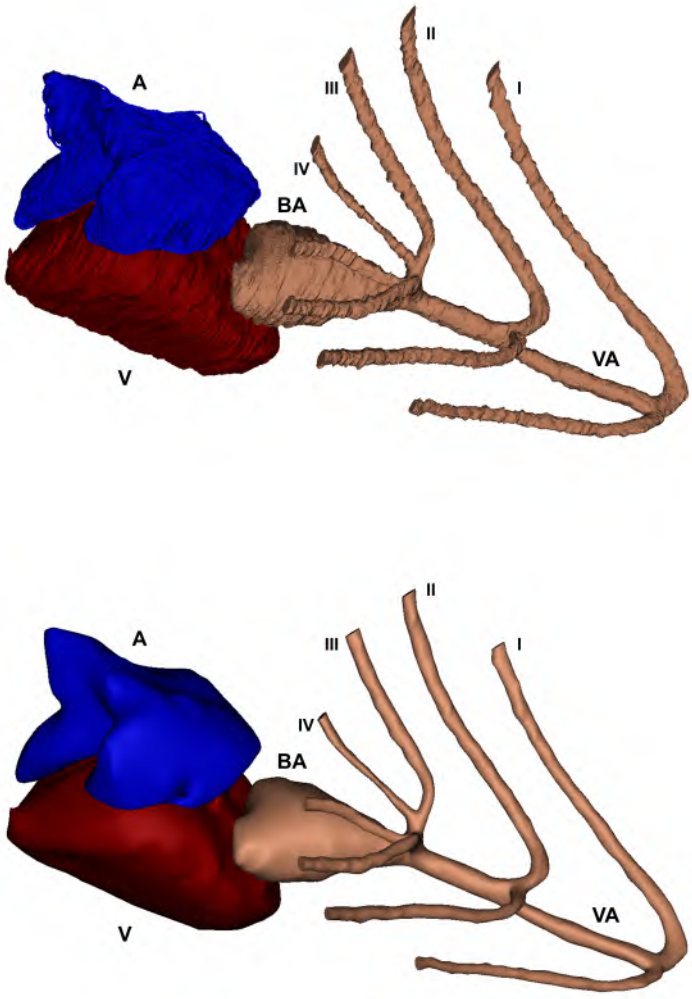

Figure 6.16: 3D reconstruction before (top) and after (bottom) smoothing. Roman numbers I, II, III and IV denote the 1st, 2nd, 3rd and 4th pair of afferent branchial arteries (arches), respectively. BA: bulbus arteriosus, VA: ventral aorta, DA: dorsal aorta. The sample was not decalcified, scanned at 21.8 keV and 250 mm object-detector distance and Paganin phase retrieval was performed during the image reconstruction. Sample #14.

6.4 Discussion

Suitable modalities for synchrotron phase contrast imaging of the major cardiovascular structures in adult zebrafish are: (i) decalcification of the sample prior to scanning, (ii) scanning at 21.8 keV

beam energy, 250 mm object-detector distance and 1.625 µm^3 isotropic voxel size, and (iii) image reconstruction using Paganin phase retrieval. The used scan and image reconstruction modalities agree with earlier experiments on the mouse aorta performed at the same beamline (TOMCAT) of the Paul Scherrer Institute ([185]). The field-of-view needed to capture the mouse aorta (ascending aorta and aortic arch) is similar to the field-of-view needed to capture major adult zebrafish cardiovascular structures. At the TOMCAT beamline, the 4x objective results in a field-of-view of 4.16 x 4.16 mm^2 (in plane) x 3.51 mm (axial) and this allows to capture, e.g., the atrium, ventricle and bulbus arteriosus completely if the zebrafish sample is oriented vertically (Figure 6.1 b and Figure 6.1 d). Within this field-of-view, also the complete ventral aorta could sometimes be captured together with the complete atrium, ventricle and bulbus (e.g., Figure 6.16) but in general capturing all four structures completely in a single scan at 4x magnification was not possible (mainly limited by the axial field-of-view of 3.51 mm). The in-plane field-of-view 4.16 x 4.16 mm^2 is sufficient to capture all four of these structures but note that this field-of-view in general does not include the complete transversal cross section of the zebrafish (e.g., Figure 6.11 top left image panel).

The synchrotron scan modalities agree with the guidelines to select the appropriate synchrotron-based phase contrast technique for pre-clinical cardiovascular imaging as proposed in [189]. In [189], the considered options are (i) propagation-based imaging and image reconstruction without phase retrieval, (ii) propagation-based imaging and image reconstruction with phase retrieval and (iii) grating interferometry imaging. Synchrotron propagation-based phase contrast imaging with (Paganin) phase retrieval is proposed for applications where segmentation of continuous macrostructures (examples in zebrafish being the complete ventricle, bulbus arteriosus or ventral aorta) and the visualization of substructures (examples in zebrafish being the substructures within the bulbar) is desired, which aligns with the aims of our study. Visualization of the substructures within the bulbar wall are desired to allow (future) detection of defects (e.g., microruptures) in zebrafish disease models. At that point, image reconstruction without phase retrieval can be considered to improve resolution and/or to segment these (discrete) defects accurately. The same synchrotron scan (acquisition) can be used, meaning that the sample does not have to be scanned twice in order to obtain an image dataset reconstructed with and without phase retrieval. Note

that in our zebrafish study, we did not analyze the resolution or the contrast-to-noise ratio in detail but the reported visual observations are supported by the data presented in [189].

Scanning at higher magnification improves the resolution but also limits the field-of-view. The complete bulbus arteriosus can be captured within a single scan at 10x magnification, corresponding to an isotropic voxel size of 0.65 μm^3 and field-of-view of 1.66 x 1.66 μm^2 (in plane) x 1.4 mm (axial). A 4x scan was required prior to scanning at 10x, since positioning of the sample for a 10x scan was based on the position and corresponding images at 4x. In synchrotron experiments focusing on the cardiovascular structures of adult zebrafish, one thus has to decided whether or not scans at higher magnification are also desired (resulting in longer duration of the experiment). The acquisition time of a single scan was approximately 7 minutes (time without image reconstruction). Scanning at higher magnification should be considered especially if structural (micro)defects are anticipated.

Segmentation and 3D reconstruction of key cardiovascular macrostructures in adult zebrafish such as the ventricle, bulbus arteriosus and ventral aorta is possible based on the obtained synchrotron image datasets and the segmentation of these structures could be performed largely automatic. Manual operations where however necessary, in particular to detach the structures of interest from surrounding structures in between the 'thresholding' and 'region growing' segmentation steps as explained in Subsection 6.3.6. The slices on which the manual removal of mask regions was performed could be limited by using the 'interpolation tool' available in Mimics. Also other structures such as the ventral aorta, dorsal aorta or branchial arteries can be segmented and 3D reconstruction but considerable manual operations to detach these structures from surrounding or connected (in the case of gill vasculature removal) structure are then needed. Also other structures such as coronary arteries or intersegmental vessels (visible in full body scans) can be 3D reconstructed but considerable manual operations are needed. Note that bone structures can be segmented easily (highly automatic), also after decalcification of the sample prior to scanning.

In this study, agarose embedding was used but a different (plastic) embedding protocol for synchrotron scanning of juvenile zebrafish was reported in [153]. The research groups involved in this PhD study aimed to replicate the (plastic) embedding protocol and a very limited

number of samples was scanned at the TOMCAT beamline using plastic embedding instead of agarose embedding but the image results were (highly) unsatisfactory. Similar to [153], pink beam synchrotron imaging can be considered in future work, which would reduce the acquisition time per sample.

This study reports synchrotron imaging (solely) dedicated to the cardiovascular structures in adult zebrafish. The described methodology can be used both to generate geometry inputs for zebrafish-specific finite element simulations (see also Chapter 7 and Chapter 8) and as tool for three-dimensional morphological phenotyping (see also Section 6.6).

6.5 Conclusion

Synchrotron phase contrast microCT imaging at 21.8 keV beam energy, 250 mm object-detector distance and isotropic voxel size of 1.625 μm^3 can provide accurate 2D information and 3D reconstructions of key cardiovascular structures such as the atrium, ventricle, bulbus arteriosus, ventral aorta and dorsal aorta. Decalcification of the sample prior to imaging and the use of Paganin phase retrieval during the image reconstruction improve image quality and facilitate segmentation of the resulting image stacks. Based on these modalities, major cardiovascular structures such as the ventricle and bulbus arteriosus can be segmented largely automatically and also structures such as the ventral aorta and afferent branchial arteries can be 3D reconstructed after combining several manual and automated operations.

6.6 Application: 3D morphological phenotyping of the bulbus arteriosus

Synchrotron imaging and 3D reconstruction as described above can be used to compare the overall morphology and appearance of bulbus arteriosus in wild-type zebrafish versus mutant zebrafish. In the following preliminary study, 6 wild-type zebrafish (samples #1 to #6) and 5 mutant fbn1-/- zebrafish (samples #7 to #11) were included.

All samples were decalcified during the sample preparation and scanned at 21.8 keV, 250mm sample-detector distance and 4x magnification. Reconstruction into image stacks was done with the Paganin phase retrieval algorithm. On the 2D image stacks resulting from synchrotron imaging, no differences regarding the

(micro)structure of the bulbus arteriosus of wild-type versus mutant fbn1-/- zebrafish were observed. Earlier comparison based on 2D histology slides of wild-type versus fbn1-/- zebrafish also did not show a (micro)structural cardiovascular phenotype [13].

For all samples, the bulbus could be captured completely in a single scan. The segmentation of the bulbus based on the synchrotron image stacks was fast as only a limited number of manual operations were needed. The majority of manual operations were needed to detach the bulbus from the ventricle.

Figure 6.17 shows the 3D reconstructions of the bulbus arteriosus in wild-type zebrafish. Each time, two views of the same sample are shown above each other. The bulbus structure was clipped shortly before the first branching of afferent branchial arteries, visible as the straight edges at the top (top row) or the right (bottom row). In the bottom row, near the top edge of the structures, remnants from the bulboventricular valve are visible. The rough surface shows that limited to no smoothing or interpolations were required to obtain these 3D reconstructions.

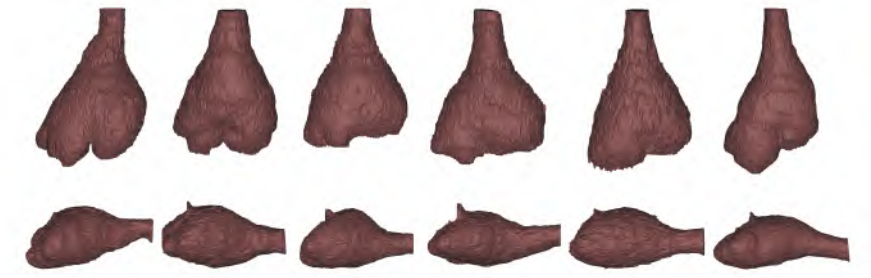

Figure 6.17: 3D reconstruction of the bulbus arteriosus in 6 wild-type adult zebrafish based on synchrotron CT-imaging.

Figure 6.18 shows the 3D reconstructions of the bulbus arteriosus in mutant fbn1-/- zebrafish, and the same views as in Figure 6.17 are displayed. Identical observations as described for the wild-type 3D reconstructions regarding the clipping, isolation and accuracy of the 3D reconstructions can be made.

After normalizing for body weight, no significant difference in (outer) volume of the bulbus was found for wild-type versus mutant fbn1-/- zebrafish. Visually, the 'streamlining' of the bulbi seems different

for mutant fbn1-/- samples compared to the wild-type samples, especially in the bottoms row view. In this view, the bulbi of fbn1-/- appear more bulgy near the ventricular side (left) while the wild-type bulbi overall appear more streamlined form the ventricular to aortic side (right).

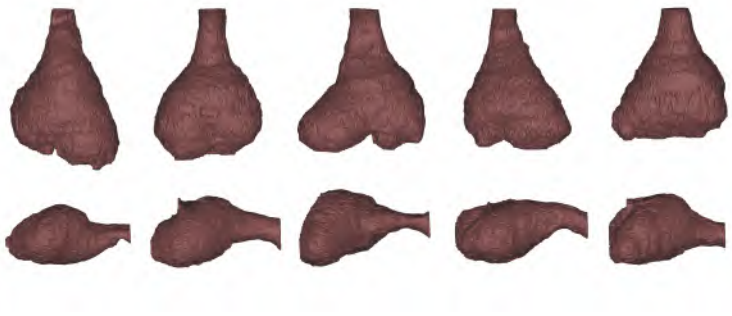

Figure 6.18: 3D reconstruction of the bulbus arteriosus in 5 mutant fbn1-/- adult zebrafish based on synchrotron CT-imaging.

The results should be expanded (larger sample size) and quantified by shape analysis. At this point, our results are not yet convincing to suggest a (hypothesized) phenotype for fbn1-/1 zebrafish. The results do however already illustrate how three-dimensional cardiovascular reconstructions could enhance the phenotyping possibilities in adult zebrafish. The reported subtle observation would not have been detected based on two-dimensional histology sections only. Three-dimensional imaging and 3D reconstruction are indispensable for comprehensive anatomical or morphological phenotyping.

6.7 Casting of the zebrafish vasculature

Casting here refers to injecting a liquid resin into the circulatory system and allowing it to polymerize and harden. If the casting technique is combined with corrosion of the soft tissue, a negative, solid, resin replica of the hollow vasculature space remains. First, CT-imaging of corrosion casts of the zebrafish vasculature is discussed in 6.7.1. Second, both CT-imaging and synchrotron CT-imaging of whole zebrafish after injecting of a contrast-enhanced casting agent are discussed in 6.7.2.

6.7.1 Corrosion casting computed tomography

The work presented in 6.7.1 is based on the publication:

Corrosion Casting of the Cardiovascular Structure in Adult Zebrafish for Analysis by Scanning Electron Microscopy and X-ray Microtomography (De Spiegelaere, W., Caboor, L., **Van Impe, M.**, Boone, M., De Backer, J., Segers, P. and Sips, P., ANATOMIA HISTOLOGIA EMBRYOLOGIA, 2020) [10].

The results presented below are limited to those involving original contributions of this PhD thesis' author.

Due to the small dimensions, vascular corrosion casting in adult zebrafish is challenging. The methodology to successfully obtain a corrosion cast of the zebrafish vasculature using the Mercox resin can be found in [10]. Imaging of these corrosion casts, below called samples, is now described.

The sample was scanned at the Ghent University Centre for X-ray Tomography (UGCT) with the Medusa scanner. The Medusa scanner is the re-designed version of the first UGCT sub-micron CT system, which is described in [190]. The sample was scanned in traditional cone beam mode, using a Photonic Science VHR detector with a pixel size of 9^2 µm^2, used in binning 4 mode. Octopus Reconstruction software version 8.9.4.2 was used to obtain a stack of reconstructed TIFF images at isotropic voxel size of 5.5^3 µm^3. The casted cardiovascular structure was segmented from this stack in Mimics 20.0 (Materialise, Leuven, Belgium) using a conventional thresholding approach based on the difference in grey values. As expected, the grey values where rather binary, except from the graphite mould on which the sample was mounted for imaging. The remaining graphite could be detected and separated from the cast structure during the segmentation. The automatic thresholding approach already resulted in an accurate segmentation which was then checked for irregularities. Minor flaws were corrected using the interpolation tool of Mimics, and the separation of atrium and ventricle was performed manually, but overall the complete segmentation was highly automated. The resulting 3D volume was lightly smoothed (20 iterations, smoothing factor 0.2) and shrinkage resulting from the smoothing operation was compensated.

As visualized in Figure 6.19, the resulting images and 3D reconstruction strikingly illustrate the morphological differences between the lumen of atrium and ventricle, the former having a smooth surface while the latter showed many indentations due to the strongly trabeculated nature of the ventricular endocardium. An animation of this 3D reconstruction can be found online.

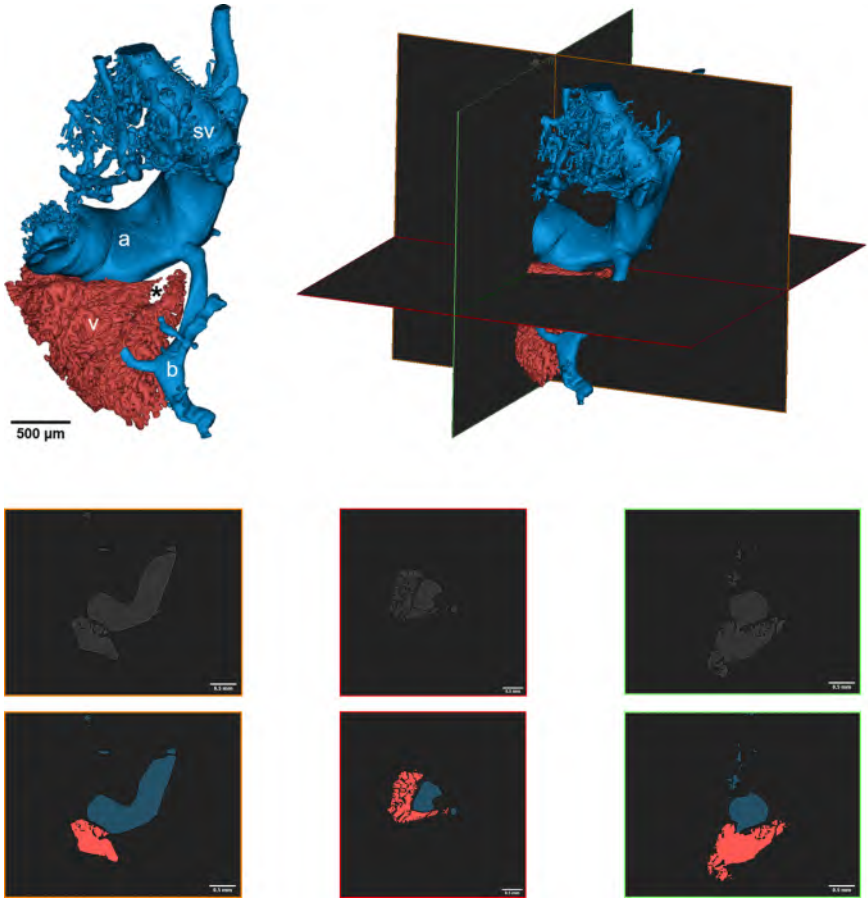

Figure 6.19: Top row (left) - Reconstructed rendering of a micro-CT scan of the zebrafish atrium (a) and ventricle (v). The sinus venosus (sv) can be seen draining into the atrium. The branchial vein (b) runs laterally next to the ventricle. The ventricle is color-coded in red, while the atrium and the connected venous vessels are highlighted in blue. Asterisk marks the injection site. Top row (right) - indication of different 2D views on the 3D reconstruction. Bottom row - unsegmentated and segementated 2D views. The same color coding as for the 3D reconstruction was applied. Adapted from [10].

Accurate and fast segmentation of the luminal spaces can thus be obtained using this methodology. However, a good end result requires adequate equipment and an experienced operator to inject the casting agent. Even in this scenario, the resulting cast is sometimes fragmented. Since only a cast of the luminal spaces remains after corrosion casting, all tissue information is lost. On the other hand, compared to the synchrotron imaging based segmentations described

earlier in this chapter, segmentation of the cast after micro computed tomography imaging is straight forward and highly automated.

6.7.2 Contrast-enhanced casting computed tomography

The work presented in 6.7.2 is based on the publication:

From Corrosion Casting to Virtual Dissection: Contrast-enhanced Vascular Imaging Using Hafnium Oxide Nanocrystals. (Goossens, E., Deblock, L., Caboor, L., Van den Eynden, D., Josipovic, I., Reyes Isaacura, P., Maksimova, E., **Van Impe, M.**, Bonnin, A., Segers, P., Cornillie, P., Boone, M., Van Driessche, I., De Spiegelaere, W., De Roo, J., Sips, P. and De Buysser, K., SMALL METHODS, 2024) [11].

The results presented below are limited to those involving original contributions of this PhD thesis' author.

The drawback that all tissue information is lost with the corrosion casting procedure explained in 6.7.1 is of course important. Histology imaging is not possible before nor after corrosion casting, while to (biomechanically) phenotype zebrafish HTAD models, structural (vessel wall) information is often indispensable. On the other hand, the more automated segmentation of corrosion casts compared to the segmentation of the blood volumes based on synchrotron data sets as explained earlier is faster and returns more accurate 3D geometries (e.g., of the ventricular cavity or gill vasculature).

Contrast-enhanced casting could combine advantages of casting and synchrotron imaging for zebrafish cardiovascular imaging. Corrosion of the sample is no longer necessary and the intact sample is scanned in situ, after casting, using (synchrotron) microCT imaging. Synchrotron scans of contrast-enhanced casted zebrafish using hafnium oxide nanocrystals are shown in Figure 6.20.

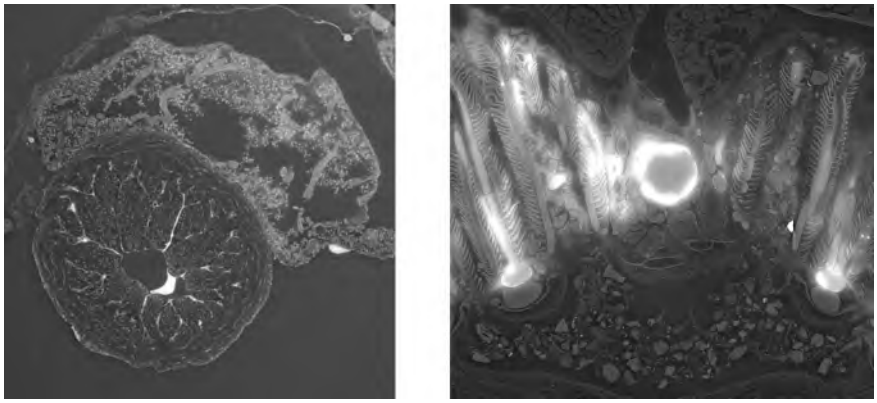

Figure 6.20: Synchrotron imaging of adult zebrafish. Cardiovascular casting with hafnium oxide nanocrystals was performed prior to scanning. The bulbus arteriosus and atrium (left image) as well as the gill vasculature (right) image are presented.

Figure 6.20 shows that both soft tissues and the contrast-enhanced cast is visible on the resulting synchrotron images. On the other hand, the casting is not optimal. For, e.g., the bulbus arteriosus and atrium (Figure 6.20 - left image panel), the blood spaces were barely filled. For, e.g., the gill vasculature (Figure 6.20 - right image panel), the blood spaces were largely filled but varying pixel intensities were observed in the scans and the cast also leaked out of the vasculature.

After further optimizing the experimental (contrast-enhanced) casting protocols, improved results were obtained. The cardiovascular blood spaces could then also be 3D reconstructed highly automatically after microCT or synchrotron microCT as reported, together with all experimental details, in [11].

CHAPTER 7

Fluid dynamics and biomechanics of the ventral aorta in adult zebrafish

The work presented in this chapter, except for the application example in 7.6, is based on the publication:

Fluid-structure interaction modeling of the aortic hemodynamics in adult zebrafish : a pilot study based on synchrotron x-ray tomography (**Van Impe, M.**, Caboor, L., Deleeuw, V., Olbinado, M., De Backer, J., Sips, P. and Segers, P., IEEE TRANSACTIONS ON BIOMEDICAL ENGINEERING, 2023) [8].

7.1 Intro

Phenotyping of cardiovascular structure and function extends beyond (anatomical and functional) imaging, and should also address biomechanical factors as indicators of aortic disease and as intrinsic components of the mechano-biological environment within which pathophysiological processes take place. WSS, i.e., the shear stress exerted by the blood flow on the endothelial cells that line the vessel wall, as well as the stress inside the vessel wall are key metrics [191–193].

Including biomechanical aspects is crucial for a comprehensive understanding of (defects in) the zebrafish cardiovascular system since the

biomechanical and mechano-biological role may be equally important as the biological functions. The first studies on cardiovascular biomechanics in zebrafish focused on the heart and described the embryonic ventricular fluid dynamics [5, 6, 87, 88, 90, 95, 194, 195]. So far, little is known about the biomechanical aspects of the aorta in zebrafish. Different techniques such as micro particle image velocimetry, confocal microscopy and light-sheet fluorescence microscopy can be used to describe blood flow and wall shear stress in the circulation of developing zebrafish. Both in the work of Lee et al. [85] and in the follow-up study by Choi et al. [86] an equivalent circuit model of the caudal microvasculature was used to investigate the link between atherosclerosis and low WSS. More recently, Roustaei et al. [196] also focused on the (caudal) microvasculature and investigated the effect of tail amputation and regeneration by using 4D CFD.

The novel zebrafish models of aortic disease will most likely direct biomechanical research in developing zebrafish to the proximal circulation as well. However, information on the cardiovascular fluid dynamics and biomechanics in adult zebrafish is completely lacking. Nonetheless, describing the aortic biomechanics in adult zebrafish would be valuable to validate hypotheses generated at developmental stages and to study progressive or late-onset conditions. In this study, we have modeled the fluid dynamics and biomechanics of the ventral aorta of adult zebrafish.

We applied synchrotron imaging in adult wild-type zebrafish, and combined the synchrotron-based 3D reconstructions of the aorta with in vivo high-frequency echocardiography measurements to set up both CFD and FSI models. This framework can be used for novel and advanced phenotyping of adult stage zebrafish models of cardiovascular disease, providing a deeper understanding of the mechano-biology of the cardiovascular system of a model organism that is widely used for the study of (the pharmacological treatment of) heritable cardiovascular pathologies.

7.2 Methods

7.2.1 Zebrafish (Danio Rerio)

N = 5 male, wild-type, 13 months old adult zebrafish from an AB background were used in this study. Zebrafish experiments were approved by the local ethical committee and conducted in strict accordance with the FELASA (Federation of European Laboratory Animal

Science Associations) guidelines and recommendations for the care and use of laboratory animals and in compliance with the Directive 2010/63/EU. All applicable international, national and institutional guidelines for the care and use of animals and the conduction of animal experiments were followed.

7.2.2 High-frequency ultrasound imaging

Echocardiography measurements were performed with a Vevo 2100 ultrasound machine (FUJIFILM VisualSonics, Toronto, Canada) and MS 700 linear array probe (FUJIFILM VisualSonics, Toronto, Canada). This probe has a frequency range of 30 - 70 MHz and a center frequency of 50 MHz. Tricaine methanesulfonate (MS-222) was used as anesthetic. The fish were first anesthetized in a 1x (0.16 g/L) tricaine solution and a new 0.5x (0.08 $\mathrm{g\,L^{-1}}$) solution was used for anesthesia maintenance during the measurement. Color Doppler and pulsed-wave Doppler measurements of ventricular in- and outflow were recorded with the probe in an abdominocranial short axis configuration at a 45° angle towards the abdominal wall [162]. B-mode images were gathered using longitudinal axis positioning of the probe over the midline of the zebrafish. Before and in between measurements, solutions were placed in a temperature-controlled water bath at constant temperature (28°C). A custom-made holder (3D printed), filled with the 0.5x tricaine solution and including spongy (submersed) clamps, was used to stabilize the zebrafish during echocardiography. Processing of the ultrasound measurements was performed in Vevo LAB (FUJIFILM VisualSonics, Toronto, Canada) by an experienced operator.

7.2.3 Specimen preparation for synchrotron imaging

Directly after ultrasound imaging, a lethal dose of tricaine (1 $\mathrm{g\,L^{-1}}$) was used to euthanize the fish. The samples were first fixed in modified Davidson's Fixative overnight, subsequently fixed in 4 % paraformaldehyde and then decalcified in citric acid. All samples were stored in 70 % ethanol (EtOH). On the day of transport, samples were rehydrated by subsequent changes to 50 % EtOH, 25 % EtOH and finally phosphate-buffered saline. As the main cardiovascular structures are located near the zebrafish head, only the most cranial part of the zebrafish was kept.

7.2.4 Synchrotron phase-contrast imaging

Propagation-based phase-contrast synchrotron X-ray imaging was performed at the TOMCAT (X02DA) beamline of the Swiss Light

Source (Paul Scherrer Institute in Villigen, Switzerland). Shortly before the scan, samples were immobilized in 1.5 mL Eppendorf tubes filled with agarose gel. All samples were oriented vertically, heads pointing upwards and Eppendorf tubes were fixed onto the robot sample holder using wax. Settings related to the beamline (21.8 keV monochromatic beam energy) and tomography scan (250 mm object-detector distance, 1501 projections, LUAg:CE 20 µm scintillator UPLAPO 4x objective, PCO.Edge 5.5 camera) were optimized during earlier studies on mouse samples [185]. The tomographic reconstruction into image stacks, including phase retrieval, was performed onsite using Paganin's algorithm [188]. Image stacks of 2560 x 2560 pixels and 2160 slices were obtained. At an isotropic voxel size of 1.625 μm^3, this corresponds to a field-of-view of 4.16 x 4.16 μm^2 (in plane) x 3.51 mm (axial).

7.2.5 Segmentation and 3D reconstruction

To reduce computational processing load during the segmentation and 3D reconstruction, images were first converted from 16-bit TIFF to 8-bit JPEG files and the image stacks were downsampled from 2160 to 540 images. This decreased stack sizes from 27.65 GB to 0.47 GB while still allowing accurate 3D reconstructions. The resulting image stacks were semi-automatically segmented in the medical image processing software package Mimics (Materialise, Leuven, Belgium). First, aiming for a mask including both the aortic wall and lumen, a threshold that showed a good trade-off between maximum inclusion of blood spaces and tissue walls of interest and minimum inclusion of neighboring structures was chosen. Then, using the built-in 'multiple slice edit' and 'interpolation' tools, the regions of interest were completely detached from surrounding structures. Holes in this mask were eliminated by using the 'smart fill' tool and on the resulting 3D part, the operations 'wrap' and 'smooth' were applied iteratively. Gill vasculature, sprouting from all pairs of afferent branchial arteries, was not included. A second mask of the lumen only was obtained by eroding the previous mask, hereby taking into account the (major) differences in wall thickness (aorta versus branchial arteries, regions more proximal or distal to the heart). Operations 'wrap' and 'smooth' were applied again on the 3D part. Throughout the whole segmentation process, local irregularities were manually corrected as needed. Both 3D reconstructions (surfaces) were exported to 3-Matic (Materialise, Leuven, Belgium) and uniformly re-meshed into volume meshes to ensure accurate importation in the finite element simulation software. The meshes used for the mesh sensitivity

study, including the final mesh, were defined later in the simulation software. There, the afferent branchial arteries were also clipped at approximately 1/3rd of the total branch lengths while the beginning of the aorta was clipped about 0.2 mm before the most proximal branching region.

7.2.6 Blood flow modeling

Blood was modeled as a Newtonian and incompressible fluid with density 1060 $\mathrm{kg\,m^{-3}}$ [5]. Lee et al. [197] reported a viscosity of 4.17 cP for adult zebrafish but to take the Fåhræus-Lindqvist effect [198,199] in the small aorta vessel into account, we estimated the viscosity value based on Figure 2 in the work of Pries et al. [199]. A representative diameter of 70 µm returns a viscosity of 2.2 cP, which was used in all simulations. For one sample, blood was also modeled as a power-law fluid defined by the parameters $m = 2.2$ cP and $n = 0.9949$ [197] to allow a direct comparison with the baseline results. Laminar blood flow through the ventral aorta was assumed, justified by the low Reynolds number ($Re \approx 15$) that was calculated based on the peak inlet velocity $\approx 300\,\mathrm{mm\,s^{-1}}$, inlet diameter ≈ 0.1 mm, and mentioned viscosity and density values. Body forces, including gravity, were not taken into account. This allows to write the governing equations, i.e., the continuity equation 7.1, and the Navier-Stokes equations 7.2, in following forms:

$$\nabla \cdot \vec{V} = 0 \tag{7.1}$$

$$\rho_f \frac{\partial \vec{V}}{\partial t} + \rho_f (\vec{V} \cdot \nabla)\vec{V} = -\nabla p + \nabla(\mu_f(\nabla \vec{V} + (\nabla \vec{V})^T)) \tag{7.2}$$

where ρ_f is the blood density, $\vec{V}$ the velocity vector, t denotes time, p is the fluid pressure and μ_f the dynamic viscosity.

Mass flow ($\mathrm{kg\,s^{-1}}$) was specified at the inlet. Neither pulsed wave Doppler signals nor cross section changes could be measured at the inlet location. A pulsed wave Doppler measurement of ventricular outflow is feasible but would not be suited as an approximation of the true inlet signal because the buffering effect of the bulbus arteriosus (the structure in between the ventricle and inlet location in our model) should be taken into account. Therefore, the overall shape of the used inlet times profile is a simplified version of the profile in Figure 1 of Korsmeyer et al. [200] which describes ventral

aortic flow in yellowfin tuna. Zebrafish sample specific measurements of stroke volume, cardiac cycle time and the ratio of aortic ejection time (AET) cardiac cycle time were used to define the inlet signals completely. As an example, the applied inlet signal as well as the pulsed wave Doppler recording of ventricular outflow for the same sample are depicted in the right part of Figure 7.1.

Pressure at the outlets was defined by a purely resistive relationship with the respective flow at that outlet. A total resistance of 2 $\mathrm{mmHg\,s\,mm^{-3}}$ was found assuming a rudimentary mean pressure of 1 mmHg and average flow rate of 0.5 $\mathrm{mm^3\,s^{-1}}$. Based on the regular appearance of gill vasculature, fairly equal flow splits were assumed and this was obtained by applying resistances R, $2.5R$, $4R$ and $3.5R$ at the outlets of aortic arches I, II, III and IV, respectively. This is also illustrated in the left part of Figure 7.1. R equals 7.74 $\mathrm{mmHg\,s\,mm^{-3}}$ considering the total resistance value and parallel connection of all outlets. In CFD simulations, a no-slip condition was applied at the remaining wall surface.

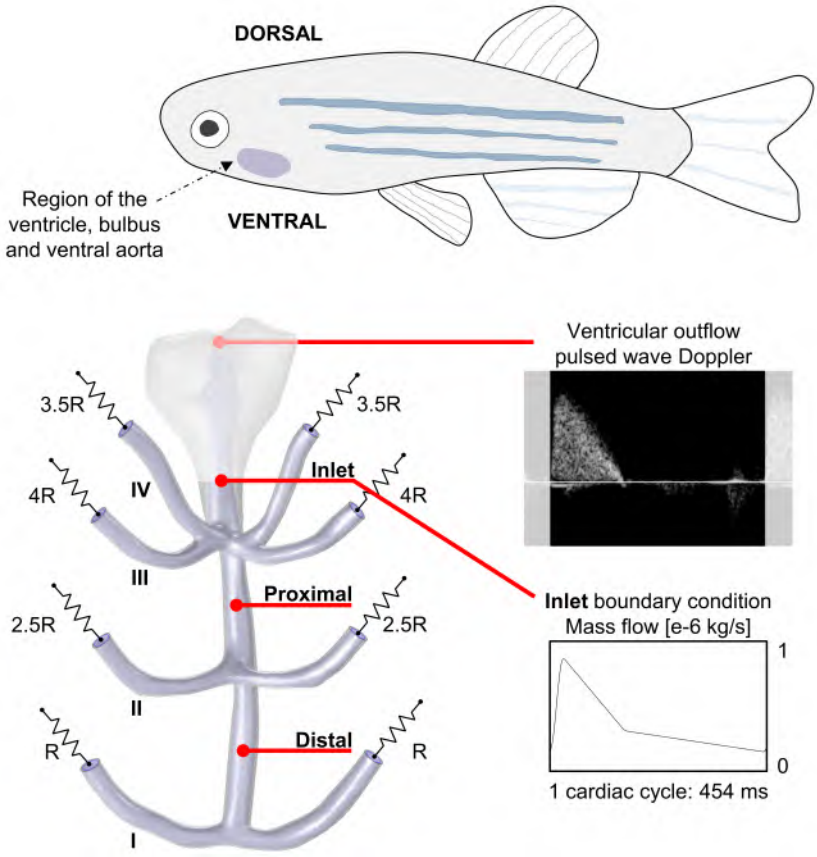

Figure 7.1: The location of the ventral aorta is indicated in purple on the zebrafish drawing (top) and a dorsal view of the ventral aorta (and bulbus) is shown below this drawing. Resistive boundary conditions are applied at the eight outlets in the model (same for all samples). Pulsed wave Doppler measurements of ventricular outflow are feasible but clearly differ from the assumed aortic inlet waveform due to the buffering effect of the bulbus arteriosus. The bulbus (shaded) is not explicitly included in the model and the actual inlet location and inlet mass flow boundary condition is depicted. The indicated proximal and distal locations are central locations where flow, pressure and cross section area are evaluated over time. Also pulsed wave velocity (PWV) is calculated at these locations. The aorta geometry and signals of sample #1 are shown.

During the first milliseconds of the simulations, a smoothed step function was used to ramp up the inlet signal from zero. The cycle-to-cycle variations after two cardiac cycles were negligible and the second cycle was post-processed to obtain the results. The CFD Module of finite element software COMSOL Multiphysics v5.6 (COMSOL Inc., Stockholm, Sweden) was used for all simulations.

7.2.7 Aortic wall and fluid-structure interaction modeling

In FSI simulations, also the aortic wall and its interaction with the fluid domain was modeled, again using COMSOL multiphysics (CFD Module, Nonlinear Structural Materials Module and Structural Mechanics Module or MEMS Module).

The FSI problem was solved by using the Arbitrary Lagrangian-Eulerian method. The governing equation to model the deformation of the aortic wall is based on the linear momentum conservation principle, 7.3:

$$\rho_s \frac{\partial^2 \vec{U}}{\partial^2 t} - \nabla \vec{\vec{\sigma}} = \rho_s \vec{b} \tag{7.3}$$

where ρ_s is the density of the vessel wall, $\vec{U}$, the displacement vector, t denotes time, $\vec{\vec{\sigma}}$ is the Cauchy stress tensor and b the vector representing body forces applied on the structure. As no (experimental) reference data on the material properties of the aorta in zebrafish was available, a density ρ_s of 1000 $\mathrm{kg\,m^{-3}}$ and incompressibility were assumed [201]. The fairly simple and for biological tissue common hyperelastic Neo-Hookean constitutive law was selected. The strain energy density function W can thus be written as:

$$W = \frac{1}{2}\mu_{Lamé}(I_1 - 3) \tag{7.4}$$

where $\mu_{Lamé}$ is the second Lamé parameter or shear modulus (material constant) and I_1 is the first invariant of the right Cauchy-Green deformation tensor. A shear modulus mu of 18 kPa was tuned to obtain plausible diameter (volume) expansions. The percentual diameter (volume) expansions from diastole to systole were assumed to be similar to the data reported in [202] on tuna, also a teleost (but much larger) fish. All inlet and outlet ends of the vessel wall were fully constrained whereas the outer vessel wall surface was free to move. Regarding earlier assumptions about blood flow modeling, the no-slip boundary condition at the wall (CFD simulations) was replaced by a coupled interface between the fluid and vessel walls (FSI simulations) to satisfy the displacement and traction equilibrium. Again, the inlet signal was ramped up from zero and two cardiac cycles were simulated of which only the second cycle was post-processed to obtain the results.

7.2.8 Derived hemodynamic parameters

Next to basic metrics such as flow, pressure, wall shear stress and principal stress inside the vessel wall, three specific derived hemodynamic parameters, namely time-averaged wall shear stress (TAWSS), oscillatory shear index (OSI) and pulse wave velocity (PWV) were evaluated. TAWSS is defined as follows (7.5):

$$TAWSS = \frac{1}{T}\int_0^T |\vec{\tau_w}|dt \tag{7.5}$$

where T represents one cardiac cycle, $\vec{\tau_w}$, the instantaneous WSS vector and t denotes time. The oscillatory shear index reflects the pulsatile aspect of WSS and is calculated according to 7.6:

$$OSI = \frac{1}{2}(1 - \frac{|\frac{1}{T}\int_0^T \vec{\tau_w}dt|}{\frac{1}{T}\int_0^T |\vec{\tau_w}|dt}) \tag{7.6}$$

PWV was calculated based on the Bramwell-Hill equation, 7.7:

$$PWV = \sqrt{\frac{A_{min}}{\rho_s}\frac{\Delta P}{\Delta A}} \tag{7.7}$$

where A_{min} is the minimal luminal area, ρ_s the density of the vessel wall, and ΔP and ΔA denote the difference between maximal and minimal blood pressure and luminal area, respectively, during the cardiac cycle.

7.2.9 Mesh and solver considerations

For sample #1, a complete mesh sensitivity analysis was conducted with unstructured, corner refined boundary layer meshes of different sizes (Figure 7.2 and Figure 7.3). Convergence was considered to be achieved for the meshes of 444 716 elements (CFD) and 558 242 elements (FSI). The input parameters of these meshes were then used to define the meshes of all samples, resulting in a similar number of elements for all cases. A direct (PARADISO solver) and fully coupled (Newton method nonlinear solver) scheme was used for all simulations. A relative tolerance of 1e-3 was defined and time steps were determined by the solver but at least one evaluation in every 0.002 s interval was enforced.

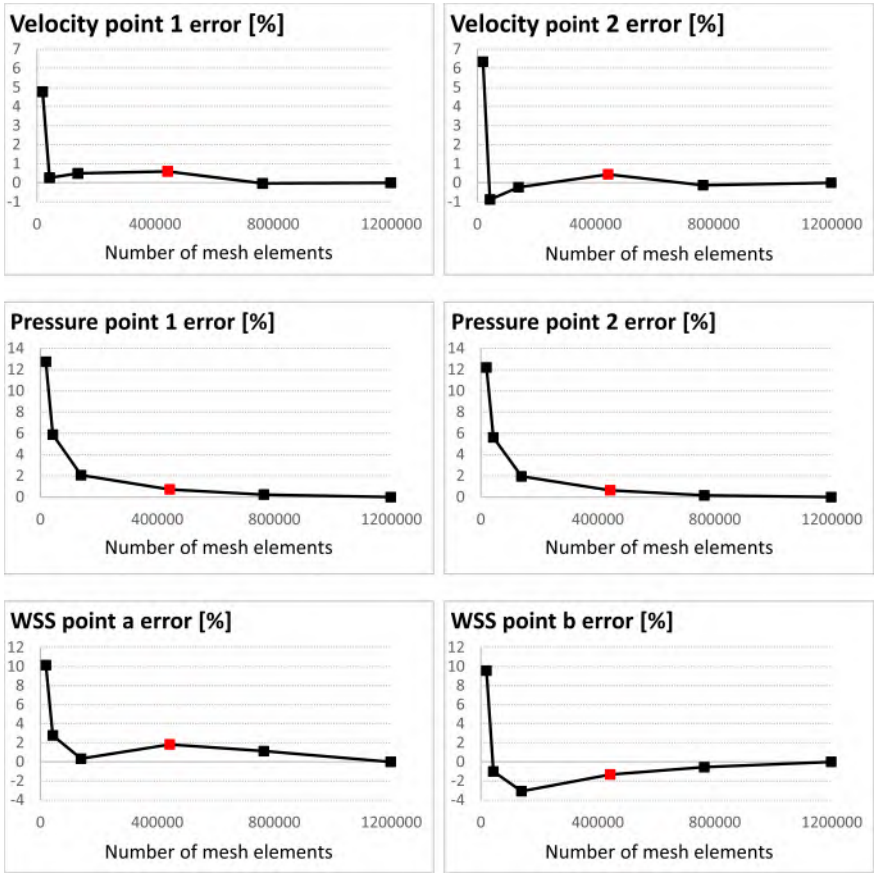

Figure 7.2: Mesh sensitivity analysis for CFD simulations. Six meshes of different size (18 935, 42 613, 138 939, 442 716, 763 938 and 1 197 699 elements) were considered and each time the relative error (expressed in %) compared to the result for the most dense mesh of 1 197 699 elements is shown. Results for individual points in the geometry at one specific time point are shown to illustrate the mesh convergence. Convergence was also validated for several time- and space-averaged metrics. The mesh of 442 716 elements (indicated in red) was selected as the final mesh. Using this mesh size, a CFD simulation of two cardiac cycles roughly took 30 minutes on a 64 GB RAM Intel Xeon CPU E5-1650 v3 @ 3.50GHz machine.

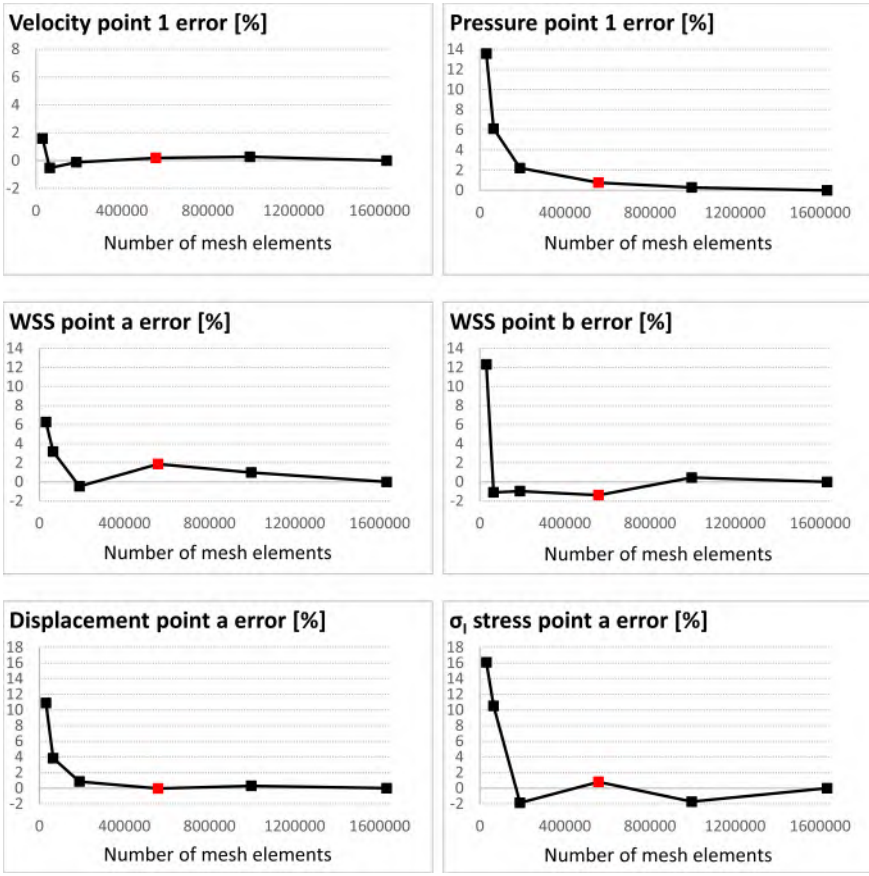

Figure 7.3: Mesh sensitivity analysis for FSI simulations. Six meshes of different size (30 848, 64 447, 188 432, 558 242, 996 185 and 1 632 339 elements) were considered and each time the relative error (expressed in %) compared to result for the most dense mesh of 1 632 339 elements is shown. Results for individual points in the geometry at one specific time point are shown to illustrate the mesh convergence. Convergence was also validated for several time- and space-averaged metrics. The mesh of 558 242 elements (indicated in red) was selected as the final mesh. Using this mesh size, a FSI simulation of two cardiac cycles roughly took three hours on a 64 GB RAM Intel Xeon CPU E5-1650 v3 @ 3.50GHz machine.

7.3 Results

7.3.1 Synchrotron micro-CT based cardiovascular structure and segmentation

All major cardiovascular structures, including the atrium, ventricle, bulbus arteriosus and ventral aorta were clearly visible on the synchrotron images (Figure 7.4). Also all four pairs of afferent branchial

arteries could be identified. Gill vasculature sprouts in regular fashion and in the end all afferent branchial arteries completely evolve into the gill microcirculation.

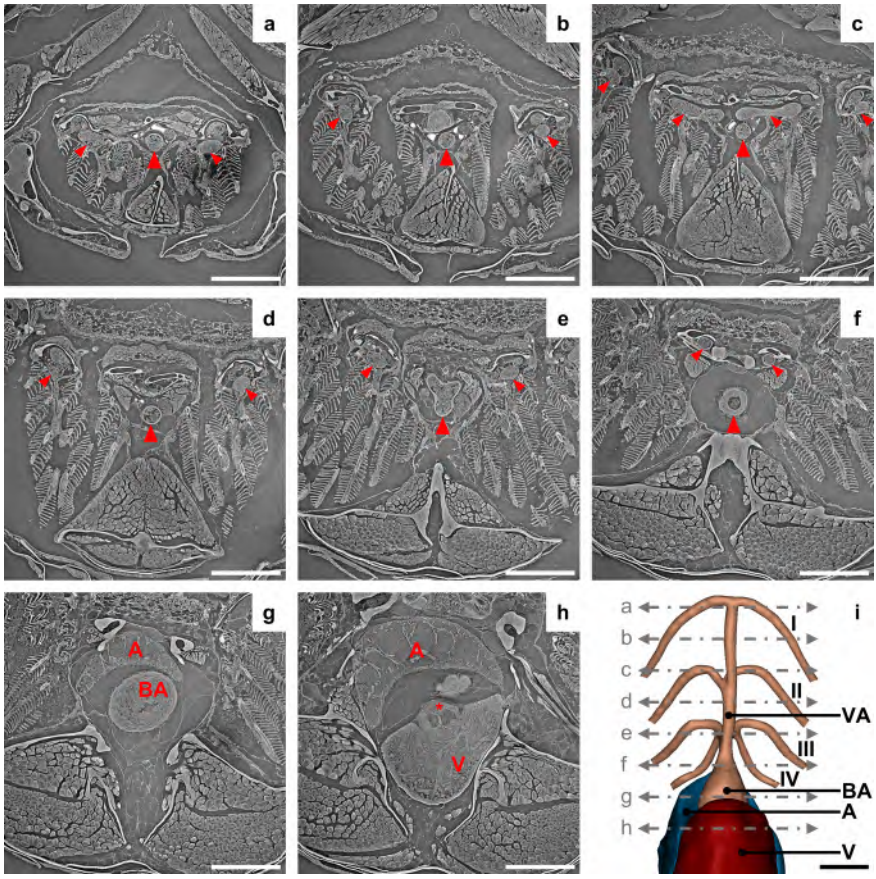

Figure 7.4: Synchrotron imaging can be used to visualize and 3D reconstruct all major cardiovascular structures in adult zebrafish. Panels a-h show equally spaced (325 µm) axial cross sections of the ventral aorta (large arrowheads), afferent branchial arteries (small arrowheads), bulbus arteriosus, atrium and ventricle. The asterisk in panel h indicates the aortic valve region. Panel i shows the resulting 3D reconstruction with indications of the locations of all cross sections. The ventricle, atrium and all four pairs of afferent branchial arteries (named I-IV) are clipped in the 3D visualization. VA: ventral aorta, BA: bulbus arteriosus, A: atrium, V: ventricle. Scale bars: 500 µm.

Blood is then collected in the efferent branchial arteries, located directly next to their afferent counterparts (not included in the 3D reconstruction in panel i of Figure 7.4 but visible right above the afferent

branchial arteries in panels a-e of Figure 7.4). For some samples, the efferent branchial arteries could be tracked until the merge with the dorsal aorta (not visible in Figure 7.4). Representative results for the segmentation of the aortic wall and lumen are shown in Figure 7.5. For CFD simulations, only the lumen boundaries are used (red) whereas for FSI simulations both the lumen boundaries and outer vessel wall boundaries (yellow) are used. This way, the CFD geometry and the fluid domain in the FSI geometry at time step zero are identical.

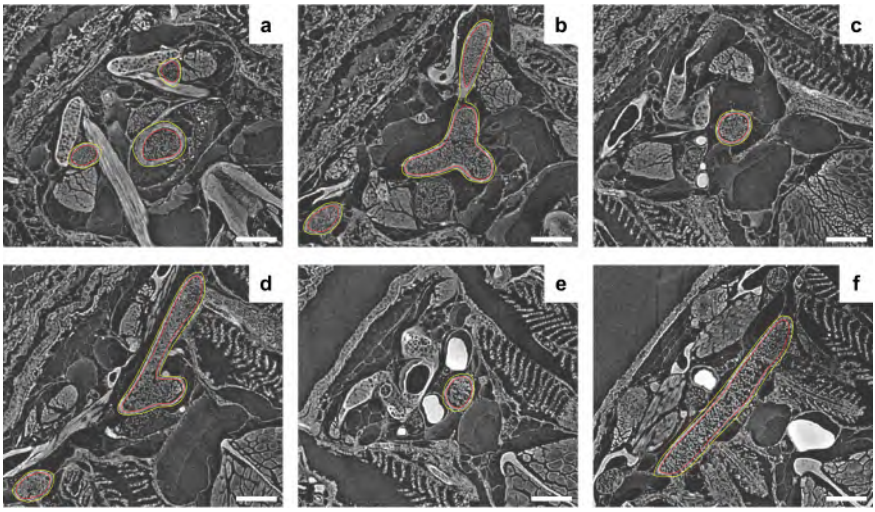

Figure 7.5: Semi-automatic segmentation of the aortic vessel wall and lumen. The outer boundary of the vessel wall is traced in yellow whereas the inner boundary of the vessel wall, which is also the outer boundary of the blood lumen, is traced in red. Six different cross sections of the same sample are shown as a representative example. Panels a-f show cross sections of the ventral aorta in proximal to distal order. Panel a shows a cross section around the inlet location (end of the transition from the bulbus arteriosus to the ventral aorta which is before the first branching region). Panel b shows a cross section near the first branching region (branchial arteries III and IV). Panel d shows the middle branching region (branchial arteries II) whereas panel f shows the last branching region (branchial arteries I). Panels c and e show the ventral aorta in non-branching regions. Scale bars: 100 µm.

7.3.2 Measurements of cardiovascular structure and function

Table I provides a quantitative summary of both ex vivo structural data and in vivo functional data of the five samples. Structural parameters (row 3-6) result from the synchrotron based segmentations

and 3D reconstructions. Functional parameters (row 7-11) result from high-frequency B-mode echocardiography measurements. The reported heart rate corresponds to the (B-mode based) cardiac cycle time measurement and cardiac output was calculated from the stroke volume and heart rate values. Body weight and length (row 1-2) were measured directly after the echocardiography experiments.

7.3.3 Hemodynamics of the aorta

For the sake of clarity, this results section mainly focuses on data retrieved from the FSI simulations. CFD results are shown as well but the similarities and differences with the FSI data are considered in the discussion

7.3.3.1 Pressure, blood flow and pulse wave velocity

Pressure (mmHg), blood flow ($mm^3\,s^{-1}$) and luminal area (mm^2) were evaluated around the middle of both straight segments of the ventral aorta (called 'proximal' and 'distal' location as displayed in Figure 7.1). Figure 7.6 depicts the time profiles of these metrics for sample #1 at both locations.

Table 7.1: Quantitative summary of synchrotron-based structural cardiovascular parameters and echocardiography-based functional cardiovascular parameters.

	#1	#2	#3	#4	#5
Body weight [mg]	216	290	191	187	230
Length [mm]	28	32	29	27	30
Aorta lumen vol. [$10^{-3}mm^3$]	25	51	36	34	33
Aorta wall vol. [$10^{-3}mm^3$]	15	22	19	16	15
Avg. wall thickness [µm]	9.14	9.53	8.34	11.65	8.89
Aorta lumen inlet [$10^{-3}mm^2$]	7.11	6.29	5.81	7.28	7.06
Stroke vol. [µL]	0.15	0.48	0.15	0.29	0.26
Total (cardiac) cycle [ms]	454	440	428	390	444
Heart rate [bpm]	132	136	140	154	135
Cardiac output [$\mu L\,min^{-1}$]	19.7	65.91	20.5	44.1	35.3
Ratio AET/total cycle [-]	0.34	0.34	0.33	0.34	0.29

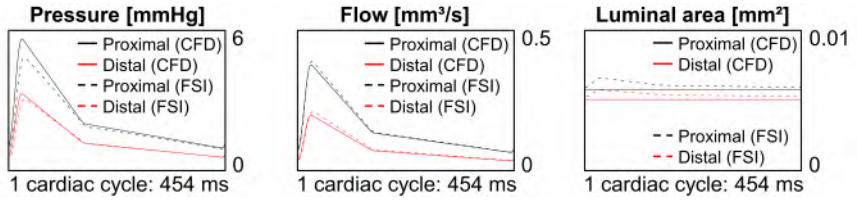

Figure 7.6: A comparison of pressure, blood flow and luminal area time profiles for sample #1 in CFD (solid lines) and FSI (dashed lines) simulations. Black lines depict the profiles at the proximal location while red lines are evaluated at the distal location. The rigid wall modeling in the CFD simulations implies a constant luminal area over time and elevates pressure compared to the FSI case. Flow at both the proximal and distal location is almost identical for the CFD and FSI case and the small difference corresponds to a slight change in flow splits. Each time one complete cardiac cycle is shown.

At the same locations, pulse wave velocity (PWV) was evaluated with the Bramwell-Hill relationship (7.7). A PWV of 1.74 - 2.25 $\mathrm{m\,s^{-1}}$ (observed range considering all 5 samples) was obtained at the proximal location whereas a PWV of 1.89 - 2.09 $\mathrm{m\,s^{-1}}$ was obtained downstream at the distal location. For each sample, the time-averaged mass flow splits (compared to the inlet mass flow) of all four pairs of branchial arteries fell within the 20 - 31 % range. For sample #1, a FSI animation of the flow throughout the complete cardiac cycle is available online. Arrows in this video point towards the local flow direction and both the color and length (on a logarithmic scale) of the arrows represent velocity magnitude. Also CFD time profiles are presented in Figure 7.6.

In Figure 7.9, oscillatory shear is presented by plotting the OSI and peak OSI values of 0.007 - 0.059 were found. A comparison of the WSS at systolic peak for the Newtonian versus the power-law fluid model returned average and maximum differences of 3.32 % and 5.45 %, respectively. CFD results of the OSI are reported in Figure 7.10.

7.3.3.2 Wall shear stress

TAWSS is displayed in Figure 7.7 Surface-averaged TAWSS values of 2.52 - 5.49 Pa were obtained. A clear visualization of lowest TAWSS regions is depicted at the bottom of Figure 7.7 by using a different color scale. The 5th and 10th percentiles of TAWSS ranged between 1.44 - 2.91 Pa and 1.58 - 3.24 Pa, respectively. TAWSS CFD results are reported in Figure 7.8. For sample #1, a FSI and CFD) animation of WSS magnitude throughout the complete cardiac cycle is available

online. Surface-averaged WSS at systolic peak was 5.71 - 11.47 Pa in FSI simulations.

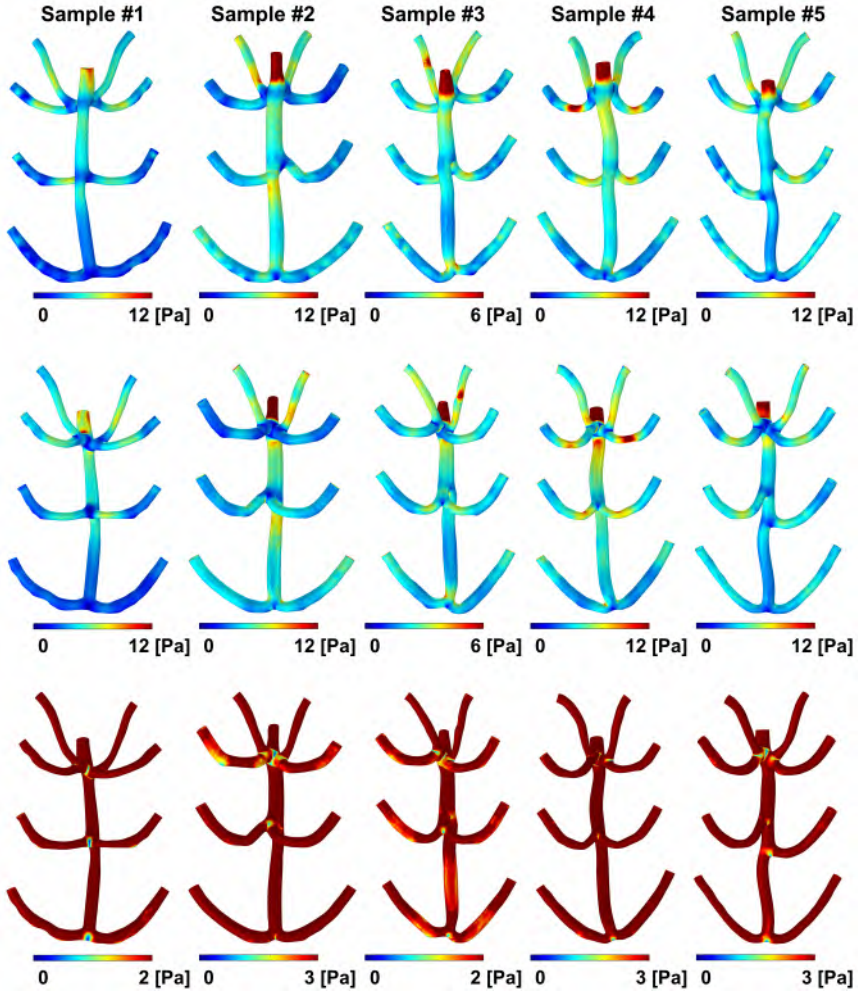

Figure 7.7: Time-averaged wall shear stress (TAWSS) in FSI simulations. For each sample, two views are provided (a view of the ventral side on the top row and a view of the dorsal side on the middle row). At the bottom, the middle row is replotted on a different color scale to get a more clear visualization of lowest TAWSS regions. Note the different color scale for sample #3 in all rows as well as for sample #1 in the bottom row.

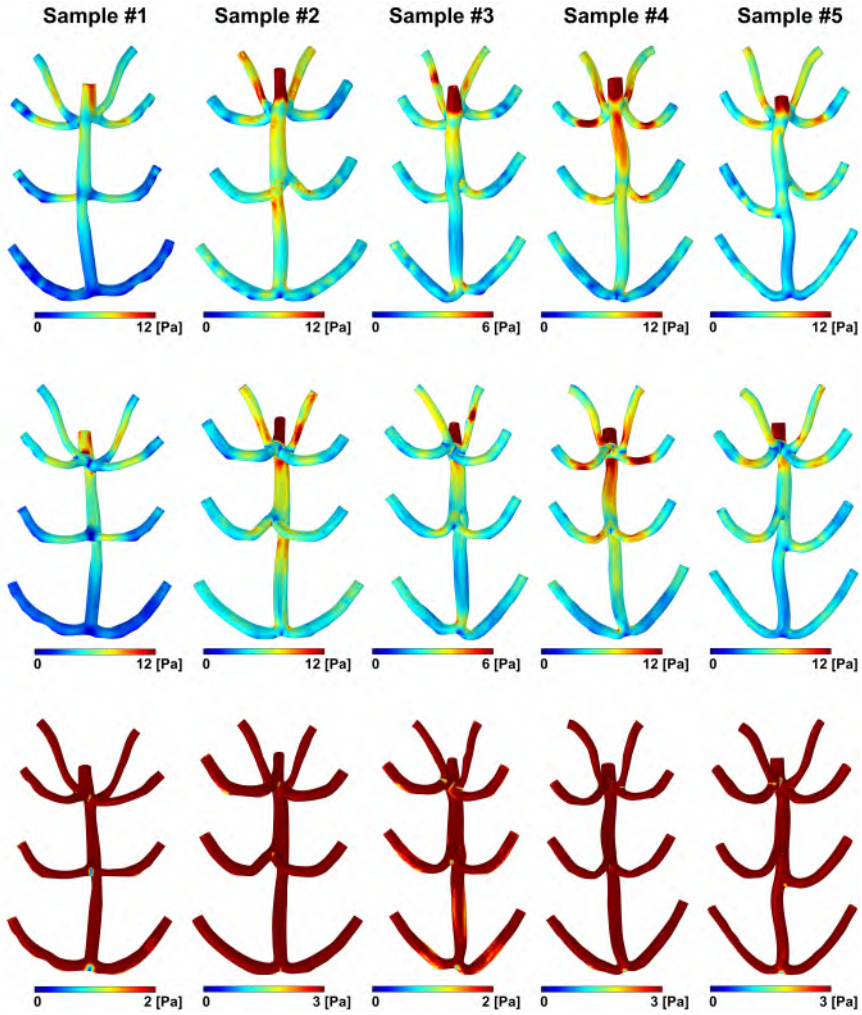

Figure 7.8: Time-averaged wall shear stress (TAWSS) in CFD simulations. For each sample, two views are provided (top row and middle row). At the bottom, the middle row is replotted on a different color scale to get a more clear visualization of lowest TAWSS regions. Note the different color scale for sample #3 in all rows as well as for sample #1 in the bottom row.

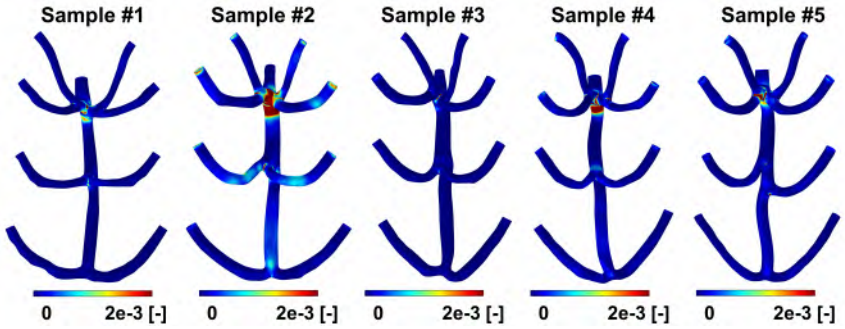

Figure 7.9: Oscillatory Shear Index (OSI) in FSI simulations. The OSI can take values between 0 and 0.5 corresponding to a uni-directional flow and reversing flow with no mean direction, respectively.

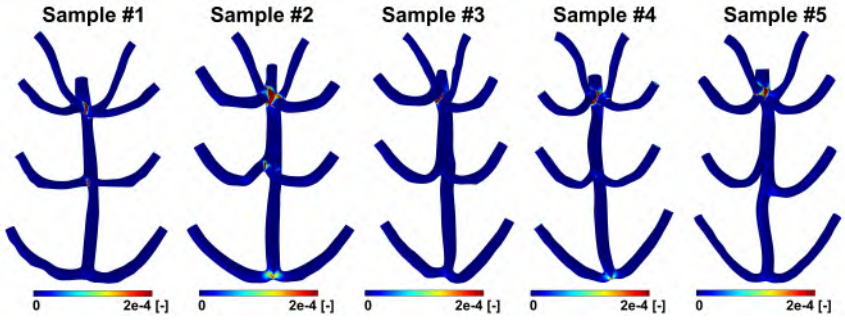

Figure 7.10: Oscillatory Shear Index (OSI) in CFD simulations. In general, the OSI can take values between 0 and 0.5 corresponding to a uni-directional flow and reversing flow with no mean direction, respectively.

7.3.3.3 Stress inside the vessel wall

First principal stress, evaluated at the inner vessel wall surface at systolic peak, is shown in Figure 7.11. Peak values of 25 - 88 kPa were obtained. For sample #1, an animation of first principal stress at the inner and outer vessel wall surfaces throughout the complete cardiac cycle is available online.

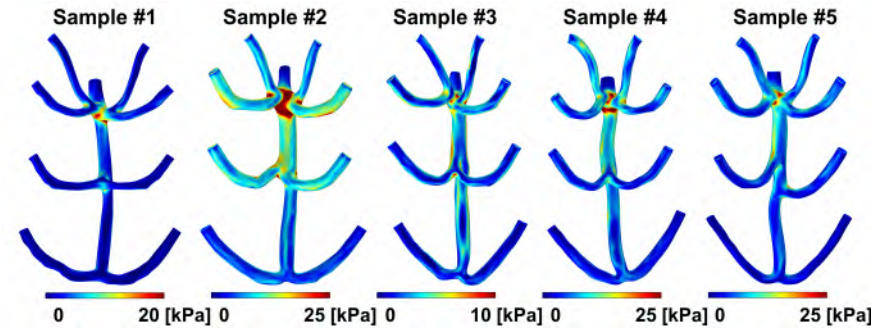

Figure 7.11: First principal stress at systolic peak in FSI simulations. The inner surface of the vessel wall is visualized. Note the different color scale for samples #1 and #3.

7.4 Discussion

In this study we used ex vivo synchrotron imaging and in vivo high-frequency echocardiography to set up unprecedented CFD and FSI finite element models of the ventral aorta in adult zebrafish. Relevant hemodynamic parameters such as flow, pressure, wall shear stress related metrics and first principal stress in the vessel wall are evaluated.

The general image quality of our synchrotron experiments agrees with other studies that applied synchrotron imaging to juvenile and adult zebrafish [151–153, 175]. None of the other studies explicitly focused on the cardiovascular structures and therefore the 3D reconstructions of the aorta and aortic arches presented here provide a novel, useful anatomical reference. Aortic arches II of sample #5 connect to the aorta at different (asymmetric) locations. Apart from this remarkable difference, the geometry of the ventral aorta segments and their branching points is similar. A visual evaluation of the segmentation (Figure 7.5) shows a good overall accuracy of the semi-automatic segmentation approach. The thickness of the vessel wall was slightly overestimated in some regions and this was tolerated to allow a semi-automatic rather than a fully manual segmentation. Moreover, the stiffness of the aorta greatly influences the mechanical behavior and the slight overestimation of wall thickness in certain regions is likely to be negligible compared to the simplifications and assumptions regarding material model and constants.

The distribution in the body weights of the zebrafish used for synchrotron imaging reflects the natural biological variability. The echocardiography-based measurements of stroke volume (0.15 - 0.48

μL) and heart rate (133 - 154 beats per minute (bpm)) fall within the range reported in the literature [163]. Age and anesthesia (time) also affect these values. Variability in simulated hemodynamic results is present as well but the overall patterns of simulated hemodynamic results agree well between different animals as can be appreciated from for example Figure 7.7, Figure 7.9 and Figure 7.11. Note that for some samples, the color scaling was altered to present this similarity more clearly.

First, FSI fluid dynamics results are discussed. Although a direct quantitative scaling of zebrafish to human flow field parameters is difficult, we still compare the results with human and mice data to put the observed order of magnitudes in context. Simulated mean pressures at the distal location (1.25 - 3.03 mmHg) agree with the mean pressure reported by Hu et al. ($\approx$ 1.25 mmHg) [48] whereas the simulated mean pressures at the proximal location (1.65 - 4.08 mmHg) are slightly higher. Obtained peak pressures at the proximal (3.91 - 8.76 mmHg) and distal (3.00 - 6.79 mmHg) locations are higher but still in the same order of magnitude compared to the ventral aortic peak pressures reported by Hu et al. ($\approx$ 2.16 mmHg) [48]. Experimental blood pressure measurements in zebrafish are challenging because of the small vessel and chamber dimensions (long axis ventricle $\approx$ 1 mm, inlet diameter ventral aorta $\approx$ 0.1 mm) and the difficulty of applying a pressure servo null system invasively at these sites. The report by Hu et al. in 3 month old zebrafish is the only reference on arterial blood pressure in adult zebrafish that we could identify. The same group showed that ventricular systolic and diastolic as well as aortic peak pressures increase geometrically with age during development [203] and later measurements by Kopp et al. [104] in 2.5-3 days post fertilization (dpf) embryos are in line with their reported values.

Recently, much higher peak ventricular pressures in 5 dpf zebrafish were reported [204] whereas stroke volumes were comparable to the measurements of [203] and [104]. This emphasizes the need for both more longitudinal (throughout development until late adulthood) and better documented (mentioning the precise measurement location in the ventral aorta) pressure measurements in zebrafish. Overall, ventral aortic pressures resulting from our model seem plausible and agree with the reported order of magnitudes.

The evaluated wall shear stress related metrics (WSS, TAWSS and OSI) revealed consistent patterns for all samples. TAWSS is lowest

near the dorsal side of the branching regions (not considering the aortic arches). Throughout the complete cardiac cycle, the instantaneous WSS pattern is very similar to the TAWSS pattern and only differs in magnitude. WSS magnitudes at systolic peak are roughly double the TAWSS values. Simulated WSS magnitudes are higher compared to adult mice and humans and more similar to WSS magnitudes observed in prenatal mice [205] or the human fetus umbilical arteries [206]. Due to the different aorta geometry in zebrafish compared to mammals, a comparison of overall WSS and TAWSS patterns between species is difficult. The (branched) zebrafish aorta geometry actually resembles, to some extent, the aorta and aortic arches of the chick embryo and also WSS magnitudes of the same order of magnitude are observed [207]. OSI patterns show that the dorsal sides of the most proximal branching regions are also the locations with highest oscillatory shear. Some variability is present in terms of the magnitude and size of this most proximal peak OSI region (especially for samples #2 and #4) but the general pattern is consistent. Highest observed oscillatory shear regions thus largely coincide with lowest wall shear stress regions. OSI magnitudes are very low compared to, e.g., mice [208] and humans [209]. The very low oscillatory shear may seem counterintuitive due to the presence of several branching regions, but can be explained by the very low peak Reynolds number (≈ 15) and associated highly laminar flow behavior. Peak Reynolds numbers in the aorta of adult mice (≈ 350) and humans (≈ 7500) are considerably higher which leads to more disturbed flow regions.

For four out of five cases, pulse wave velocity was higher at the distal measurement location compared to the proximal measurement location. The values of approximately 2 $\mathrm{m\,s^{-1}}$ are of the same order of magnitude as PWV in the healthy human and mouse aorta. In our simulations, highest first principal stress locations in the vessel wall are observed near the most proximal branching region. Around and in between the connections of aortic arches III and IV, several stress hotspots were found. First principal stress was also relatively high near the middle branching region. The location of peak first principal stress around the most proximal branching region is not totally unexpected, but it is interesting to see such distinct and similar first principal stress hotspots and patterns in all samples. Note that some similarities can be observed between the overall patterns of low TAWSS (Figure 7.7 5 bottom row), OSI (Figure 7.9) and first principal stress (Figure 7.11). The highest values of first principal

stress values are one order of magnitude below the values reported in mice [193] and humans [210].

Comparing the flow results of FSI and CFD simulations, most key findings agree with literature. Peak pressures are higher throughout the model in CFD simulations because of the rigid lumen walls (Figure 7.6). Also (peak) instantaneous WSS and TAWSS are slightly higher in CFD simulations whereas the overall patterns are almost identical (see the video as well as Figure 7.7 versus Figure 7.8). Several groups reported that OSI patterns and magnitude in both mice [211] and humans [209] can differ considerably in CFD and FSI simulations. No clear difference in the OSI patterns of CFD and FSI simulations was observed, but OSI magnitudes were about one order of magnitude lower in CFD simulations compared to FSI simulations (Figure 7.9 versus Figure 7.10). Overall, CFD simulations can give accurate qualitative information on the fluid dynamics. Whereas FSI magnitudes of all metrics are likely to be more accurate, the increased computational effort and uncertainty of several model parameters (inlet and outlet boundary conditions, stiffness aorta vessel...) are arguments in favor of CFD simulations if only the mentioned flow related parameters are important. FSI simulations can still be necessary depending on the application, e.g., to quantify first principal stress inside the vessel wall or to study disease conditions that affect vascular wall properties.

Below, we discuss certain choices and assumptions and also address the limitations of the current models and modeling approach. Synchrotron micro-CT imaging was used in order to provide an optimal combination of resolution and soft tissue contrast. Vascular corrosion casting could allow to use traditional micro-CT instead of synchrotron radiation while a high level of detail showing, e.g., the trabeculation of the ventricle [10], can still be obtained. Corrosion casting however cannot be used to reconstruct the vessel wall geometry as all tissue information is lost. On the other hand, corrosion casting could provide fast segmentations of the CFD geometries and the obtained 3D reconstructions may actually be a (slightly) better representation of the in vivo intraluminal dimensions. The vascular corrosion casting workflow [10] as well as our presented synchrotron imaging workflow are intrinsically ex vivo procedures. MRI seems a promising option to obtain in vivo three-dimensional geometries but remains very challenging in zebrafish. Only for larger structures like the atrium, ventricle and bulbus arteriosus, the use of MRI was successfully reported [150, 174]. At this point, MRI nor 4D high-frequency

echocardiography provides sufficient resolution to evaluate the deformation of the ventral aorta and aortic arches in adult zebrafish. If imaging techniques become available that allow accurate 3D reconstructions of in vivo measurements of the aorta structure, simulations including pre-stress can be considered. Customized high-frequency ultrasound set ups can be used to push resolution limits as recently reported [159, 160] but require specialized material and staff. PWV or motion mode (M-mode) ultrasound measurements in the ventral aorta could become feasible in the near future and can then be used to construct the inlet signal and to provide in vivo validation of simulation results.

A reduced zebrafish blood viscosity was used because the Fåhræus-Lindqvist effect may play a prominent role. In small arteries ($D < 0.3$ mm), red blood cells tend to migrate towards the center of small vessels and effective viscosity near the wall is more similar to the viscosity of plasma [198, 199]. Although often accepted for mice and humans, the assumption to model blood as a Newtonian fluid is not trivial for zebrafish. In (adult) mice and humans, the compressible effect of individual red blood cells is mostly negligible when looking at the whole blood suspension as vessel diameters are usually large compared to blood cell diameters. However, for the zebrafish circulation, red blood cell diameters tend to approach (some) vessel diameters which could make blood viscosity more shear rate dependent and therefore non constant. Two arguments make the constant viscosity assumption (Newtonian fluid) in our models still reasonable: (i) only large vessels of the zebrafish circulation were included in our simulations and (ii) Lee et al. [197] demonstrated that blood viscosity in adult zebrafish stays fairly constant over the vast majority of shear rates encountered during the simulations. This is also reflected by the small WSS differences (at systolic peak) for the Newtonian and power-law fluid model.

Explicit validation of several assumptions is difficult at this point, including viscosity modeling, outlet flow splits and material model and constants of the vessel wall. If the modeling workflow is consistently used, e.g., to compare different pathological conditions, valuable results can be obtained nonetheless. Although some biological variability has been incorporated in this study by using different geometries and inlet boundary conditions, a systematic sensitivity analysis including more (modeling) parameters should be considered in future studies. In future work, also several zebrafish models of heritable

thoracic aortic disease will be compared with the presented wild-type baseline data. In addition, other cardiovascular structures such as the bulbus arteriosus will be modeled explicitly. Ongoing advances in zebrafish echocardiography and MRI will also provide more in vivo validation options.

7.5 Conclusion

In summary, we have shown that modeling the cardiovascular fluid dynamics and biomechanics in adult zebrafish is feasible. Synchrotron imaging can provide accurate three-dimensional reconstructions of the main cardiovascular structures, which is complemented by high-frequency ultrasound measurements to provide additional information on in vivo blood flow characteristics. This study provides the first reference values for multiple key biomechanical stimuli in wild-type adult zebrafish, including wall shear stress and first principal stress. The presented framework can be used for advanced cardiovascular phenotyping of adult genetically engineered zebrafish models of cardiovascular disease, showing disruptions of the normal mechanobiology and homeostasis. This way, biomechanical phenotyping in zebrafish is no longer limited to the developing stages, as earlier reported, and also progressive or late onset conditions and phenotypes can be investigated. By providing a pipeline for image-based animal-specific computational biomechanical models in zebrafish, a model organism that is increasingly used for the study of heritable cardiovascular pathophysiology, this study contributes to a more comprehensive understanding of the role of altered biomechanics and hemodynamics in cardiovascular pathologies.

7.6 Application: phenotyping a zebrafish model of aortic dissection

The work presented in 7.6 is based on the preprint:

Early mechanisms of aortic failure in a zebrafish model for thoracic aortic dissection and rupture. (Vanhooydonck, M., Verlee, M., Silva, M. S., Pottie, P., Boel, A., **Van Impe, M.**, De Saffel, H., Caboor, L., Tapaneeyaphan, P., Bonnin, A., Segers, P., De Clercq, A., Willaert, A., Syx, S., Sips, P. and Callewaert, B., bioRxiv, 2024) [12].

The results presented below are limited to those involving original contributions of this PhD thesis' author.

In smad3a-/-;smad3b-/-;smad6a-/-;smad6b-/- quadruple knockout mutant zebrafish, a novel zebrafish model for thoracic aortic dissection [12], a severe reduction of the diameter of several aortic arches is observed, resulting in asymmetric branching patterns. The fluid-structure interaction models of wild-type zebrafish, presented in this chapter, were used in a preliminary study of the principal stresses (inside the vessel wall) in the quadruple knockout zebrafish model.

All five aortic geometries and all parameter settings as described in this chapter were maintained except for the flow outlet boundary conditions at the right aortic arches II, III and IV, which was set to nearly zero (by heavily increasing the resistive boundary condition) in order to mimic the vascular organization found in these quadruple knockout mutant zebrafish.

Figure 7.12 displays both the principal stresses obtained in wild-type zebrafish (top row, note that this is a repetition of Figure 7.11) and the principal stresses obtained in simulations mimicking the quadruple knockout mutant zebrafish blood flow (bottom row, note that aortic arches II, III an IV are largely transparent in this case to indicate the nearly zero flow through these arches).

These preliminary results definitely should be interpreted cautiously, since no actual geometries nor flow profiles of SMAD quadruple knockout zebrafish were used. On the other hand, this simplified approach has the advantage that a direct and fair comparison with the earlier obtained wild type results is possible. The principal stress within the vessel wall was increased in all 5 mimicked SMAD quadruple knockout cases, especially around branching regions (Figure 7.12). Interestingly, histological and synchrotron imaging of the aorta in the SMAD quadruple knockout model show wall damage (medial elastolysis, aortic dissections and ruptures [12]) at these wall regions exposed to high biomechanical stress. Further research based on the modelling approach presented in this chapter, both including simulations with actual SMAD quadruple knockout zebrafish geometries and flow profiles and also comprising different stages (e.g., before damage and at the onset of damage), will provide a more comprehensive insight on the importance of altered hemodynamics and biomechanics in smad3a-/-;smad3b-/-;smad6a-/-;smad6b-/- quadruple knockout mutant zebrafish.

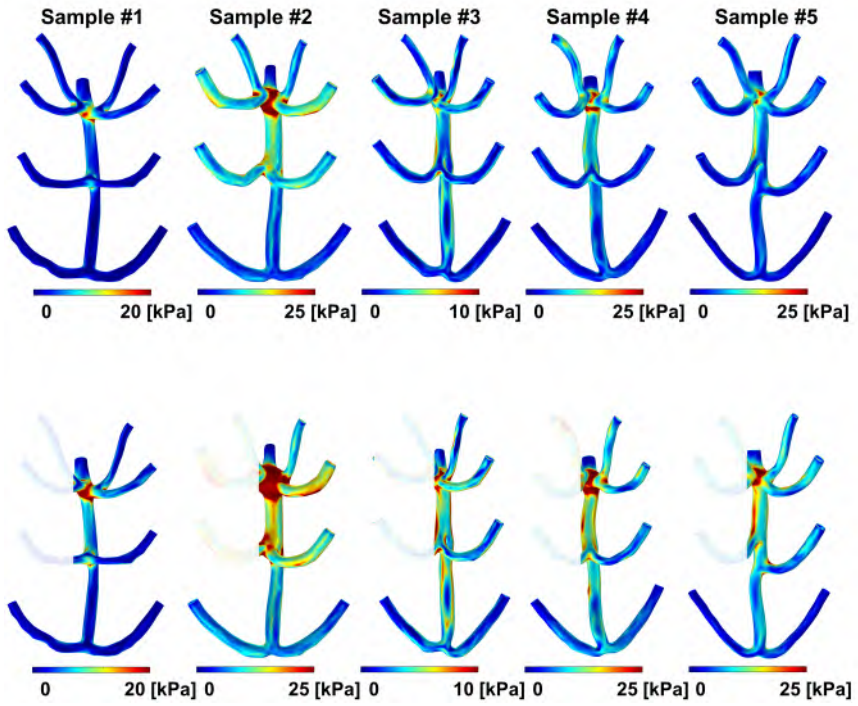

Figure 7.12: First principal stress at systolic peak in FSI baseline simulations (top row, this is identical to Figure 7.11) versus FSI simulations mimicking the flow in SMAD quadruple knock-out zebrafish.

CHAPTER 8

Biomechanics and fluid dynamics of the bulbus arteriosus in adult zebrafish: an FSI proof-of-concept

8.1 Introduction

Next to investigations of the aorta, the (patho)physiology of the bulbus arteriosus in zebrafish is interesting from a translational viewpoint, particularly for HTAD research. The position of the bulbus, directly downstream of the ventricle, is similar to the location of the aortic root in mammals, the latter providing the largest contribution to the buffering capacity of the arterial tree [212].

In zebrafish disease models of (human) pathologies associated to aortic root dilatation, abnormal function and dilatations of the bulbus were observed [13, 150].

Unfortunately, little details and experimental data on the zebrafish bulbar mechanics have been reported. In other teleost fish such as the yellowfin tuna, the behavior of the bulbus was studied experimentally [200, 202, 213]. Yellowfin tuna, compared to zebrafish, are much larger, develop much higher blood pressures and migrate over large distances (tuna are described as high-performance fish in [213])

possibly impacting their cardiovascular system and bulbus arteriosus in particular. While it is clear that a conservation of the overall cardiovascular characteristics from the yellowfin tuna to the zebrafish cannot be guaranteed, information from these reports are still used to set up the zebrafish models in this exploratory study.

Taking into account the current limitations, several options and preliminary results for biomechanical modeling of the bulbus arteriosus in adult zebrafish are reported in this chapter. For all simulations, COMSOL Multiphysics® was used. This chapter consists of two proof-of-concept (preliminary) studies (8.2.1 and 8.2.2) as well as a short overall discussion and conclusion section (8.3). Both idealized 2D axi-symmetric geometries and synchrotron imaging-based 3D geometries as well as different constitutive relations to mimic the structural behavior of the bulbar wall are considered in FSI simulations.

8.2 Proof-of-concept studies

8.2.1 2D axi-symmetric modeling

As mentioned in 2.3.2, the bulbus is pear-shaped and tapers towards the ventral aorta. The gross structure of the bulbar wall follows the classic three-layered aortic vessel structure, consisting of an intima, media and adventitia. Figure 8.1 is presented to describe the structure of the bulbar wall.

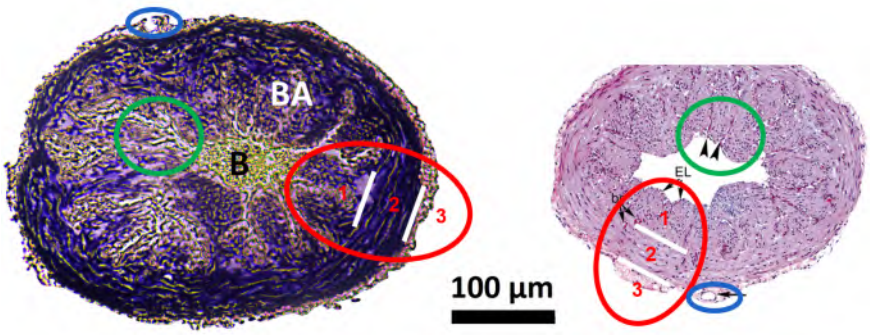

Figure 8.1: Histological cross section of the bulbus arteriosus of different zebrafish after Resorcin-fuchsine staining (left) and hematoxylin-eosin staining (right). Luminal ridges in the luminal surface and subjacent tissue are encircled in green and indicated by arrowheads, the coronary artery is encircled in blue and the three different layers of the bulbar wall are encircled in red, spaced by white bars and numbered. BA: bulbus arteriosus, B: (luminal) blood space. Images acquired at the Center for Medical Genetics Ghent (left) and adapted from [48] (right).

The ridged (or lobed) structure of the inner bulbar layer (encircled in green in Figure 8.1) is present throughout the inner circumference of the bulbus. The three different layers present in the bulbar vessel wall are encircled in red, separated by white bars, and numbered 1, 2 and 3 (counting radially from the inner to the outer layer, respectively).

The innermost layer (denoted '1' in Figure 8.1) is referred to as the intima and consists of a thin endothelial cell layer but mainly of a subendothelium with collagen, fibrils, elastic fibers and smooth muscle cells. These fibers are (predominantly) oriented longitudinally, parallel to the direction of blood flow. The middle layer (denoted '2' in Figure 8.1) is referred to as the media. The middle layer is denser compared to the inner layer and contains elastin fibers predominantly arranged circumferentially [213]. Also smooth muscle cells and collagen are present in the media (middle layer) [48]. The outermost layer (denoted '3' in Figure 8.1) is referred to as the adventitia and contains most of the collagen while limited elastin is present compared to the other layers [213].

Inspired by the above description of bulbar tissue structure, a simplified 2D axi-symmetric geometry of the bulbus was constructed for finite element modeling. In this simulation, the bulbar wall was modeled as an anisotropic hyperelastic three-layered tissue using a Holzapfel-Gasser-Ogden (HGO) material model [214]. For every hyperelastic material, the stress-strain relation can be derived from a strain energy density function, commonly denoted by W. The HGO material model models tissue as a fiber reinforced material, and the strain energy density function W can be written as:

$$W = W_{isotropic} + W_{anisotropic} \tag{8.1}$$

where $W_{isotropic}$ here is the Neo-Hookean strain energy density function as described in Chapter 7. $W_{anisotropic}$ can be written as the sum of:

$$W_4 = \frac{k_1}{2k_2}(\exp\Big(k_2(I_4 - 1)^2\Big) - 1) \tag{8.2}$$

$$W_6 = \frac{k_1}{2k_2}(\exp\Big(k_2(I_6 - 1)^2\Big) - 1) \tag{8.3}$$

where k_1 is a stress-like material parameter, k_2 is a dimensionless material parameter and I_4 and I_6 are the fourth and sixth invariants of right Cauchy-Green tensor. These invariants introduce another parameter describing the angle between the spiraling fibers.

This HGO model thus requires 4 parameter values for every different layer. Figure 8.2 visualizes (the fiber angle of) the anisotropic part of the strain energy density throughout the bulbar wall. Based on the earlier description of the (micro)structure of the bulbar wall, a longitudinal versus circumferential orientation were chosen for the inner and middle layer, respectively.

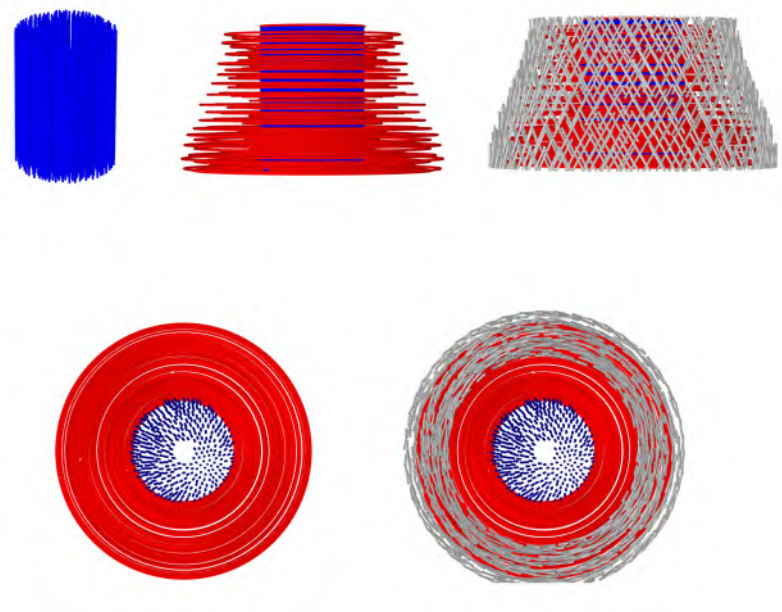

Figure 8.2: Illustration of the fiber angle of the applied HGO material model for the different layers of the bulbar wall. Top images: view from the side. Bottom images: view from the top.

An FSI simulation was conducted and the two vessel wall surfaces (consisting of three layers) perpendicular to the direction of blood flow were fully constrained. A velocity inlet (a generalize pulsed wave Doppler waveform) and pressure outlet (based on [48]) fluid boundary conditions. Later, we noticed that the timing of the applied waveforms with respect to each other does not accurately describe the physiological conditions of the bulbus. Also the (many) parameter values for the HGO model should be reconsidered in future studies since they were now unsystematically tuned in order to exhibit an r-shaped pressure-diameter relation during static inflation, as described

in [213]. Future simulations, ideally after *in vivo* measurement of bulbar pressure, outflow and luminal as well as outer wall expansion, are needed. Still, the current proof-of-concept study demonstrates that zebrafish-specific FSI modeling of the bulbus is feasible in COMSOL Multiphysics®, also for large displacements (luminal expansion), and an animation of the performed FSI simulation is provided onlineto spike the curiosity of the reader.

8.2.2 Zebrafish-specific 3D modeling

If (regularly spaced) histological sections covering the complete bulbus are available, alignment of these stacks could be performed as described in [12]. A 3D zebrafish-specific reconstruction of the bulbus is then feasible. In Figure 8.3, the transition from the bulbar wall near ventricle (left) to the aorta (right) further downstream is depicted. Note that the left image in Figure 8.3 and the left image in Figure 8.1 visualize the same histological section.

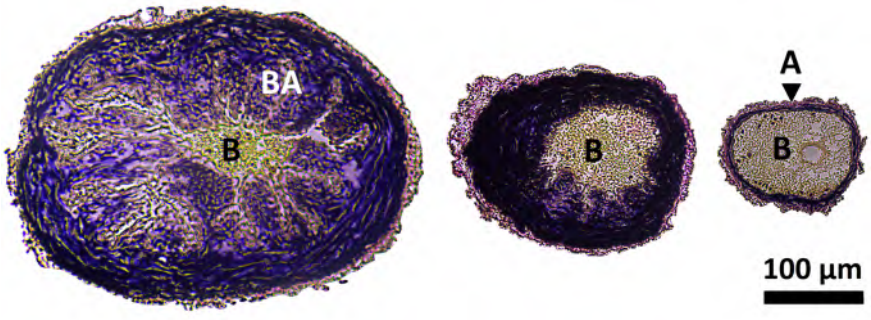

Figure 8.3: Transversal histological sections. From left to right, the transition of bulbar to aortic structure is shown. Three layers can be identified in bulbar tissue, with different (predominant) fiber orientations. The transversal spacing is 165 µm between subsequent shown sections. BA: bulbus arteriosus, B: (luminal) blood space, A: (ventral) aorta. Images acquired at the Center for Medical Genetics Ghent.

Accurate 3D zebrafish-specific reconstruction is also feasible based on synchrotron image stacks as described in Chapter 6. The synchrotron image stacks are inherently three-dimensional, the voxel size is isotropic and the bulbus was completely captured in all of our scans. Next to the segmentation of the outer tissue wall as described in Chapter 6, fast manual segmentation of both the lumen and the lobed (innermost) bulbar wall layer was feasible as depicted in Figure 8.4.

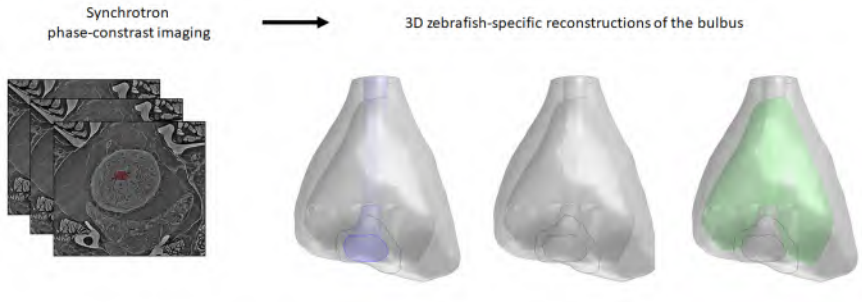

Figure 8.4: Zebrafish-specific 3D reconstruction of the bulbar wall (as a two-layered structure) as well as the blood lumen is feasible starting from synchrotron image datasets.

Accurate zebrafish-specific 3D reconstruction of all three layers of the bulbar wall is however difficult. Instead, the bulbar wall was modeled as a 2-layered structure in this case (combining the middle and outer layer).

An FSI simulation was conducted using velocity inlet and pressure outlet fluid boundary conditions. The two (wall) surfaces around the inlet and outlet were fully constrained and a stiffer material model was applied for the outer vessel layer compared to the inner layer (both layers were modeled as Neo-Hookean materials). Future simulations, ideally after *in vivo* measurement of bulbar pressure, outflow and luminal as well as outer wall expansion, are needed. Still, to spike the curiosity of the reader and to demonstrate that zebrafish-specific FSI modeling of the bulbus is feasible in COMSOL Multiphysics®, and an animation of the performed FSI simulation is provided online.

8.3 Discussion and conclusion

Rather than providing accurate simulation results at this preliminary stage, the two proof-of-constant studies presented in Subsection 8.2.1 and Subsection 8.2.2 demonstrate the feasibility of biomechanical modeling of the bulbus arteriosus but also identify (important) current limitations. More *in vivo* measurements and reports of bulbar pressure, outflow and luminal as well as outer wall bulbar expansion are needed.

A workaround to obtain a 3-layered bulbar wall structure in zebrafish-specific (synchrotron-based) geometries is assuming a constant thickness of the adventitia. The adventitia can then be obtained by eroding the outer wall. The (relatively) constant thickness of the adventitia has been reported in [213] for larger teleost fish.

HGO modeling is also possible for 3D zebrafish-specific geometries, if fiber direction is made dependent on the centerline of the lumen. Future improvements also include the use of contrast-enhanced casting to obtain a better representation of the (ridged and lobed) lumen.

Once computational solid mechanics and fluid-structure interaction models of the bulbus arteriosus have been set up using physiological (validated) fluid boundary conditions, a combined (zebrafish-specific) model of the bulbus arteriosus and ventral aorta should be considered.

In summary, this proof-of-concept study structures the first ideas to model the bulbar biomechanics and hemodynamics. Preliminary FSI animations showing, a.o., the displacement of the bulbar wall, are provided.

III

Overall discussion

Chapters

Chapter 9

Overall discussion

Each of the chapter in Part II included an individual discussion and conclusion section, which will not be repeated here. The following sections focus on this dissertation as a whole from a more general viewpoint.

9.1 Advanced imaging for cardiovascular phenotyping in adult zebrafish

Two imaging techniques have been used in this dissertation: (high-frequency) echocardiography and synchrotron (phase-contrast) micro-CT imaging.

High-frequency echocardiography provides *in vivo* functional information but can only provide limited spatial (3D) information when applied to zebrafish. Synchrotron micro-CT imaging on the other hand provides (anatomical) structural information (both in 2D and 3D) at superior spatial resolution but was applied *ex vivo*. These two techniques thus provide complementary information on the cardiovascular system of the adult zebrafish, both regarding direct cardiovascular phenotyping options and as input for (finite element) biomechanical simulations.

High-frequency echocardiography has been applied in many adult zebrafish studies focusing on cardiovascular function [150, 158, 160, 162–164, 177, 178]. In this dissertation a framework is provided to

automatically annotate and analyze a large number of pulsed wave Doppler recordings of ventricular in- or outflow. The contribution compared to the state-of-the-art is not an improvement of the ultrasound measurement (options) itself but rather a way to optimally use all information present in adult zebrafish ultrasound recordings in a fast and standardized (unbiased) manner. Furthermore, an unprecedented in-depth analysis of (correlations between) different PWD parameters was performed.

Synchrotron phase-contrast imaging was applied for the 3D reconstruction of key adult zebrafish cardiovascular macrostructures. At the same time, soft tissue microstructure information was also available from the synchrotron images. Compared to the work of Ding et al. [153] where different synchrotron modalities where examined for whole-body imaging of larval and juvenile zebrafish, we have shown that synchrotron imaging can also be applied to adult zebrafish. Our studies also identified and optimized imaging and segmentation guidelines to visualize the cardiovascular system of adult zebrafish. To segment and 3D reconstruct the (luminal) blood spaces, casting of the sample can be performed either without contrast agent and followed by a corrosion step or with a contrast agent (contrast-enhanced casting). For the ventral aorta, an accurate 3D reconstruction of the lumen could also be obtained by eroding the segmentation of the outer vessel walls. An important remark is that *ex vivo* imaging is performed and deformation of the blood lumen occurs. Injection of the casting resin *in vivo* prior to *ex vivo* imaging could allow a more physiological representation of the lumen of blood vessels.

Next to the direct use of the presented imaging frameworks for cardiovascular phenotyping in adult zebrafish, the annotated pulsed wave Doppler recording of Chapter 5 and the segmented microCT imaging datasets of Chapter 6 could also serve as reference dataset for artificial intelligence based methods regarding pulsed wave Doppler annotation and CT image segmentation in adult zebrafish.

The presented imaging frameworks for echocardiography and synchrotron microCT imaging should be seen as additions to the state-of-the art cardiovascular imaging toolbox for adult zebrafish and complement earlier described multimodal imaging modalities [150].

9.2 From imaging to biomechanical model

The biomechanical models presented in this dissertation make use of both aforementioned imaging techniques: synchrotron imaging

as input for the 3D geometry and high-frequency echocardiography providing functional information (boundary conditions). In the preliminary simulations of the bulbar biomechanics, histological data is also used to define constitutive modeling options. Synchrotron scanning still allows to use the same sample for later histological analysis. While biomechanical characterization in adult zebrafish (see below) is feasible based on the obtained imaging data, technical advancements of adult zebrafish cardiovascular imaging modalities will further improve modeling possibilities and relevance.

Taking the mouse as an example, considerable advancements have been obtained in (mouse-specific) image-based biomechanical models of the aorta during the last two decades. CFD simulations based on corrosion casts of the mouse aorta [215] evolved into in vivo micro-CT imaging to obtain more accurate (physiological) geometries [148] and the impact of different boundary conditions was investigated [208]. Subsequently, the link between hemodynamic parameters and aneurysm formation in mice was investigated with a prominent role for synchrotron imaging [216–218]. Synchrotron imaging and synchrotron-guided histology was also found especially valuable in the case of subtle (micro)defects [185, 219].

9.3 Biomechanical characterization of the cardiovascular system in adult zebrafish

Via CFD and FSI simulations, this dissertation provides the first reference values for multiple key biomechanical parameters in the ventral aorta of wild-type adult zebrafish, including wall shear stress and first principal stress. Also the first (preliminary) results on bulbar biomechanical modeling are reported.

The presented modeling framework can be used for advanced cardiovascular phenotyping of adult genetically engineered zebrafish models of cardiovascular disease where we expect to find disruptions of the normal mechano-biology and tissue homeostasis. The presented biomechanical studies provide reference values for future comparisons.

The biomechanical reports on adult zebrafish aortic biomechanics and hemodynamics in this dissertation complement other reports on biomechanics of the adult zebrafish aortic valve [220], on the embryonic biomechanics of the zebrafish heart [5–7, 87–97, 99] and on the biomechanics in the zebrafish vessel network of developing

zebrafish [85, 86, 98]. Our study therefore ensures that biomechanical phenotyping in zebrafish is no longer limited to the developing stages, enabling investigation of progressive or late onset conditions and phenotypes.

9.4 Application and clinical relevance

The next step is applying the presented advanced phenotyping options to (genetically engineered) zebrafish disease models. Examples were already provided in this dissertation, e.g., the biomechanical phenotyping of the aorta of a zebrafish smad3/smad6 quadruple knock-out model of aortic dissection. Many more applications are possible and the relevance of this dissertation is not limited to HTAD but can be expanded to investigate drug induced cardiovascular toxicities, atherosclerosis, congenital heart disease, cardiomyopathies, cardiac valves and heart regeneration.

Combined with the ease of genetic manipulation (including precision medicine) and the time- and cost-effectiveness of the zebrafish model organism, this dissertation further boosts the zebrafish as a unique first-line model in cardiovascular research, including research on the role of altered biomechanics and hemodynamics in cardiovascular pathologies.

9.5 Limitations

Validation of the modeling results presented in this dissertation is limited at this point. Many modeling inputs (e.g., boundary conditions, constitutive material models and parameter values) reflect (simplified) assumptions. Prestress in the cardiovascular tissues was not included. The very limited data on mechanical characterization of the tissues as well as blood pressure measurements also is a limiting factor. The blood as a Newtonian fluid. Several modeling results presented in Chapter 7 should therefore be seen as a baseline given the described assumptions and modeling approach, allowing future comparison with (i) similar simulations of zebrafish mutants and (ii) cardiovascular simulations in wild-type adult zebrafish based on better validated boundary conditions and modeling assumptions. The assumption to model the blood as a Newtonian fluid could also be regarded as a limitation.

Also the sample selection (including sample size, age distribution and male-female ratio) could be seen as a limiting factor, especially

in Chapter 5. More comprehensive results could be obtained by, e.g., balanced male-female ratios and age groups.

9.6 Future perspectives

Further (technical) improvement of the imaging modalities is anticipated and will enable improved biomechanical modeling in adult zebrafish as more validation options and more physiological input data will become available. Regarding high-frequency ultrasound, successors of the ultrasound machine and probes used for data recording in this dissertation are already (commercially) available (e.g., VEVO 3100 and VEVO F2 ultrasound machines compared to the used VEVO 2100 ultrasound machine). Improved ultrasound imaging of the bulbus arteriosus, both in B-mode and PWD-mode could boost image-based biomechanical modeling and 4D echocardiography of the zebrafish heart could be (re)considered.

The combination of contrast-enhanced casting and synchrotron-imaging is highly promising and could provide accurate, highly automated segmentations of the luminal blood spaces and tissue walls individually. The contrast-enhanced (ridged) lumen of the bulbus will be of special interest for improved biomechanical modeling of the bulbus arteriosus in adult zebrafish. To obtain also casts of the vasculature distal to the gills, research on resin formulation allowing to pass past the small gill capillaries is ongoing.

Reports on mechanical testing of the small zebrafish cardiovascular tissues are lacking at this point but atomic force microscopy could be considered in future studies. Additionally, improved validation of the presented computational models would be enabled by more pressure measurements (limited information is presented in [48]) and improved ultrasound recordings, and both of these options are viewed as realistic in the near/immediate future. A combined fluid-structure interaction model of the bulbus arteriosus and ventral aorta can then be considered.

Next to these technical perspectives, direct application of the imaging and modeling frameworks to phenotype several zebrafish models of cardiovascular disease (as already described in 9.4) form an (at least equally) important future perspective.

9.7 Take home message

Both embryonic and adult zebrafish can be considered as a valuable model in cardiovascular research, not only in, e.g., biology or biomedical sciences but also for biomedical engineering and biomechanical research. This dissertation demonstrates that biomedical engineering can enable novel cardiovascular phenotyping options in adult zebrafish such as zebrafish-specific numerical simulations of aortic biomechanics and hemodynamics. Zebrafish, a versatile, cost-effective and genetically very interesting animal model, can effectively contribute to a comprehensive understanding of the role of cardiovascular biomechanics in (patho)physiological mechanobiology. By improving the battery of cardiovascular phenotyping tools in zebrafish as presented in this dissertation, a more comprehensive and biomechanical characterization of zebrafish disease models is feasible, which may ultimately facilitate the translation from preclinical research to clinical application.

Bibliography

[1] Jay D. Humphrey and Martin A. Schwartz. Vascular Mechanobiology: Homeostasis, Adaptation, and Disease, 2021.

[2] J. D. Humphrey. Continuum biomechanics of soft biological tissues, jan 2003.

[3] G. Martufi, T. C. Gasser, J. J. Appoo, and E. S. Di Martino. Mechano-biology in the thoracic aortic aneurysm: a review and case study, 2014.

[4] Jay D. Humphrey, Martin A. Schwartz, George Tellides, and Dianna M. Milewicz. Role of mechanotransduction in vascular biology: Focus on thoracic aortic aneurysms and dissections, 2015.

[5] Vijay Vedula, Juhyun Lee, Hao Xu, C.-C. Jay Kuo, Tzung K. Hsiai, and Alison L. Marsden. A method to quantify mechanobiologic forces during zebrafish cardiac development using 4-D light sheet imaging and computational modeling. *PLOS Computational Biology*, 13(10):e1005828, oct 2017.

[6] Yoke Yin Foo, Shilpa Pant, Huiping Shermaine Tay, Nurgul Imangali, Nanguang Chen, Christoph Winkler, and Choon Hwai Yap. 4D modelling of fluid mechanics in the zebrafish embryonic heart. *Biomechanics and Modeling in Mechanobiology*, 19(1):221–232, 2020.

[7] Adriana Gaia Cairelli, Renee Wei Yan Chow, Julien Vermot, and Choon Hwai Yap. Fluid mechanics of the zebrafish embryonic heart trabeculation. *PLoS Computational Biology*, 18(6):1–17, 2022.

[8] Matthias Van Impe, Lisa Caboor, Violette Deleeuw, Margie Olbinado, Julie De Backer, Patrick Sips, and Patrick Segers.

Fluid-Structure Interaction Modeling of the Aortic Hemodynamics in Adult Zebrafish: A Pilot Study Based on Synchrotron X-Ray Tomography. *IEEE Transactions on Biomedical Engineering*, 70(7):2101–2110, 2023.

[9] Matthias Van Impe, Lisa Caboor, Violette Deleeuw, Karo De Rycke, Michiel Vanhooydonck, Julie De Backer, Patrick Segers, and Patrick Sips. Application of an automated analysis framework for pulsed-wave Doppler cardiac ultrasound measurements to generate reference data in adult zebrafish. *American Journal of Physiology - Regulatory Integrative and Comparative Physiology*, 325(6):R782–R796, 2023.

[10] Ward De Spiegelaere, Lisa Caboor, Matthias Van Impe, Matthieu N. Boone, Julie De Backer, Patrick Segers, and Patrick Sips. Corrosion casting of the cardiovascular structure in adult zebrafish for analysis by scanning electron microscopy and X-ray microtomography. *Journal of Veterinary Medicine Series C: Anatomia Histologia Embryologia*, 49(5):635–642, 2020.

[11] Eline Goossens, Loren Deblock, Lisa Caboor, Dietger Van den Eynden, Iván Josipovic, Pablo Reyes Isaacura, Elizaveta Maksimova, Matthias Van Impe, Anne Bonnin, Patrick Segers, Pieter Cornillie, Matthieu N. Boone, Isabel Van Driessche, Ward De Spiegelaere, Jonathan De Roo, Patrick Sips, and Klaartje De Buysser. From Corrosion Casting to Virtual Dissection: Contrast-Enhanced Vascular Imaging using Hafnium Oxide Nanocrystals. *Small Methods*, 2301499:1–15, 2024.

[12] Michiel Vanhooydonck, Maxim Verlee, Marta Santana Silva, Annekatrien Boel, Matthias Van Impe, Hanna De Saffel, Lisa Caboor, Piyanoot Tapaneeyaphan, Anne Bonnin, Adelbert De Clercq, Andy Willaert, Delfien Syx, Patrick Sips, and Bert Callewaert. Early mechanisms of aortic failure in a zebrafish model for thoracic aortic dissection and rupture. *bioRxiv*, 2024.

[13] Karo De Rycke, Marina Horvat, Lisa Caboor, Petra Vermassen, Griet De Smet, Marta Santana Silva, Wouter Steyaert, Matthias Van Impe, Patrick Segers, Julie De Backer, and Patrick Sips. Systematic disruption of zebrafish fibrillin genes identifies a translational zebrafish model for Marfan syndrome. 2025.

[14] Mihaly Szabo, Sara Svensson Akusjärvi, Ankur Saxena, Jianping Liu, Gayathri Chandrasekar, and Satish S. Kitambi. Cell and small animal models for phenotypic drug discovery, 2017.

[15] Vijay K. Singh and Thomas M. Seed. How necessary are animal models for modern drug discovery?, 2021.

[16] N. Bryce Robinson, Katherine Krieger, Faiza Khan, William Huffman, Michelle Chang, Ajita Naik, Ruan Yongle, Irbaz Hameed, Karl Krieger, Leonard N. Girardi, and Mario Gaudino. The current state of animal models in research: A review. *International Journal of Surgery*, 72, 2019.

[17] P. Mukherjee, S. Roy, D. Ghosh, and S. K. Nandi. Role of animal models in biomedical research: a review, 2022.

[18] Graham J. Lieschke and Peter D. Currie. Animal models of human disease: Zebrafish swim into view. *Nature Reviews Genetics*, 8:353–367, 2007.

[19] Yusuf Bozkurt. *Recent Advances in Zebrafish Researches*. 2018.

[20] Tsegay Teame, Zhen Zhang, Chao Ran, Hongling Zhang, Yalin Yang, Qianwen Ding, Minxu Xie, Chenchen Gao, Yongan Ye, Ming Duan, and Zhigang Zhou. The use of zebrafish (Danio rerio) as biomedical models. *Animal Frontiers*, 9(3), 2019.

[21] Tae Young Choi, Tae Ik Choi, Yu Ri Lee, Seong Kyu Choe, and Cheol Hee Kim. Zebrafish as an animal model for biomedical research, 2021.

[22] Kerstin Howe, Matthew D. Clark, Carlos F. Torroja, James Torrance, Camille Berthelot, Matthieu Muffato, John E. Collins, Sean Humphray, Karen McLaren, Lucy Matthews, Stuart McLaren, Ian Sealy, Mario Caccamo, Carol Churcher, Carol Scott, Jeffrey C. Barrett, Romke Koch, Gerd Jörg Rauch, Simon White, William Chow, Britt Kilian, Leonor T. Quintais, José A. Guerra-Assunção, Yi Zhou, Yong Gu, Jennifer Yen, Jan Hinnerk Vogel, Tina Eyre, Seth Redmond, Ruby Banerjee, Jianxiang Chi, Beiyuan Fu, Elizabeth Langley, Sean F. Maguire, Gavin K. Laird, David Lloyd, Emma Kenyon, Sarah Donaldson, Harminder Sehra, Jeff Almeida-King, Jane Loveland, Stephen Trevanion, Matt Jones, Mike Quail, Dave Willey, Adrienne Hunt, John Burton, Sarah Sims, Kirsten McLay, Bob Plumb, Joy Davis, Chris Clee, Karen Oliver, Richard Clark, Clare Riddle, David Eliott, Glen Threadgold, Glenn Harden, Darren Ware, Beverly Mortimer, Giselle Kerry, Paul Heath, Benjamin Phillimore, Alan Tracey, Nicole Corby, Matthew

Dunn, Christopher Johnson, Jonathan Wood, Susan Clark, Sarah Pelan, Guy Griffiths, Michelle Smith, Rebecca Glithero, Philip Howden, Nicholas Barker, Christopher Stevens, Joanna Harley, Karen Holt, Georgios Panagiotidis, Jamieson Lovell, Helen Beasley, Carl Henderson, Daria Gordon, Katherine Auger, Deborah Wright, Joanna Collins, Claire Raisen, Lauren Dyer, Kenric Leung, Lauren Robertson, Kirsty Ambridge, Daniel Leongamornlert, Sarah McGuire, Ruth Gilderthorp, Coline Griffiths, Deepa Manthravadi, Sarah Nichol, Gary Barker, Siobhan Whitehead, Michael Kay, Jacqueline Brown, Clare Murnane, Emma Gray, Matthew Humphries, Neil Sycamore, Darren Barker, David Saunders, Justene Wallis, Anne Babbage, Sian Hammond, Maryam Mashreghi-Mohammadi, Lucy Barr, Sancha Martin, Paul Wray, Andrew Ellington, Nicholas Matthews, Matthew Ellwood, Rebecca Woodmansey, Graham Clark, James Cooper, Anthony Tromans, Darren Grafham, Carl Skuce, Richard Pandian, Robert Andrews, Elliot Harrison, Andrew Kimberley, Jane Garnett, Nigel Fosker, Rebekah Hall, Patrick Garner, Daniel Kelly, Christine Bird, Sophie Palmer, Ines Gehring, Andrea Berger, Christopher M. Dooley, Zübeyde Ersan-Ürün, Cigdem Eser, Horst Geiger, Maria Geisler, Lena Karotki, Anette Kirn, Judith Konantz, Martina Konantz, Martina Oberländer, Silke Rudolph-Geiger, Mathias Teucke, Kazutoyo Osoegawa, Baoli Zhu, Amanda Rapp, Sara Widaa, Cordelia Langford, Fengtang Yang, Nigel P. Carter, Jennifer Harrow, Zemin Ning, Javier Herrero, Steve M.J. Searle, Anton Enright, Robert Geisler, Ronald H.A. Plasterk, Charles Lee, Monte Westerfield, Pieter J. De Jong, Leonard I. Zon, John H. Postlethwait, Christiane Nüsslein-Volhard, Tim J.P. Hubbard, Hugues Roest Crollius, Jane Rogers, and Derek L. Stemple. The zebrafish reference genome sequence and its relationship to the human genome. *Nature*, 2013.

[23] Allan V. Kalueff, David J. Echevarria, and Adam Michael Stewart. Gaining translational momentum: More zebrafish models for neuroscience research, 2014.

[24] Adam Michael Stewart, Oliver Braubach, Jan Spitsbergen, Robert Gerlai, and Allan V. Kalueff. Zebrafish models for translational neuroscience research: From tank to bedside, 2014.

[25] Chie Satou, Rachael L. Neve, Hassana K. Oyibo, Pawel Zmarz, Kuo Hua Huang, Estelle Arn Bouldoires, Takuma

Mori, Shin Ichi Higashijima, Georg B. Keller, and Rainer W. Friedrich. A viral toolbox for conditional and transneuronal gene expression in zebrafish. *eLife*, 11, 2022.

[26] Marina C. Mione and Nikolaus S. Trede. The zebrafish as a model for cancer, 2010.

[27] Martina Hason and Petr Bartůněk. Zebrafish models of cancer-new insights on modeling human cancer in a non-mammalian vertebrate, 2019.

[28] Muhammad Abdul Rouf, Lin Wen, Yoga Mahendra, Jinxuan Wang, Kun Zhang, Shuang Liang, Yuming Wang, Zhenggong Li, Yeqi Wang, and Guixue Wang. The recent advances and future perspectives of genetic compensation studies in the zebrafish model, 2023.

[29] Lucie Crouzier, Elodie M. Richard, Jo Sourbron, Lieven Lagae, Tangui Maurice, and Benjamin Delprat. Use of zebrafish models to boost research in rare genetic diseases, 2021.

[30] Federico Tessadori, Helen I. Roessler, Sanne M.C. Savelberg, Sonja Chocron, Sarah M. Kamel, Karen J. Duran, Mieke M. Van Haelst, Gijs Van Haaften, and Jeroen Bakkers. Effective CRISPR/Cas9-based nucleotide editing in zebrafish to model human genetic cardiovascular disorders. *DMM Disease Models and Mechanisms*, 11(10), 2018.

[31] Satoshi Ota and Atsuo Kawahara. Zebrafish: A model vertebrate suitable for the analysis of human genetic disorders, 2014.

[32] Anne S. Glass and Ralf Dahm. The zebrafish as a model organism for eye development. *Ophthalmic Research*, 36(1), 2004.

[33] Anastasia Dimitriadi and George Koumoundouros. Elevated Embryonic Temperature Has Persistent Adverse Effects on Zebrafish Swimming Capacity. *Fishes*, 7(6), 2022.

[34] Woong Y. Hwang, Yanfang Fu, Deepak Reyon, Morgan L. Maeder, Shengdar Q. Tsai, Jeffry D. Sander, Randall T. Peterson, J. R.Joanna Yeh, and J. Keith Joung. Efficient genome editing in zebrafish using a CRISPR-Cas system. *Nature Biotechnology*, 31(3):227–229, 2013.

[35] Paige R. Takasugi, Shengzhou Wang, Kimberly T. Truong, Evan P. Drage, Sahar N. Kanishka, Marissa A. Higbee, Nathan Bamidele, Ogooluwa Ojelabi, Erik J. Sontheimer, and James A. Gagnon. Orthogonal CRISPR-Cas tools for genome editing, inhibition, and CRISPR recording in zebrafish embryos. *Genetics*, 220(1), 2022.

[36] Philipp J. Keller, Annette D. Schmidt, Joachim Wittbrodt, and Ernst H.K. Stelzer. Reconstruction of Zebrafish Early Embryonic Development by Scanned Light Sheet Microscopy. *Science*, 322(5904):1065–1069, nov 2008.

[37] Philipp J. Keller. In vivo imaging of zebrafish embryogenesis. *Methods*, 62(3), 2013.

[38] Leonard I. Zon and Randall T. Peterson. In vivo drug discovery in the zebrafish, 2005.

[39] T. P. Barros, W. K. Alderton, H. M. Reynolds, A. G. Roach, and S. Berghmans. Zebrafish: An emerging technology for in vivo pharmacological assessment to identify potential safety liabilities in early drug discovery, 2008.

[40] Calum A. MacRae and Randall T. Peterson. Zebrafish as tools for drug discovery. *Nature Reviews Drug Discovery*, 14(10):721–731, 2015.

[41] Uwe Strähle, Stefan Scholz, Robert Geisler, Petra Greiner, Henner Hollert, Sepand Rastegar, Axel Schumacher, Ingrid Selderslaghs, Carsten Weiss, Hilda Witters, and Thomas Braunbeck. Zebrafish embryos as an alternative to animal experiments-A commentary on the definition of the onset of protected life stages in animal welfare regulations. *Reproductive Toxicology*, 33(2), 2012.

[42] Lynne U. Sneddon, Lewis G. Halsey, and Nic R. Bury. Considering aspects of the 3Rs principles within experimental animal biology, 2017.

[43] Keke Wang, Xiangguang Meng, and Zhikun Guo. Elastin Structure, Synthesis, Regulatory Mechanism and Relationship With Cardiovascular Diseases, 2021.

[44] Markella Ponticos and Barbara D. Smith. Extracellular matrix synthesis in vascular disease: Hypertension, and atherosclerosis. *Journal of Biomedical Research*, 28(1), 2014.

[45] Xunjie Yu, Raphaël Turcotte, Francesca Seta, and Yanhang Zhang. Micromechanics of elastic lamellae: Unravelling the role of structural inhomogeneity in multi-scale arterial mechanics. *Journal of the Royal Society Interface*, 15(147), 2018.

[46] E. N. Marieb and K. Hoehn. *Anatomy and physiology*. Pearson Education Inc., 2011.

[47] Friedrich Heinrich Martini. *Fundamentals of Anatomy and Physiology*. Benjamin Cummings, Pearson education, 2006.

[48] Norman Hu, H. Joseph Yost, and Edward B. Clark. Cardiac morphology and blood pressure in the adult zebrafish. *The Anatomical Record*, 264(1):1–12, sep 2001.

[49] Marie Hoareau, Naïma El Kholti, Romain Debret, and Elise Lambert. Zebrafish as a Model to Study Vascular Elastic Fibers and Associated Pathologies. *International Journal of Molecular Sciences*, 23(4), 2022.

[50] Olaf Fritze, Beatriz Romero, Martina Schleicher, Marie Paule Jacob, Djin Ye Oh, Barry Starcher, Katja Schenke-Layland, Julia Bujan, and Ulrich A. Stock. Age-related changes in the elastic tissue of the human aorta. *Journal of Vascular Research*, 49(1), 2011.

[51] Joseph M. Miano, Mary A. Georger, Adam Rich, and Karen L. De Mesy Bentley. Ultrastructure of zebrafish dorsal aortic cells. *Zebrafish*, 3(4), 2006.

[52] James C. Russell and Spencer D. Proctor. Small animal models of cardiovascular disease: tools for the study of the roles of metabolic syndrome, dyslipidemia, and atherosclerosis, 2006.

[53] Jesus Egido, Carlos Zaragoza, Carmen Gomez-Guerrero, Jose Luis Martin-Ventura, Luis Blanco-Colio, Begoa Lavin, Beat Mallavia, Carlos Tarin, Sebastian Mas, and Alberto Ortiz. Animal models of cardiovascular diseases, 2011.

[54] H. G. Tsang, N. A. Rashdan, C. B.A. Whitelaw, B. M. Corcoran, K. M. Summers, and V. E. MacRae. Large animal models of cardiovascular disease. *Cell Biochemistry and Function*, 34(3), 2016.

[55] Timothy J.A. Chico, Philip W. Ingham, and David C. Crossman. Modeling cardiovascular disease in the zebrafish. *Trends in Cardiovascular Medicine*, 18(4):150–155, 2008.

[56] Catherine T. Nguyen, Qing Lu, Yibin Wang, and Jau Nian Chen. Zebrafish as a model for cardiovascular development and disease, 2008.

[57] Jeroen Bakkers. Zebrafish as a model to study cardiac development and human cardiac disease. *Cardiovascular Research*, 91(2):279–288, jul 2011.

[58] Kar Lai Poon and Thomas Brand. The zebrafish model system in cardiovascular research: A tiny fish with mighty prospects. *Global Cardiology Science and Practice*, 2013(1):4, 2013.

[59] Aarti Asnani and Randall T. Peterson. The zebrafish as a tool to identify novel therapies for human cardiovascular disease. *Disease Models & Mechanisms*, 7(7):763–767, 2014.

[60] Christine E. Genge, Eric Lin, Ling Lee, Xiao Ye Sheng, Kaveh Rayani, Marvin Gunawan, Charles M. Stevens, Alison Yueh Li, Sanam Shafaat Talab, Thomas W. Claydon, Leif Hove-Madsen, and Glen F. Tibbits. The zebrafish heart as a model of mammalian cardiac function, 2016.

[61] Despina Bournele and Dimitris Beis. Zebrafish models of cardiovascular disease. *Heart Failure Reviews*, 2016.

[62] Philipp Gut, Sven Reischauer, Didier Y. R. Stainier, and Rima Arnaout. Little Fish, Big Data: Zebrafish as a Model for Cardiovascular and Metabolic Disease. *Physiological Reviews*, 97(3):889–938, jul 2017.

[63] Matthew R. Stoyek and T. Alexander Quinn. One fish, two fish, red fish, blue fish*: Zebrafish as a model for cardiac research. *Progress in Biophysics and Molecular Biology*, 138:1–2, oct 2018.

[64] Panagiota Giardoglou and Dimitris Beis. On Zebrafish disease models and matters of the heart. *Biomedicines*, 7(1):15, feb 2019.

[65] George Bowley, Elizabeth Kugler, Rob Wilkinson, Allan Lawrie, Freek Eeden, Tim J. A. Chico, Paul C. Evans, Emily S. Noël, and Jovana Serbanovic-Canic. Zebrafish as a tractable model of human cardiovascular disease. *British Journal of Pharmacology*, 179(5):900–917, mar 2022.

[66] Juan Manuel González-Rosa. Zebrafish Models of Cardiac Disease: From Fortuitous Mutants to Precision Medicine, 2022.

[67] Didier Y.R. Stainier and Mark C. Fishman. Patterning the zebrafish heart tube: Acquisition of anteroposterior polarity. *Developmental Biology*, 153(1), 1992.

[68] D. Y.R. Stainier, R. K. Lee, and M. C. Fishman. Cardiovascular development in the zebrafish: I. Myocardial fate map and heart tube formation. *Development*, 1993.

[69] Charles B. Kimmel, William W. Ballard, Seth R. Kimmel, Bonnie Ullmann, and Thomas F. Schilling. Stages of embryonic development of the zebrafish. *Developmental Dynamics*, 203(3):253–310, jul 1995.

[70] D.Y. Stainier, Bernadette Fouquet, J.N. Chen, K.S. Warren, B.M. Weinstein, S.E. Meiler, M.A. Mohideen, S.C. Neuhauss, Liliana Solnica-Krezel, A.F. Schier, Fried Zwartkruis, D.L. Stemple, Jarema Malicki, Wolfgang Driever, and M.C. Fishman. Mutations affecting the formation and function of the cardiovascular system in the zebrafish embryo. *Development*, 123(1):285–292, dec 1996.

[71] Jau Nian Chen, Pascal Haffter, Jörg Odenthal, Elisabeth Vogelsang, Michael Brand, Fredericus J.M. Van Eeden, Makoto Furutani-Seiki, Michael Granato, Matthias Hammerschmidt, Carl Philipp Heisenberg, Yun Jin Jiang, Donald A. Kane, Robert N. Kelsh, Mary C. Mullins, and Christiane Nüsslein-Volhard. Mutations affecting the cardiovascular system and other internal organs in zebrafish. *Development*, 123, 1996.

[72] Brant M. Weinstein, Derek L. Stemple, Wolfgang Driever, and Mark C. Fishman. Gridlock, a localized heritable vascular patterning defect in the zebrafish. *Nature Medicine*, 1(11):1143–1147, nov 1995.

[73] Brant M. Weinstein, Alexander F. Schier, Salim Abdelilah, Jarema Malicki, Lilliana Solnica-Krezel, Derek L. Stemple, Didier Y.R. Stainier, Fried Zwartkruis, Wolfgang Driever, and Mark C. Fishman. Hematopoietic mutations in the zebrafish. *Development*, 123, 1996.

[74] Michael Weber and Jan Huisken. In vivo imaging of cardiac development and function in zebrafish using light sheet microscopy. *Swiss Medical Weekly*, 145(December):1–13, 2015.

[75] Shu Tu and Neil C. Chi. Zebrafish models in cardiac development and congenital heart birth defects. *Differentiation*, 84(1), 2012.

[76] Dixuan Yang, Zhenjie Jian, Changfa Tang, Zhanglin Chen, Zuoqiong Zhou, Lan Zheng, and Xiyang Peng. Zebrafish Congenital Heart Disease Models: Opportunities and Challenges. *International Journal of Molecular Sciences*, 25(11), 2024.

[77] Yan Shi, Yongqing Li, Yuequn Wang, Ping Zhu, Yu Chen, Heng Wang, Shusheng Yue, Xiaohui Xia, Jimei Chen, Zhigang Jiang, Chengbin Zhou, Wanwan Cai, Haiyun Yuan, Yueheng Wu, Yongqi Wan, Xiaohong Li, Xiaolan Zhu, Zuoqiong Zhou, Guo Dai, Fang Li, Xiaoyang Mo, Xiangli Ye, Xiongwei Fan, Jian Zhuang, Xiushan Wu, and Wuzhou Yuan. BVES downregulation in non-syndromic tetralogy of fallot is associated with ventricular outflow tract stenosis. *Scientific Reports*, 10(1), 2020.

[78] Kelly A. Smith, Sonja Chocron, Sophia von der Hardt, Emma de Pater, Alexander Soufan, Jeroen Bussmann, Stefan Schulte-Merker, Matthias Hammerschmidt, and Jeroen Bakkers. Rotation and Asymmetric Development of the Zebrafish Heart Requires Directed Migration of Cardiac Progenitor Cells. *Developmental Cell*, 14(2), 2008.

[79] Julien Vermot, Arian S. Forouhar, Michael Liebling, David Wu, Diane Plummer, Morteza Gharib, and Scott E. Fraser. Reversing blood flows act through klf2a to ensure normal valvulogenesis in the developing heart. *PLoS Biology*, 7(11), 2009.

[80] Emily Steed, Nathalie Faggianelli, Stéphane Roth, Caroline Ramspacher, Jean Paul Concordet, and Julien Vermot. Klf2a couples mechanotransduction and zebrafish valve morphogenesis through fibronectin synthesis. *Nature Communications*, 7, 2016.

[81] Chen Cai, Caijun Sang, Juan Du, Haibo Jia, Jiayi Tu, Qing Wan, Binghao Bao, Shanglun Xie, Ying Huang, Ao Li, Jiayu Li, Kun Yang, Song Wang, and Qunwei Lu. Knockout of tnni1b in zebrafish causes defects in atrioventricular valve development via the inhibition of the myocardial wnt signaling pathway. *FASEB Journal*, 33(1), 2019.

[82] Felix Gunawan, Alessandra Gentile, Sébastien Gauvrit, Didier Y.R. Stainier, and Anabela Bensimon-Brito. Nfatc1 Promotes Interstitial Cell Formation During Cardiac Valve Development in Zebrafish. *Circulation Research*, 126(8), 2020.

[83] Thomas Juan, Agatha Ribeiro da Silva, Bárbara Cardoso, So Eun Lim, Violette Charteau, and Didier Y.R. Stainier. Multiple pkd and piezo gene family members are required for atrioventricular valve formation. *Nature Communications*, 14(1):1–12, 2023.

[84] Dandan Tang, Fang Geng, Chunxiao Yu, and Ruilin Zhang. Recent Application of Zebrafish Models in Atherosclerosis Research. *Frontiers in Cell and Developmental Biology*, 9, 2021.

[85] Sang Joon Lee, Woorak Choi, Eunseok Seo, and Eunseop Yeom. Association of early atherosclerosis with vascular wall shear stress in hypercholesterolemic zebrafish. *PLoS ONE*, 10(11), 2015.

[86] Woorak Choi, Hye Mi Kim, Sungho Park, Eunseop Yeom, Junsang Doh, and Sang Joon Lee. Variation in wall shear stress in channel networks of zebrafish models. *Journal of the Royal Society Interface*, 14(127), 2017.

[87] Juhyun Lee, Mahdi Esmaily Moghadam, Ethan Kung, Hung Cao, Tyler Beebe, Yury Miller, Beth L. Roman, Ching-Ling Lien, Neil C. Chi, Alison L. Marsden, and Tzung K. Hsiai. Moving Domain Computational Fluid Dynamics to Interface with an Embryonic Model of Cardiac Morphogenesis. *PLoS ONE*, 8(8):e72924, aug 2013.

[88] Francesco Boselli and Julien Vermot. Live imaging and modeling for shear stress quantification in the embryonic zebrafish heart. *Methods*, 94:129–134, feb 2016.

[89] Francesco Boselli, Emily Steed, Jonathan B. Freund, and Julien Vermot. Anisotropic shear stress patterns predict the orientation of convergent tissue movements in the embryonic heart. *Development*, 144(23):4322–4327, dec 2017.

[90] Huseyin C. Yalcin, Armin Amindari, Jonathan T. Butcher, Asma Althani, and Magdi Yacoub. Heart function and hemodynamic analysis for zebrafish embryos. *Developmental Dynamics*, 246(11):868–880, nov 2017.

[91] Juhyun Lee, Vijay Vedula, Kyung In Baek, Junjie Chen, Jeffrey J. Hsu, Yichen Ding, Chih Chiang Chang, Hanul Kang, Adam Small, Peng Fei, Cheng Ming Chuong, Rongsong Li, Linda Demer, René R.Sevag Packard, Alison L. Marsden, and Tzung K. Hsiai. Spatial and temporal variations in hemodynamic forces initiate cardiac trabeculation. *JCI insight*, 3(13), 2018.

[92] N. A. Battista, A. N. Lane, J. Liu, and L. A. Miller. Fluid dynamics in heart development: Effects of hematocrit and trabeculation. *Mathematical Medicine and Biology*, 35(4):493–516, 2018.

[93] Nicholas Battista, Dylan Douglas, Andrea Lane, Leigh Samsa, Jiandong Liu, and Laura Miller. Vortex Dynamics in Trabeculated Embryonic Ventricles. *Journal of Cardiovascular Development and Disease*, 6(1):6, jan 2019.

[94] Huseyin Enes Salman and Huseyin Cagatay Yalcin. Advanced blood flow assessment in Zebrafish via experimental digital particle image velocimetry and computational fluid dynamics modeling. *Micron*, 130(December 2019), 2020.

[95] Huseyin Enes Salman and Huseyin Cagatay Yalcin. Computational Modeling of Blood Flow Hemodynamics for Biomechanical Investigation of Cardiac Development and Disease. *Journal of Cardiovascular Development and Disease*, 8(2):14, jan 2021.

[96] Alireza Sharifi, Alex Gendernalik, Deborah Garrity, and David Bark. Valveless pumping behavior of the simulated embryonic heart tube as a function of contractile patterns and myocardial stiffness. *Biomechanics and Modeling in Mechanobiology*, 20(5):2001–2012, 2021.

[97] Yoke Yin Foo, Efthymios Motakis, Zenia Tiang, Shuhao Shen, Jason Kuan Han Lai, Wei Xuan Chan, Hadi Wiputra, Nanguang Chen, Ching Kit Chen, Christoph Winkler, Roger Sik Yin Foo, and Choon Hwai Yap. Effects of extended pharmacological disruption of zebrafish embryonic heart biomechanical environment on cardiac function, morphology, and gene expression. *Developmental Dynamics*, 250(12):1759–1777, dec 2021.

[98] Kyung In Baek, Shyr Shea Chang, Chih Chiang Chang, Mehrdad Roustaei, Yichen Ding, Yixuan Wang, Justin Chen, Ryan O'Donnell, Hong Chen, Julianne W. Ashby, Xiaolei Xu, Julia J. Mack, Susana Cavallero, Marcus Roper, and Tzung K. Hsiai. Vascular Injury in the Zebrafish Tail Modulates Blood Flow and Peak Wall Shear Stress to Restore Embryonic Circular Network. *Frontiers in Cardiovascular Medicine*, 9(March):1–18, 2022.

[99] Adriana Gaia Cairelli, Alex Gendernalik, Wei Xuan Chan, Phuc Nguyen, Julien Vermot, Juhyun Lee, David Bark, and Choon Hwai Yap. Role of tissue biomechanics in the formation and function of myocardial trabeculae in zebrafish embryos. *Journal of Physiology*, 602(4), 2024.

[100] Aaron Kithcart and Calum A. MacRae. Using Zebrafish for High-Throughput Screening of Novel Cardiovascular Drugs. *JACC: Basic to Translational Science*, 2(1):1–12, 2017.

[101] Yanbin Zhao, Kun Zhang, Patrick Sips, and Calum A. MacRae. Screening drugs for myocardial disease in vivo with zebrafish: an expert update. *Expert Opinion on Drug Discovery*, 14(4):343–353, 2019.

[102] Leyre Echeazarra, Maria Pura Hortigón-Vinagre, Oscar Casis, and Mónica Gallego. Adult and Developing Zebrafish as Suitable Models for Cardiac Electrophysiology and Pathology in Research and Industry, 2021.

[103] David J. Milan, Ian L. Jones, Patrick T. Ellinor, and Calum A. MacRae. In vivo recording of adult zebrafish electrocardiogram and assessment of drug-induced QT prolongation. *American Journal of Physiology - Heart and Circulatory Physiology*, 291(1):269–273, 2006.

[104] Renate Kopp, Thorsten Schwerte, and Bernd Pelster. Cardiac performance in the zebrafish breakdance mutant. *Journal of Experimental Biology*, 208(11), 2005.

[105] David J. Milan and Calum A. MacRae. Zebrafish genetic models for arrhythmia. *Progress in Biophysics and Molecular Biology*, 98(2-3):301–308, 2008.

[106] Jordan T. Shin, Eugene V. Pomerantsev, John D. Mably, and Calum A. MacRae. High-resolution cardiovascular function confirms functional orthology of myocardial contractility pathways in zebrafish. *Physiological Genomics*, 42(2):300–309, 2010.

[107] Kenneth D. Poss, Lindsay G. Wilson, and Mark T. Keating. Heart Regeneration in Zebrafish. *Science*, 298(5601):2188–2190, dec 2002.

[108] Chris Jopling, Eduard Sleep, Marina Raya, Mercè Martí, Angel Raya, and Juan Carlos Izpisa Belmonte. Zebrafish heart regeneration occurs by cardiomyocyte dedifferentiation and proliferation. *Nature*, 464(7288), 2010.

[109] Kyung In Baek, Yichen Ding, Chih Chiang Chang, Megan Chang, René R. Sevag Packard, Jeffrey J. Hsu, Peng Fei, and Tzung K. Hsiai. Advanced microscopy to elucidate cardiovascular injury and regeneration: 4D light-sheet imaging, 2018.

[110] Anabela Bensimon-Brito, Srinath Ramkumar, Giulia L.M. Boezio, Stefan Guenther, Carsten Kuenne, Christian S.M. Helker, Héctor Sánchez-Iranzo, Dijana Iloska, Janett Piesker, Soni Pullamsetti, Nadia Mercader, Dimitris Beis, and Didier Y.R. Stainier. TGF-β Signaling Promotes Tissue Formation during Cardiac Valve Regeneration in Adult Zebrafish. *Developmental Cell*, 52(1):9–20.e7, 2020.

[111] Yonghe Ding, Xiaojing Sun, Wei Huang, Tiffany Hoage, Margaret Redfield, Sudhir Kushwaha, Sridhar Sivasubbu, Xueying Lin, Stephen Ekker, and Xiaolei Xu. Haploinsufficiency of target of rapamycin attenuates cardiomyopathies in adult zebrafish. *Circulation Research*, 109(6), 2011.

[112] Peng Fei, Juhyun Lee, René R. Sevag Packard, Konstantina-Ioanna Sereti, Hao Xu, Jianguo Ma, Yichen Ding, Hanul Kang, Harrison Chen, Kevin Sung, Rajan Kulkarni, Reza Ardehali, C.-C. Jay Kuo, Xiaolei Xu, Chih-Ming Ho, and Tzung K. Hsiai.

Cardiac Light-Sheet Fluorescent Microscopy for Multi-Scale and Rapid Imaging of Architecture and Function. *Scientific Reports*, 6(1):22489, apr 2016.

[113] René R. Sevag Packard, Kyung In Baek, Tyler Beebe, Nelson Jen, Yichen Ding, Feng Shi, Peng Fei, Bong Jin Kang, Po-Heng Chen, Jonathan Gau, Michael Chen, Jonathan Y. Tang, Yu-Huan Shih, Yonghe Ding, Debiao Li, Xiaolei Xu, and Tzung K. Hsiai. Automated Segmentation of Light-Sheet Fluorescent Imaging to Characterize Experimental Doxorubicin-Induced Cardiac Injury and Repair. *Scientific Reports*, 7(1):8603, dec 2017.

[114] Xiao Ma, Yonghe Ding, Yong Wang, and Xiaolei Xu. A doxorubicin-induced cardiomyopathy model in adult zebrafish. *Journal of Visualized Experiments*, 2018(136), 2018.

[115] Yuehua Fang, Yanyi Sun, Chen Luo, Jianing Gu, Zhongwei Shi, Guoping Lu, Jean Sébastien Silvestre, and Zhenyue Chen. Evaluation of cardiac dysfunction in adult zebrafish using high frequency echocardiography. *Life Sciences*, 253, 2020.

[116] Amélie Pinard, Gregory T. Jones, and Dianna M. Milewicz. Genetics of Thoracic and Abdominal Aortic Diseases: Aneurysms, Dissections, and Ruptures, 2019.

[117] Julie De Backer, Laura Muiño Mosquera, and John A. Elefteriades. Genetics of aortic disease. In *Biomechanics of the Aorta*, pages 17–47. 2024.

[118] Laurence Faivre, Alice Masurel-Paulet, Gwenaelle Collod-Beroud, Bert L. Callewaert, Anne H. Child, Chantal Stheneur, Christine Binquet, Elodie Gautier, Bertrand Chevallier, Frédéric Huet, Bart L. Loeys, Eloisa Arbustini, Karin Mayer, Mine Arslan-Kirchner, Anatoli Kiotsekoglou, Paolo Comeglio, Maurizia Grasso, Dorothy J. Halliday, Christophe Beroud, Claire Bonithon-Kopp, Mireille Claustres, Peter N. Robinson, Lesley Adés, Julie De Backer, Paul Coucke, Uta Francke, Anne De Paepe, Catherine Boileau, and Guillaume Jondeau. Clinical and molecular study of 320 children with marfan syndrome and related type i fibrillinopathies in a series of 1009 probands with pathogenic FBN1 mutations. *Pediatrics*, 123(1), 2009.

[119] Bart L. Loeys, Ulrike Schwarze, Tammy Holm, Bert L. Callewaert, George H. Thomas, Hariyadarshi Pannu, Julie F. De Backer, Gretchen L. Oswald, Sofie Symoens, Sylvie Manouvrier, Amy E. Roberts, Francesca Faravelli, M. Alba Greco, Reed E. Pyeritz, Dianna M. Milewicz, Paul J. Coucke, Duke E. Cameron, Alan C. Braverman, Peter H. Byers, Anne M. De Paepe, and Harry C. Dietz. Aneurysm Syndromes Caused by Mutations in the TGF-β Receptor. *New England Journal of Medicine*, 355(8):788–798, 2006.

[120] Melanie G. Pepin, Ulrike Schwarze, Kenneth M. Rice, Mingdong Liu, Dru Leistritz, and Peter H. Byers. Survival is affected by mutation type and molecular mechanism in vascular Ehlers-Danlos syndrome (EDS type IV). *Genetics in Medicine*, 16(12), 2014.

[121] Yskert Von Kodolitsch, Julie De Backer, Helke Schüler, Peter Bannas, Cyrus Behzadi, Alexander M. Bernhardt, Mathias Hillebrand, Bettina Fuisting, Sara Sheikhzadeh, Meike Rybczynski, Tilo Kölbel, Klaus Püschel, Stefan Blankenberg, and Peter N. Robinson. Perspectives on the revised ghent criteria for the diagnosis of marfan syndrome. *Application of Clinical Genetics*, 8, 2015.

[122] John C.S. Dean. Marfan syndrome: Clinical diagnosis and management. *European Journal of Human Genetics*, 15(7), 2007.

[123] Julie De Backer. The expanding cardiovascular phenotype of Marfan syndrome, 2009.

[124] Julie De Backer, Laurence Campens, and Laura Muiño Mosquera. Looking for the Missing Links: Challenges in the Search for Genotype-Phenotype Correlation in Marfan Syndrome, 2018.

[125] Dong Chuan Guo, Christina L. Papke, Van Tran-Fadulu, Ellen S. Regalado, Nili Avidan, Ralph Jay Johnson, Dong H. Kim, Hariyadarshi Pannu, Marcia C. Willing, Elizabeth Sparks, Reed E. Pyeritz, Michael N. Singh, Ronald L. Dalman, James C. Grotta, Ali J. Marian, Eric A. Boerwinkle, Lorraine Q. Frazier, Scott A. LeMaire, Joseph S. Coselli, Anthony L. Estrera, Hazim J. Safi, Sudha Veeraraghavan, Donna M. Muzny, David A. Wheeler, James T. Willerson,

Robert K. Yu, Sanjay S. Shete, Steven E. Scherer, C. S. Raman, L. Maximilian Buja, and Dianna M. Milewicz. Mutations in Smooth Muscle Alpha-Actin (ACTA2) Cause Coronary Artery Disease, Stroke, and Moyamoya Disease, Along with Thoracic Aortic Disease. *American Journal of Human Genetics*, 84(5):617–627, 2009.

[126] Marjolijn Renard, Bert Callewaert, MacHteld Baetens, Laurence Campens, Kay MacDermot, Jean Pierre Fryns, Maryse Bonduelle, Harry C. Dietz, Isabel Mendes Gaspar, Diogo Cavaco, Eva Lena Stattin, Constance Schrander-Stumpel, Paul Coucke, Bart Loeys, Anne De Paepe, and Julie De Backer. Novel MYH11 and ACTA2 mutations reveal a role for enhanced TGFβ signaling in FTAAD. *International Journal of Cardiology*, 165(2), 2013.

[127] Dong Chuan Guo, Limin Gong, Ellen S. Regalado, Regie L. Santos-Cortez, Ren Zhao, Bo Cai, Sudha Veeraraghavan, Siddharth K. Prakash, Ralph J. Johnson, Ann Muilenburg, Marcia Willing, Guillaume Jondeau, Catherine Boileau, Hariyadarshi Pannu, Rocio Moran, Julie Debacker, Michael J. Bamshad, Jay Shendure, Deborah A. Nickerson, Suzanne M. Leal, C. S. Raman, Eric C. Swindell, and Dianna M. Milewicz. MAT2A mutations predispose individuals to thoracic aortic aneurysms. *American Journal of Human Genetics*, 96(1):170–177, 2015.

[128] Dong chuan Guo, Ellen M. Hostetler, Yuxin Fan, Richard J. Kulmacz, Di Zhang, Deborah A. Nickerson, Suzanne M. Leal, Scott A. LeMaire, Ellen S. Regalado, and Dianna M. Milewicz. Heritable Thoracic Aortic Disease Genes in Sporadic Aortic Dissection, 2017.

[129] Meghana R. Kunkala, Hartzell V. Schaff, Zhuo Li, Irina Volguina, Harry C. Dietz, Scott A. Lemaire, Joseph S. Coselli, and Heidi Connolly. Mitral valve disease in patients with marfan syndrome undergoing aortic root replacement. *Circulation*, 128(SUPPL.1), 2013.

[130] Julie F. De Backer, Daniel Devos, Patrick Segers, Dirk Matthys, Katrien François, Thierry C. Gillebert, Anne M. De Paepe, and Johan De Sutter. Primary impairment of left ventricular function in Marfan syndrome. *International Journal of Cardiology*, 112(3), 2006.

[131] Mary B. Sheppard, Jeffrey D. Smith, Lisa L. Bergmann, and Jakub K. Famulski. Novel SMAD3 variant identified in a patient with familial aortopathy modeled using a zebrafish embryo assay. *Frontiers in Cardiovascular Medicine*, 10, 2023.

[132] Andrew Prendergast, Bulat A. Ziganshin, Dimitra Papanikolaou, Mohammad A. Zafar, Stefania Nicoli, Sandip Mukherjee, and John A. Elefteriades. Phenotyping zebrafish mutant models to assess candidate genes associated with aortic aneurysm. *Genes*, 13(1):1–14, 2022.

[133] Andrew Prendergast, Mary B. Sheppard, Jakub K. Famulski, Stefania Nicoli, Sandip Mukherjee, Patrick Sips, and John A. Elefteriades. Modeling thoracic aortic genetic variants in the zebrafish: useful for predicting clinical pathogenicity? *Frontiers in Cardiovascular Medicine*, 12(February), 2025.

[134] Giulia L.M. Boezio, Anabela Bensimon-Brito, Janett Piesker, Stefan Guenther, Christian S.M. Helker, and Didier Y.R. Stainier. Endothelial TGF-β signaling instructs smooth muscle cell development in the cardiac outflow tract. *eLife*, 9, sep 2020.

[135] Maryline Abrial, Sandeep Basu, Mengmeng Huang, Vincent Butty, Asya Schwertner, Spencer Jeffrey, Daniel Jordan, Caroline E. Burns, and C Geoffrey Burns. Latent TGFβ-binding proteins 1 and 3 protect the larval zebrafish outflow tract from aneurysmal dilatation. *Disease Models & Mechanisms*, 15(3), mar 2022.

[136] Victor S. Costache, Jorn P. Meekel, Andreea Costache, Tatiana Melnic, Crina Solomon, Anca M. Chitic, Cristian Bucurenciu, Horatiu Moldovan, Iulian Antoniac, Gabriela Candea, and Kak K. Yeung. Geometric analysis of type b aortic dissections shows aortic remodeling after intervention using multilayer stents. *Materials*, 13(10), 2020.

[137] Paritosh Vasava, Payman Jalali, Mahsa Dabagh, and Pertti J. Kolari. Finite element modelling of pulsatile blood flow in idealized model of human aortic arch: Study of hypotension and hypertension. *Computational and Mathematical Methods in Medicine*, 2012, 2012.

[138] David Marlevi, Bram Ruijsink, Maximilian Balmus, Desmond Dillon-Murphy, Daniel Fovargue, Kuberan Pushparajah, Cristóbal Bertoglio, Massimiliano Colarieti-Tosti, Matilda

Larsson, Pablo Lamata, C. Alberto Figueroa, Reza Razavi, and David A. Nordsletten. Estimation of Cardiovascular Relative Pressure Using Virtual Work-Energy. *Scientific Reports*, 9(1), 2019.

[139] Elisa Fevola, Francesco Ballarin, Laura Jiménez-Juan, Stephen Fremes, Stefano Grivet-Talocia, Gianluigi Rozza, and Piero Triverio. An optimal control approach to determine resistance-type boundary conditions from in-vivo data for cardiovascular simulations. *International Journal for Numerical Methods in Biomedical Engineering*, 37(10), 2021.

[140] Chen Peng, Wei He, Xingsheng Huang, Jun Ma, Tong Yuan, Yun Shi, and Shengzhang Wang. The study on the impact of AAA wall motion on the hemodynamics based on 4D CT image data. *Frontiers in Bioengineering and Biotechnology*, 11, 2023.

[141] Bram Trachet. *De rol van verstoorde hemodynamica in aneurysmavorming bij muizen The Role of Disturbed Hemodynamics in Aneurysm Formation in Mice*. 2012.

[142] Michele Jessica L. Moore, Jessica L. Aros, Kimberly G. Steudel, and Keith C. Cheng. Fixation and Decalcification of Adult Zebrafish for Histological, Immunocytochemical, and Genotypic Analysis. *Biotechniques*, 32(2):296–298, 2000.

[143] Jean E. Copper, Lynn R. Budgeon, Christina A. Foutz, Damian B. van Rossum, Daniel J. Vanselow, Margaret J. Hubley, Darin P. Clark, David T. Mandrell, and Keith C. Cheng. Comparative analysis of fixation and embedding techniques for optimized histological preparation of zebrafish. *Comparative Biochemistry and Physiology Part - C: Toxicology and Pharmacology*, 208(July 2017):38–46, 2018.

[144] Aswin L. Menke, Jan M. Spitsbergen, Andre P.M. Wolterbeek, and Ruud A. Woutersen. Normal anatomy and histology of the adult zebrafish. *Toxicologic Pathology*, 39(5):759–775, 2011.

[145] Marie Hoareau, Naïma El Kholti, Romain Debret, and Elise Lambert. Characterization of the Zebrafish Elastin a (elnasa12235) Mutant: A New Model of Elastinopathy Leading to Heart Valve Defects. *Cells*, 12(10), 2023.

[146] Bram Trachet, Rodrigo Fraga-Silva, Alessandra Piersigilli, Patrick Segers, and Nikolaos Stergiopulos. Dissecting abdominal aortic aneurysm in Angiotensin II-infused mice: the importance of imaging. *Current Pharmaceutical Design*, 2015.

[147] Christian Dullin and Louisa Habich. In Vivo and Ex Vivo CT Imaging of Zebrafish Gonads. In *Methods in Molecular Biology*, volume 2218. 2021.

[148] Bert Vandeghinste, Bram Trachet, Marjolijn Renard, Christophe Casteleyn, Steven Staelens, Bart Loeys, Patrick Segers, and Stefaan Vandenberghe. Replacing vascular corrosion casting by in vivo micro-ct imaging for building 3D cardiovascular models in mice. *Molecular Imaging and Biology*, 2011.

[149] Fatemeh Babaei, Tony Liu Chi Hong, Kelvin Yeung, Shuk Han Cheng, and Yun Wah Lam. Contrast-Enhanced X-Ray Micro-Computed Tomography as a Versatile Method for Anatomical Studies of Adult Zebrafish. *Zebrafish*, 13(4), 2016.

[150] Anabela Bensimon-Brito, Giulia L M Boezio, João Cardeira-da Silva, Astrid Wietelmann, Srinath Ramkumar, Pia R Lundegaard, Christian S M Helker, Radhan Ramadass, Janett Piesker, Arno Nauerth, Clemens Mueller, and Didier Y R Stainier. Integration of multiple imaging platforms to uncover cardiovascular defects in adult zebrafish. *Cardiovascular Research*, oct 2021.

[151] Venera Weinhardt, Roman Shkarin, Tobias Wernet, Joachim Wittbrodt, Tilo Baumbach, and Felix Loosli. Quantitative morphometric analysis of adult teleost fish by X-ray computed tomography. *Scientific Reports*, 8(1):1–12, 2018.

[152] Eunseok Seo, Jae Hong Lim, Seung Jun Seo, and Sang Joon Lee. Whole-body imaging of a hypercholesterolemic female zebrafish by using synchrotron X-ray micro-CT. *Zebrafish*, 12(1):11–20, 2015.

[153] Yifu Ding, Daniel J. Vanselow, Maksim A. Yakovlev, Spencer R. Katz, Alex Y. Lin, Darin P. Clark, Phillip Vargas, Xuying Xin, Jean E. Copper, Victor A. Canfield, Khai C. Ang, Yuxin Wang, Xianghui Xiao, Francesco De Carlo, Damian B.Van Rossum, Patrick La Riviere, and Keith C. Cheng. Computational 3d histological phenotyping of whole zebrafish by x-ray histotomography. *eLife*, 8:1–28, 2019.

[154] Yi-Lwun Ho, Yio-Wha Shau, Huai-Jen Tsai, Lung-Chun Lin, Por-Jau Huang, and Fon-Jou Hsieh. Assessment of zebrafish cardiac performance using Doppler echocardiography and power angiography. *Ultrasound in Medicine & Biology*, 28(9):1137–1143, sep 2002.

[155] Lei Sun, Ching Ling Lien, Xiaochen Xu, and K. Kirk Shung. In Vivo Cardiac Imaging of Adult Zebrafish Using High Frequency Ultrasound (45-75 MHz). *Ultrasound in Medicine and Biology*, 34(1):31–39, 2008.

[156] Ting Yu Liu, Po Yang Lee, and Chih Chung Huang. In vivo analysis of adult zebrafish cardiac functions by Doppler-gated ultrahigh frame rate 80 MHz high frequency retrospective ultrasound imaging. *IEEE International Ultrasonics Symposium, IUS*, pages 2631–2634, 2012.

[157] Xiaowei Zhou, Lei Sun, Yanyan Yu, Weibao Qiu, Ching Ling Lien, K. Shung, and Weichuan Yu. Ultrasound bio-microscopic image segmentation for evaluation of zebrafish cardiac function. *IEEE Transactions on Ultrasonics, Ferroelectrics, and Frequency Control*, 60(4):718–726, 2013.

[158] Fatiha M. Benslimane, Maha Alser, Zain Z. Zakaria, Anju Sharma, Hana A. Abdelrahman, and Huseyin C. Yalcin. Adaptation of a Mice Doppler Echocardiography Platform to Measure Cardiac Flow Velocities for Embryonic Chicken and Adult Zebrafish. *Frontiers in Bioengineering and Biotechnology*, 7(May):1–17, 2019.

[159] Chao Chuan Chang, Pei Yu Chen, Hsin Huang, and Chih Chung Huang. In Vivo Visualization of Vasculature in Adult Zebrafish by Using High-Frequency Ultrafast Ultrasound Imaging. *IEEE Transactions on Biomedical Engineering*, 66(6):1742–1751, 2019.

[160] Chen Ho-Chiang, Hsin Huang, and Chih Chung Huang. High-frequency ultrasound deformation imaging for adult zebrafish during heart regeneration. *Quantitative Imaging in Medicine and Surgery*, 10(1):66–75, 2020.

[161] Juan Manuel González-Rosa, Gabriela Guzmán-Martínez, Inês João Marques, Héctor Sánchez-Iranzo, Luis Jesús Jiménez-Borreguero, and Nadia Mercader. Use of echocardiography

reveals reestablishment of ventricular pumping efficiency and partial ventricular wall motion recovery upon ventricular cryoinjury in the Zebrafish. *PLoS ONE*, 9(12):1–18, 2014.

[162] Selina J. Hein, Lorenz H. Lehmann, Mandy Kossack, Lonny Juergensen, Dieter Fuchs, Hugo A. Katus, and David Hassel. Advanced echocardiography in adult zebrafish reveals delayed recovery of heart function after myocardial cryoinjury. *PLoS ONE*, 10(4):1–21, 2015.

[163] Louis W. Wang, Inken G. Huttner, Celine F. Santiago, Scott H. Kesteven, Ze-Yan Yu, Michael P. Feneley, and Diane Fatkin. Standardized echocardiographic assessment of cardiac function in normal adult zebrafish and heart disease models. *Disease Models & Mechanisms*, 10(1):63–76, 2017.

[164] Alessandro Evangelisti, Katharina Schimmel, Shaurya Joshi, Kavya Shah, Sudeshna Fisch, Kevin M. Alexander, Ronglih Liao, and Isabel Morgado. High-Frequency Ultrasound Echocardiography to Assess Zebrafish Cardiac Function. *Journal of Visualized Experiments*, 2020(157), mar 2020.

[165] Mao Hsiang Huang, Amir Mohammad Naderi, Ping Zhu, Xiaolei Xu, and Hung Cao. Assessing Cardiac Functions of Zebrafish from Echocardiography Using Deep Learning. *Information (Switzerland)*, 14(6), 2023.

[166] Eleonora Sulas, Monica Urru, Roberto Tumbarello, Luigi Raffo, and Danilo Pani. Automatic detection of complete and measurable cardiac cycles in antenatal pulsed-wave Doppler signals. *Computer Methods and Programs in Biomedicine*, 190, 2020.

[167] Eleonora Sulas, Emanuele Ortu, Monica Urru, Roberto Tumbarello, Luigi Raffo, Giuliana Solinas, and Danilo Pani. Impact of pulsed-wave-Doppler velocity-envelope tracing techniques on classification of complete fetal cardiac cycles. *PLoS ONE*, 16(4 April):1–25, 2021.

[168] Samira Kabli, A. Alia, Herman P. Spaink, Fons J. Verbeek, and Huub J.M. De Groot. Magnetic resonance microscopy of the adult zebrafish. *Zebrafish*, 3(4), 2006.

[169] Gavin D. Merrifield, James Mullin, Lindsay Gallagher, Carl Tucker, Maurits A. Jansen, Martin Denvir, and William M.

Holmes. Rapid and recoverable in vivo magnetic resonance imaging of the adult zebrafish at 7T. *Magnetic Resonance Imaging*, 37:9–15, apr 2017.

[170] Samira Kabli, Herman P. Spaink, Huub J.M. De Groot, and A. Alia. In vivo metabolite profile of adult zebrafish brain obtained by high-resolution localized magnetic resonance spectroscopy. *Journal of Magnetic Resonance Imaging*, 29(2), 2009.

[171] Samira Kabli, Shuning He, Herman P. Spaink, Adam Hurlstone, Ewa Snaar Jagalska, Huub J.M. De Groot, and A. Alia. In vivo magnetic resonance imaging to detect malignant melanoma in adult zebrafish. *Zebrafish*, 7(2), 2010.

[172] Noémie Hamilton, Claire Allen, and Steven Reynolds. Longitudinal MRI brain studies in live adult zebrafish. *NMR in Biomedicine*, 36(7), 2023.

[173] Sonal Sharma, Sergey Magnitsky, Emily Reesey, Mitchell Schwartz, Suraiya Haroon, Manuela Lavorato, Sherine Chan, Rui Xiao, Benjamin J. Wilkins, Daniel Martinez, Christoph Seiler, and Marni J. Falk. Novel Development of Magnetic Resonance Imaging to Quantify the Structural Anatomic Growth of Diverse Organs in Adult and Mutant Zebrafish. *Zebrafish*, 21(1), 2024.

[174] Jana Koth, Mahon L. Maguire, Darryl McClymont, Leonie Diffley, Victoria L. Thornton, John Beech, Roger K. Patient, Paul R. Riley, and Jürgen E. Schneider. High-Resolution Magnetic Resonance Imaging of the Regenerating Adult Zebrafish Heart. *Scientific Reports*, 7(1):2917, dec 2017.

[175] Keith C. Cheng, Xuying Xin, Darin P. Clark, and Patrick La Riviere. Whole-animal imaging, gene function, and the Zebrafish Phenome Project. *Current Opinion in Genetics & Development*, 21(5):620–629, oct 2011.

[176] M. Juliana Gomez-Garcia, Amber L. Doiron, Robyn R.M. Steele, Hagar I. Labouta, Bahareh Vafadar, Robert D. Shepherd, Ian D. Gates, David T. Cramb, Sarah J. Childs, and Kristina D. Rinker. Nanoparticle localization in blood vessels: dependence on fluid shear stress, flow disturbances, and flow-induced changes in endothelial physiology. *Nanoscale*, 10(32):15249–15261, 2018.

[177] Bong Jin Kang, Jinhyoung Park, Jieun Kim, Hyung Ham Kim, Changyang Lee, Jae Youn Hwang, Ching Ling Lien, and K. Kirk Shung. High-frequency dual mode pulsed wave Doppler imaging for monitoring the functional regeneration of adult zebrafish hearts. *Journal of the Royal Society Interface*, 12(103), 2015.

[178] Chih Chung Huang, Ta Han Su, and Cho Chiang Shih. High-resolution tissue doppler imaging of the zebrafish heart during its regeneration. *Zebrafish*, 12(1):48–57, 2015.

[179] Massoud Zolgharni, Niti M. Dhutia, Graham D. Cole, M. Reza Bahmanyar, Siana Jones, S. M.Afzal Sohaib, Sarah B. Tai, Keith Willson, Judith A. Finegold, and Darrel P. Francis. Automated aortic doppler flow tracing for reproducible research and clinical measurements. *IEEE Transactions on Medical Imaging*, 33(5):1071–1082, 2014.

[180] David N. Cooper, Michael Krawczak, Constantin Polychronakos, Chris Tyler-Smith, and Hildegard Kehrer-Sawatzki. Where genotype is not predictive of phenotype: Towards an understanding of the molecular basis of reduced penetrance in human inherited disease. *Human Genetics*, 132(10):1077–1130, 2013.

[181] A. J. Niimi. Relationship of body surface area to weight in fishes. *Canadian journal of zoology*, 53(8), 1975.

[182] Louis W. Wang, Inken G. Huttner, Celine F. Santiago, and Diane Fatkin. Bradycardia in Zebrafish heart failure: A true physiological response or anesthetic-induced red herring? *Zebrafish*, 13(6):475–476, 2016.

[183] Ling Lee, Christine E. Genge, Michelle Cua, Xiaoye Sheng, Kaveh Rayani, Mirza F. Beg, Marinko V. Sarunic, and Glen F. Tibbits. Functional assessment of cardiac responses of adult zebrafish (danio rerio) to acute and chronic temperature change using high-resolution echocardiography. *PLoS ONE*, 11(1):1–18, 2016.

[184] Christopher S. Hayward, Wally V. Kalnins, and Raymond P. Kelly. Gender-related differences in left ventricular chamber function. *Cardiovascular Research*, 49(2):340–350, 2001.

[185] Gerlinde Logghe, Bram Trachet, Lydia Aslanidou, Pablo Villaneuva-Perez, Julie De Backer, Nikolaos Stergiopulos, Marco Stampanoni, Hiroki Aoki, and Patrick Segers. Propagation-based phase-contrast synchrotron imaging of aortic dissection in mice: from individual elastic lamella to 3D analysis. *Scientific Reports*, 8(1):2223, dec 2018.

[186] Federica Marone, Alain Studer, Heiner Billich, Leonardo Sala, and Marco Stampanoni. Towards on-the-fly data post-processing for real-time tomographic imaging at TOMCAT. *Advanced Structural and Chemical Imaging*, 3(1), 2017.

[187] F. Marone and M. Stampanoni. Regridding reconstruction algorithm for real-time tomographic imaging. *Journal of Synchrotron Radiation*, 19(6), 2012.

[188] D. Paganin, S. C. Mayo, T. E. Gureyev, P. R. Miller, and S. W. Wilkins. Simultaneous phase and amplitude extraction from a single defocused image of a homogeneous object. *Journal of Microscopy*, 206(1):33–40, 2002.

[189] Bram Trachet, Goran Lovric, Pablo Villanueva-Perez, Lydia Aslanidou, Mauro Ferraro, Gerlinde Logghe, Nikolaos Stergiopulos, and Patrick Segers. Synchrotron-based phase contrast imaging of cardiovascular tissue in mice - Grating interferometry or phase propagation? *Biomedical Physics and Engineering Express*, 2019.

[190] B. C. Masschaele, V. Cnudde, M. Dierick, P. Jacobs, L. Van Hoorebeke, and J. Vlassenbroeck. UGCT: New X-ray radiography and tomography facility. *Nuclear Instruments and Methods in Physics Research, Section A: Accelerators, Spectrometers, Detectors and Associated Equipment*, 580(1 SPEC. ISS.):266–269, 2007.

[191] Deshun Lu and Ghassan S. Kassab. Role of shear stress and stretch in vascular mechanobiology. *Journal of The Royal Society Interface*, 8(63):1379–1385, oct 2011.

[192] Jennifer M. Dolan, John Kolega, and Hui Meng. High Wall Shear Stress and Spatial Gradients in Vascular Pathology: A Review. *Annals of Biomedical Engineering*, 41(7):1411–1427, jul 2013.

[193] Bram Trachet, Joris Bols, Joris Degroote, Benedict Verhegghe, Nikolaos Stergiopulos, Jan Vierendeels, and Patrick Segers. An Animal-Specific FSI Model of the Abdominal Aorta in Anesthetized Mice. *Annals of Biomedical Engineering*, 43(6):1298–1309, jun 2015.

[194] R. Aidan Jamison, Chaminda R. Samarage, Robert J. Bryson-Richardson, and Andreas Fouras. In Vivo Wall Shear Measurements within the Developing Zebrafish Heart. *PLoS ONE*, 8(10):e75722, oct 2013.

[195] Jeffrey J. Hsu, Vijay Vedula, Kyung In Baek, Cynthia Chen, Junjie Chen, Man In Chou, Jeffrey Lam, Shivani Subhedar, Jennifer Wang, Yichen Ding, Chih-Chiang Chang, Juhyun Lee, Linda L. Demer, Yin Tintut, Alison L. Marsden, and Tzung K. Hsiai. Contractile and hemodynamic forces coordinate Notch1b-mediated outflow tract valve formation. *JCI Insight*, 4(10), may 2019.

[196] Mehrdad Roustaei, Kyung In Baek, Zhaoqiang Wang, Susana Cavallero, Sandro Satta, Angela Lai, Ryan O'Donnell, Vijay Vedula, Yichen Ding, Alison Lesley Marsden, and Tzung K Hsiai. Computational simulations of the 4D micro-circulatory network in zebrafish tail amputation and regeneration. *Journal of The Royal Society Interface*, 19(187), feb 2022.

[197] Juhyun Lee, Tzu Chieh Chou, Dongyang Kang, Hanul Kang, Junjie Chen, Kyung In Baek, Wei Wang, Yichen DIng, DIno DI Carlo, Yu Chong Tai, and Tzung K. Hsiai. A Rapid Capillary-Pressure Driven Micro-Channel to Demonstrate Newtonian Fluid Behavior of Zebrafish Blood at High Shear Rates. *Scientific Reports*, 7(1):1–8, 2017.

[198] Robin Fåhræus and Torsten Lindqvist. The viscosity of the blood in narrow capillary tubes. *American Journal of Physiology-Legacy Content*, 96(3):562–568, mar 1931.

[199] A. R. Pries, D. Neuhaus, and P. Gaehtgens. Blood viscosity in tube flow: Dependence on diameter and hematocrit. *American Journal of Physiology - Heart and Circulatory Physiology*, 263(6 32-6), 1992.

[200] Keith E. Korsmeyer, N. Chin Lai, Robert E. Shadwick, and Jeffrey B. Graham. Heart rate and stroke volume contributions

to cardiac output in swimming yellowfin tuna: Response to exercise and temperature. *Journal of Experimental Biology*, 200(14):1975–1986, 1997.

[201] C. W. Ong, F. Kabinejadian, F. Xiong, Y. R. Wong, M. Toma, Y. N. Nguyen, K. J. Chua, F. S. Cui, P. Ho, and H. Leo. Pulsatile Flow Investigation in Development of Thoracic Aortic Aneurysm: An In-Vitro Validated Fluid Structure Interaction Analysis. *Journal of Applied Fluid Mechanics*, 12(6):1855–1872, nov 2019.

[202] Marvin H. Braun, Richard W. Brill, John M. Gosline, and David R. Jones. Form and function of the bulbus arteriosus in yellowfin tuna (Thunnus albacares), bigeye tuna (Thunnus obesus) and blue marlin (Makaira nigricans): dynamic properties. *Journal of Experimental Biology*, 206(19):3311–3326, 2003.

[203] Norman Hu, David Sedmera, H. Joseph Yost, and Edward B. Clark. Structure and function of the developing zebrafish heart. *The Anatomical Record*, 260(2):148–157, oct 2000.

[204] Nabid Salehin, Cameron Villarreal, Tanveer Teranikar, Benjamin Dubansky, Juhyun Lee, and Cheng Jen Chuong. Assessing Pressure-Volume Relationship in Developing Heart of Zebrafish In-Vivo. *Annals of Biomedical Engineering*, 49(9), 2021.

[205] Choon Hwai Yap, Xiaoqin Liu, and Kerem Pekkan. Characterizaton of the vessel geometry, flow mechanics and wall shear stress in the great arteries of wildtype prenatal mouse. *PLoS ONE*, 9(1), 2014.

[206] Shier Nee Saw, Chia Dawn, Arijit Biswas, Citra Nurfarah Zaini Mattar and Choon Hwai Yap. Characterization of the in vivo wall shear stress environment of human fetus umbilical arteries and veins. *Biomech Model Mechanobiol.*, 16(1), 2017.

[207] Yajuan Wang, Onur Dur, Michael J. Patrick, Joseph P. Tinney, Kimimasa Tobita, Bradley B. Keller, and Kerem Pekkan. Aortic Arch Morphogenesis and Flow Modeling in the Chick Embryo. *Annals of Biomedical Engineering*, 37(6):1069–1081, jun 2009.

[208] Bram Trachet, Joris Bols, Gianluca De Santis, Stefaan Vandenberghe, Bart Loeys, and Patrick Segers. The Impact of Simplified Boundary Conditions and Aortic Arch Inclusion on CFD Simulations in the Mouse Aorta: A Comparison With Mouse-specific Reference Data. *Journal of Biomechanical Engineering*, 133(12), dec 2011.

[209] Mona Alimohammadi, Joseph M. Sherwood, Morad Karimpour, Obiekezie Agu, Stavroula Balabani, and Vanessa Díaz-Zuccarini. Aortic dissection simulation models for clinical support: fluid-structure interaction vs. rigid wall models. *BioMedical Engineering OnLine*, 14(1):34, dec 2015.

[210] Sergio Ruiz de Galarreta, Aitor Cazón, Raúl Antón, and Ender A. Finol. The Relationship Between Surface Curvature and Abdominal Aortic Aneurysm Wall Stress. *Journal of Biomechanical Engineering*, 139(8), aug 2017.

[211] David De Wilde, Bram Trachet, Guido De Meyer, and Patrick Segers. The influence of anesthesia and fluid-structure interaction on simulated shear stress patterns in the carotid bifurcation of mice. *Journal of Biomechanics*, 2016.

[212] N. Stergiopulos, P. Segers, and N. Westerhof. Use of pulse pressure method for estimating total arterial compliance in vivo. *American Journal of Physiology - Heart and Circulatory Physiology*, 276(2 45-2), 1999.

[213] M. H. Braun. Form and function of the bulbus arteriosus in yellowfin tuna (Thunnus albacares), bigeye tuna (Thunnus obesus) and blue marlin (Makaira nigricans): static properties. *Journal of Experimental Biology*, 206(19):3311–3326, 2003.

[214] Gerhard A. Holzapfel, Thomas C. Gasser, and Ray W. Ogden. A new constitutive framework for arterial wall mechanics and a comparative study of material models. *Journal of Elasticity*, 2000.

[215] Bram Trachet, Abigail Swillens, Denis Van Loo, Christophe Casteleyn, Anne De Paepe, Bart Loeys, and Patrick Segers. The influence of aortic dimensions on calculated wall shear stress in the mouse aortic arch. *Computer Methods in Biomechanics and Biomedical Engineering*, 2009.

[216] Bram Trachet, Marjolijn Renard, Gianluca De Santis, Steven Staelens, Julie De Backer, Luca Antiga, Bart Loeys, and Patrick Segers. An integrated framework to quantitatively link mouse-specific hemodynamics to aneurysm formation in angiotensin ii-infused ApoE-/-mice. *Annals of Biomedical Engineering*, 2011.

[217] Bram Trachet, Alessandra Piersigilli, Rodrigo A. Fraga-Silva, Lydia Aslanidou, Jessica Sordet-Dessimoz, Alberto Astolfo, Marco F.M. Stampanoni, Patrick Segers, and Nikolaos Stergiopulos. Ascending Aortic Aneurysm in Angiotensin II-Infused Mice: Formation, Progression, and the Role of Focal Dissections. *Arteriosclerosis, Thrombosis, and Vascular Biology*, 36(4), 2016.

[218] Bram Trachet, Lydia Aslanidou, Alessandra Piersigilli, Rodrigo A. Fraga-Silva, Jessica Sordet-Dessimoz, Pablo Villanueva-Perez, Marco F.M. Stampanoni, Nikolaos Stergiopulos, and Patrick Segers. Angiotensin II infusion into ApoE-/-mice: A model for aortic dissection rather than abdominal aortic aneurysm? *Cardiovascular Research*, 2017.

[219] Lydia Aslanidou, Mauro Ferraro, Goran Lovric, Matthew R. Bersi, Jay D. Humphrey, Patrick Segers, Bram Trachet, and Nikos Stergiopulos. Co-localization of microstructural damage and excessive mechanical strain at aortic branches in angiotensin-II-infused mice. *Biomechanics and Modeling in Mechanobiology*, 19(1), 2020.

[220] Alexander D Kaiser, Jing Wang, Aaron L Brown, Enbo Zhu, Tzung Hsiai, and Alison L Marsden. A Fluid-Structure Interaction Model of the Zebrafish Aortic Valve. *arXiv preprint*, pages 1–11, 2024.